Impact of Vehicle Charge and Discharge Cycles on the Thermal Characteristics of Lithium-ion Batteries

by

Satyam Panchal

A thesis
presented to the University of Waterloo
in fulfillment of the
thesis requirement for the degree of

Master of Applied Science
in
Mechanical Engineering

Waterloo, Ontario, Canada, 2014

Author's Declaration

I hereby declare that I am the sole author of this thesis. This is a true copy of the thesis, including any required final revisions, as accepted by my examiners.

I understand that my thesis may be made electronically available to the public.

Satyam Panchal

Abstract

The performance, life-cycle cost, and safety of electric and hybrid electric vehicles (EVs and HEVs) depend strongly on the vehicle's energy storage system. Advanced batteries such as lithium-ion (Li-ion) polymer batteries are quite viable options for storing energy in EVs and HEVs. Battery temperature impacts battery performance, SOH, and may even present a safety risk. Therefore, thermal management is essential for achieving the desired performance and life-cycle from a vehicle battery pack comprised of a particular battery cell or module.

This work presents the thermal characteristics of a prismatic pouch battery comprised of $LiFePO_4$ electrode material and modules. Characterization is performed via experiments that enable development of an empirical battery thermal model for vehicle simulations. As well electrical data is presented for the validation of electrochemistry based battery thermal models. The research is organized into two parts.

Part-I: An apparatus was designed to measure the surface temperature distribution, heat flux, and heat generation from a battery pouch cell undergoing various charge/discharge cycles. In this work, a prismatic lithium-ion pouch cell is cooled by two cold plates with 19 thermocouples and 3 heat flux sensors applied to the battery at distributed locations. The total heat generation from a particular battery is obtained at various discharge rates (1C, 2C, 3C, and 4C) and different cooling bath temperature (5 ^{0}C, 15 ^{0}C, 25 ^{0}C, and 35 ^{0}C). Results show that the heat generation rate is greatly affected by the both discharge rate and boundary conditions. The developed experimental facility can be used for the measurement of heat generation from any prismatic battery, regardless of chemistry. Thermal images obtained at different discharge rates are presented within to enable visualization of the temperature distribution. An empirical battery thermal model is developed and validated with collected data from a test bench in terms of temperature, SOC and voltage profile.

In part-II: In-situ vehicle data was collected using three data loggers installed in three different Burlington Hydro Ford Escape vehicles (one pure EV and other two HEVs). The data collection infrastructure developed produced monthly reports for the EV, allowing Burlington Hydro to track the vehicle's distance travelled, energy consumption, efficiency, and charging times. Five months of data for the EV indicated 792.6 km travelled and 222.6 kWh of grid electricity

consumed. The real-world drive cycles from the EV were then performed with the lab apparatus and thermal data was collected and analyzed. In this study, a vehicle model using PSAT/Autonomie software is developed based on available specifications of the vehicle and is validated with the collected drive cycle.

Acknowledgements

Many people have contributed the development of this project and it is a pleasure to acknowledge my indebtedness to a few of them.

This work has benefitted immeasurably from the insights, guidance, constant support and encouragement of my mentor Prof. Roydon Fraser, whose altruistic nature in perceiving and dispensing scientific knowledge is greatly appreciated.

A special note of appreciation is owed to Scott Mathewson for helping me to build the test bench. I could not have completed this research work without his support. He is one of the nicest people I have ever seen in my life.

I would like to thank Prof Richard Culham for allowing me to use his Microelectronic Heat Transfer Lab (MHTL) and some of the components for my research work. A special thanks to Prof Michael Fowler for allowing me to work in his lab.

I would like to thank people at Burlington Hydro Co., Cross Chasm Co, and also my officemate, Ehsan, for providing assistance and constructive consultations.

Lastly, and most importantly I would like to thank my family: my mom (Sushilaben) and my dad (Jashubhai), my wife (Jolly), my twins (Dev and Dwij) and my sisters (Kirti and Swati).

Table of Contents

List of Figures

List of Tables

Nomenclature

A	=	area [m^2]
c_p	=	specific heat capacity [J/kg°C]
E	=	open-circuit potential [V]
h	=	heat transfer coefficient [W/m^2°C]
I	=	current [A]
m	=	mass [kg]
$\dot{m}$	=	mass flow rate [kg/s]
N	=	number
Pr	=	Prandtl number
Q	=	heat [KJ]
$\dot{Q}$		heat generation rate [W]
q	=	heat flux [W/m^2]
Ra	=	Rayleigh number
T	=	temperature [°C or K]
t	=	time [s]
V	=	cell voltage or cell potential [V]
dE/dT	=	temperature coefficient [V/°C]
dT/dx	=	temperature gradient [°C /m]

Greek Symbols

α	=	thermal diffusivity [m^2/s]
β	=	thermal expansion coefficient
ε	=	emissivity
i	=	layer index
ρ	=	density [kg/m^3]
μ	=	dynamic viscosity [kg/ms]
ν	=	kinematic viscosity [m^2/s]

Subscripts

∞	=	ambient
b	=	battery
bs	=	battery surface
c	=	cell
$conv$	=	convection
e	=	electrical
f	=	fluid
gen	=	generated
i	=	layer index
n	=	negative electrode
oc	=	open circuit
p	=	positive electrode

rad	=	radiation
T	=	temperature
th	=	thermal
w	=	water
x,y,z	=	Cartesian coordinate directions

Acronyms and Abbreviations

A123	A lithium-ion pouch cell manufactured by A123. It is obtained after market.
A	Ampere
Ah	Ampere-hour
APS	Accelerator pedal position
ARC	Accelerated rate calorimeter
BC	Boundary condition
BPS	Brake pedal position
BEV	Battery electric vehicle
BOL	Beginning of life
C	Capacity
CD	Charge depleting
CAD	Computer aided design
CIL	Component in loop
CNTs	Carbon nanotubes
^{0}C	Degree Celsius
DOD	Depth of discharge
DEC	Diethyl carbonate
DMC	Dimethyl carbonate
DRU	Data Recording Unit
Dischg	Discharge
EC	Ethylene carbonate
EMC	Ethyl-methyl carbonate
EV	Electric vehicle
EOL	End of life
EOD	End of discharge
E-stop	Emergency shut down
FEA	Finite element analysis
GM	General motors
GPS	Global positioning satellite
GHG	Greenhouse gas
HEV	Hybrid electric vehicle
HFA	Heat flux array
HFS	Heat flux sensor
ICE	Internal combustion engine
IHC	Isothermal heat conduction calorimeter
IR	Infra-red
kW	Kilowatt
Km	Kilometer
kW/L	Kilo watt per liter
Kg	Kilo gram
L	Liter
Li-ion	Lithium ion
$LiCoO_2$ / LCO	Lithium-cobalt-dioxide

$LiFePO_4$ / LFP	Lithium-phosphate
LiBOB	Lithium bis (oxalate) borate
mA	Milli-ampere
MHTL	Microelectronics Heat Transfer Lab
NiMH	Nickel metal hydride
NiCad	Nickel cadmium
OCV/Voc	Open circuit voltage
PHEV	Plug-in hybrid electric vehicle
PVC	Polyvinyl chloride
PSAT	Power train system analysis toolkit
PE	polyethylene
PP	polypropylene
REV	Rapid electric vehicle
REEV	Range extended electric vehicle
RESS	Rechargeable electricity storage system
Sec	Seconds
SOC	State of charge
SOD	Start of discharge
SOH	State of health
SEI	Solid electrolyte interface
SPI	Solid permeable interface
SLE	Special limit of errors
TC	Thermocouple
TOU	Time-of-use
US	United states
UW	University of waterloo
UPS	Uninterrupted power source
UDDS	Urban dynamometer driving schedule
V	Volt
V2G	Vehicle-to-grid
W	Watt
Wh	Watt hour
$	Dollar

Chapter 1

Introduction

According to Natural Resources Canada, in 2007, there were around 20 million vehicles on Canadian roads, up nearly 2.5 million since 2000. Out of these, 19 million (96.4%) vehicles were light duty, 2% were medium trucks, and 1.7% were heavy trucks. These vehicles travelled some 332 billion kilometers consuming 31 billion litres of gasoline and 11 billion litres of diesel [1]. One of the largest sources of greenhouse gases (GHG) in Canada is road transportation, which contributes significantly to urban air quality problems [2]. Canadian GHG emissions can be lowered by replacing gasoline usage with the adoption of alternative fuels, and urban air quality can also be increased.

Therefore, demand for hybrid and electric vehicles has increased significantly due to rising costs and environmental concerns [3]. The burning of fossil fuels for gasoline has decreased the number of trees in the world and has also affected the overall air quality for all living and non-living creatures on this planet. In addition, the price of oil and gasoline has been steadily rising over the decades, making hybrid and electric vehicles a cheaper and more efficient option [3]. Due to environmental benefits and rising oil prices, major automobile manufacturers have spent millions of dollars on the research and development of hybrid and electric vehicles which are becoming more and more environmentally friendly by protecting the eco-system.

Batteries, a major powertrain component of hybrid and electric vehicles, will undergo thousands of cycles during the life-time of a vehicle. Over this lifetime, a battery degrades potentially to the point of requiring replacement. Given the high cost of the battery and its importance in determining electric vehicle range, it is very desirable to postpone battery degradation as long as possible. One element of controlling battery degradation is controlling battery temperature [4, 5]. Understanding vehicle battery temperatures during discharge is the focus of this research.

In order to better understand the battery thermal problem, it is useful to first understand the basic vehicle applications for large battery packs. Electrified vehicles are classified in three groups: 1)

Hybrid electric vehicles (HEVs), 2) Plug-in hybrid electric vehicles (PHEVs), and 3) Electric vehicles (EVs).

1.1 Hybrid Electric Vehicles (HEVs)

A hybrid electric vehicle has one or more power sources, such as an internal combustion engine and an electric motor [3]. In Hybrid Vehicles, the engine is smaller and hence it provides better fuel economy. These vehicles use less fuel and produce less pollution. Modern mass produced hybrids prolong the charge on their batteries by capturing kinetic energy through regenerative braking. During cruising or idling where only a light thrust is required, "full" hybrids can use the internal combustion engine to generate electricity by spinning an electric generator to recharge the battery or to feed power to an electric motor which drives the vehicle. Almost all hybrids still require gasoline and diesel as their sole fuel source as well as other fuels such as ethanol or occasionally plant based oils. There are three main types of Hybrid configurations available in market: 1) Parallel Hybrid Vehicle Configuration 2) Series Hybrid Vehicle Configuration, and 3) Series-parallel Hybrid Vehicle Configuration.

1.2 Plug-In-Hybrid Electric Vehicle (PHEVs)

Plug-in–hybrid electric vehicles, which can consist of any of the three hybrid systems, have a large capacity battery pack that is charged from an electrical outlet. They can drive a certain distance in an all-electric mode and, after that, the vehicles operate like a non-plug-in hybrid. This means that, while driving in all electric modes, the PHEV consumes no fuel and there is zero emission. PHEVs are classified by their Charge-Depleting (CD) range. For example, a PHEV-10 has charge-depleting range of 10 mile (16 km) and a PHEV-40 has a charge-depleting range of 40 mile (64km). If one drives less than 64 km a day, the PHEV-40 will normally operate in charge-depleting mode.

Most of PHEVs on the road today are passenger cars, but there are also PHEV versions of buses, trains, utility trucks, vans, scooters, motor cycles and military vehicles. The cost of electricity to power plug-in-hybrids for all electric operation is less than one quarter of the cost of a gasoline vehicle [6]. PHEVs not only reduce greenhouse gas (GHG) emissions that contribute to global warming but also decrease air pollution. In PHEVs, if batteries are charged from renewable

electricity, plug-in hybrids use no fossil fuel during their all electric range and produce lower greenhouse gas (GHG) emissions. PHEVs also provide other benefits like improvement in national energy security, fewer fill-ups at the filling station, home recharging, emergency backup power in the home and vehicle-to-grid (V2G) applications [7, 8].

1.3 Electric Vehicles (EVs)

Electric vehicles (EVs) do not use an internal combustion engine (ICE) to supply power to the wheels and drivetrain but they rely on an electric motor to supply the power to the wheels. Most electric vehicles (EVs) have a more elaborate method to control the amount of electricity going to the motor and a system of gears to drive the wheels in a most efficient manner [9]. The high price of oil and increased concern over the environmental impact of the petroleum-based transportation have led to renewed interest in an electric transportation [10]. Electric vehicles today are electric cars, motorbikes, trains, airplanes and boats.

Electric vehicles (EVs) differ from fossil fuel powered vehicle in that the electricity they consume is generated from different sources, like solar power, tidal power and wind power or any combination of those energies [9, 10]. The electricity can be stored on board the vehicle using a battery, flywheel or a capacitor [9]. The main advantage of electric or hybrid electric vehicles is regenerative braking and the ability to recover energy lost during braking as electricity stored in the on-board battery [11, 12]. Gasoline and Diesel Engines are only 30% to 40% efficient at converting fuel energy into kinetic energy (i.e. as motion or as work on driveshaft), while electric motors can convert more than 94% of electrical energy supplied into useful work. Electric vehicles can be a much more energy efficient means of transportation, provided that the electricity can be effectively stored and supplied to the motor.

Moving from conventional vehicles to EVs and HEVs, the design challenge moves from the engine to the battery. Lithium-ion batteries are a good choice for EVs and HEVs because of higher power and higher energy density [13]. Nickel-metal hydride batteries are still attractive because of their low cost. Due to the dependency of EVs on batteries, it is important to know and manage the battery status, in order to achieve a better level of safety and reliability. Batteries are discussed in greater detail in Chapter 2.

1.4 Problem Definition

The performance and life of Li-ion battery packs for PHEVs, HEVs, and EVs applications are greatly influenced by battery operating temperatures [4, 5]. To understand the thermal behaviour of batteries and its impact on battery performance and life, the first step experimentally is to study the battery temperature distributions and the heat generation profiles at different charge and discharge rates. And to make this study relevant to PHEVs, HEVs, and EVs, the charge and discharge rates must be typical of those seen and expected to be seen in vehicles. Figure 1 shows the surface temperature of a lithium-ion pouch cell (for definition of pouch cell, module, and pack, refer to section-2.8) at different discharge rates of 1C, 2C, 3C and 4C (C-rate is the measurement of the charge and discharge current of a battery), on the order of those seen in vehicles. The charge rate between discharges in all cases is 1C.

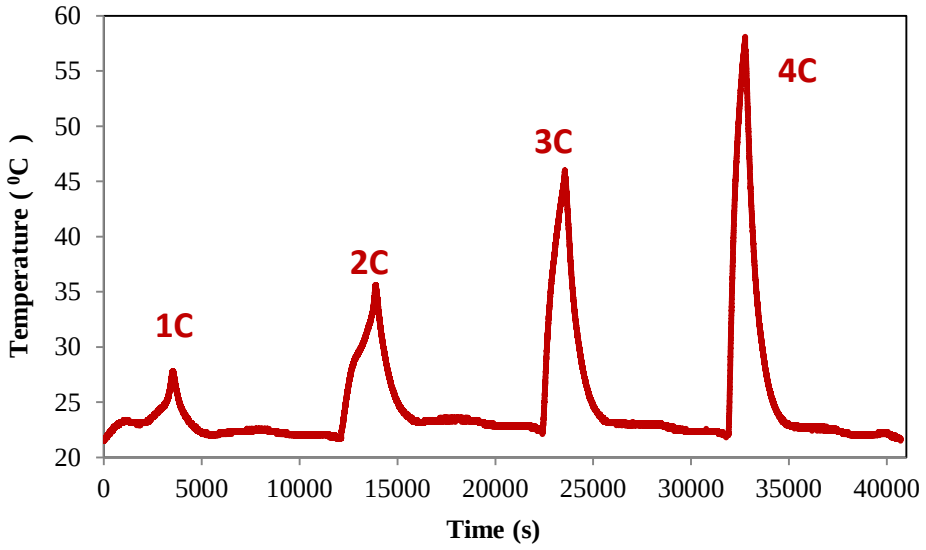

Figure 1 : Surface temperature profile of a lithium-ion pouch cell during 1C charge and 1C, 2C, 3C and 4C discharge rates [14]

Figure 1 illustrates the thermal spikes that can accompany discharge. Over a short 20 minute time period (short from a vehicle operation viewpoint) for 3C and a 15 minute time period for 4C discharge, enough heat is generated to increase the cell temperature to 46 ^{0}C (for 3C) and 58 ^{0}C (for 4C) from a 22 ^{0} C start condition. This value is only for a single pouch cell with free convection boundary condition, so even a greater temperature can result when extrapolated to the approximately 300 pouch cells in a battery pack of PHEVs, HEVs, and EVs, where there is no

free boundary convection, but only conduction between pouch cells,; this problem is explained next.

Operating lithium-ion batteries above 50 ^{0}C can accelerate the aging process and lead to significant degradation of battery capacity and electric range reduction [15]. Following from Figure 1, battery cell temperatures above 50 ^{0}C are very possible especially when cells are stacked into modules, and then packs, and if the ambient temperature is closer to 50 ^{0}C than the 22 ^{0}C used in Figure 1. The possibility of fire is also a major issue with high operating temperature where thermal runaway is a possibility [16]. Thus, adequate battery cooling and thermal management are an integral part of the vehicle operation during electric mode operation. PHEVs, HEVs, and EVs require a robust battery thermal management system in order to ensure optimal (safe, good performance, and long battery life) vehicle operation.

Experimental data on the thermal characteristics of batteries is important not only to the battery pack designers and modellers, but also to those looking more fundamentally at electrochemical battery models [17]. Battery modelling gives very important information on battery charging/discharging, SOC, SOH, and temperature. There are different methods for modeling batteries, for example, 1) electrochemical modeling [18], and 2) equivalent circuit modeling [18]. Electrochemical modeling provides a deep understanding of the chemical and physical process inside the battery and is useful when building a cell or pouch cell, but high computational time makes this approach impractical for applications that involve multiple pouch cells, such as vehicle battery packs. On the other hand, in equivalent circuit modeling, battery losses are represented in terms of electrical circuit components, making this method more efficient in terms of computation.

1.5 Research Objectives

Given the problems of 1) battery performance, 2) aging or degradation of batteries, and 3) fire issues, all due to high battery operating temperature as identified in the previous section, and given our limited knowledge of the thermal behaviour of vehicle batteries, it is quite important to do more research on performance of PHEV, HEV, and EV batteries undergoing realistic vehicle charge and discharge cycles. To date, a lot of work has been done on battery modeling but limited published work exists experimentally with varying boundary conditions. So, one of the

key objectives in this research is to characterize the thermal behavior of a vehicle suitable pouch cell using dual cold plates to provide a large range of boundary conditions. Consequently, the objectives of this research work are as follows:

OBJECTIVES:

1) To characterize the thermal behaviour of batteries
2) To develop and validate an empirical battery thermal model in MATLAB Simulink.
3) To characterize the thermal behaviour of vehicle batteries under realistic drive cycles.

In order to fulfill the above mentioned objectives, empirical data, including battery voltage, current, temperature, heat flux, and heat generation, are required. A thermal boundary condition test apparatus is designed and developed to generate the data of interest. In addition, in-situ vehicle data is collected to enable characterization of vehicle batteries undergoing real-world drive cycles by outfitting three different industry partner (Burlington Hydro) vehicles using different propulsion technology (one EV, and two HEVs) with data loggers and a data reporting infrastructure. The data from each part is used in development of battery thermal models.

The first empirical battery thermal model is developed based on data collected from the thermal boundary condition test apparatus. The acquired data is incorporated into a look up table along with algorithms written in MATLAB Simulink.

The second model developed is a vehicle drive train model (which can be used to determine vehicle performance) in PSAT/Autonomie software. The in-situ vehicle data collected for the converted EV of Burlington Hydro is used to provide validation of the model. Ultimately the aim is to improve understanding EV operation, provide insights into design improvements, and evaluate the degradation in performance due to non-optimal operation.

Specific experiment milestones are as follows:

A. To design an apparatus that measures
   i. The surface temperature distribution at various charge/discharge profile from different types of batteries of different chemistry,
   ii. The heat flux near the cathode, the anode, and at the center of the pouch cell along the height of the pouch cell, and

iii. The heat rejection to the dual cold plates under various discharge rates with different boundary conditions.

B. To visually observe and report the locations of highest heat generation and temperature distribution using IR imaging techniques.

C. To determine the effect of discharge rates and operating temperature on the battery discharge capacity.

D. To outfit three Burlington Hydro Ford Escape Vehicles (One pure EV and two HEVs) with data loggers:

   i. To collect driving, battery and powertrain data from a pure EV, in order to analyze the vehicle performance.

   ii. To characterize the thermal behaviour of Li-ion battery in terms of temperature and power from lab battery versus vehicle battery, using real drive cycles from pure EV.

   iii. To collect driving data from two HEVs in addition to the EV in order to compare and evaluate the capability of an EV to serve as a fleet vehicle.

1.6 Document Organization

Chapter 1: introduces the research objectives along with the motivation and challenges.

Chapter 2: reviews related research in battery.

Chapter 3: presents work performed to date, Part-I: Design of a thermal boundary condition test apparatus which measures the thermal characteristics of a battery, results & discussion

Chapter 4: presents work performed to date, Part-II: Installation of three data loggers in three different vehicles, data collection and analysis

Chapter 5: presents model development and validation based on part-I and part-II.

Chapter 6: presents conclusions, recommendations, and summary of contributions

Chapter 7: presents an experimental uncertainty analysis

Chapter 2

Background and Literature Review

The focus of this research is on thermal management and thermal characterization of Li-ion battery for EVs and HEVs. In this chapter background information about the battery including chemistry and glossary, thermal management of batteries, thermal measurements via thermocouples and calorimeters, IR image, battery modeling, and degradation mechanism are discussed.

2.1 Batteries

The commercially available and widely used rechargeable batteries are lead-acid, nickel cadmium, nickel metal hydride, lithium ion, and lithium ion polymer batteries. Lithium ion batteries are a relatively new battery technology currently undergoing immense growth and development. They have already become the preferred battery type for applications requiring high energy densities and light weight, such as portable media players and smartphones [19] . There is also a shift in the expanding hybrid vehicle market towards lithium chemistries and away from NiMH batteries. In 2009, rechargeable lithium batteries accounted for 11% of the $16.4 billion total US demand and is expected to be the fastest growing chemistry type through 2012 [20]. The 2008 European lithium rechargeable market was similarly sized at $1.62 billion and is expected to grow to $1.76 billion by 2015 [21]. Notable deployments of Li-ion batteries in the automotive market include the Chevrolet Volt, which is a range-extending electric vehicle (RE-EV), and the Nissan Leaf, which is a battery electric vehicle (BEV). Table 1 presents characteristics of different battery types used in PHEVs and EVs.

A lithium ion battery offers advantages over other battery types in several areas. It has a high operating voltage of 3-5 volts, depending on the specific chemistry. This allows for an equivalent power operation at a lower current draw and the battery will last longer on a single charge. It has a high energy density, so lithium ion batteries are lightweight and compact. Unlike NiCad and

older NiMH batteries, Li-ions do not exhibit any memory effect, and they have long shelf lives – up to 5 years. Additionally, they are capable of high discharge rates with high reversibility and good charge retention. The disadvantages of Li-ion batteries are the high cost and safety issues. The term 'Lithium-ion' include a number of different chemistries; Table 2 shows some of the chemistries under development in EVs. In Figure 2 a comparison is given between the best EV suitable Li-ion batteries.

Table 1- Characteristics of battery types used in EVs [22]

Characteristic	Lead Acid	NiMH	ZEBRA	Li-ion
Nominal cell voltage	2 v	1.2 v	2.58 v	2.5 v/ 3.3 v/ 3.6-3.7 v
Specific energy	30-45 Wh/kg	30-80 Wh/kg	90-100 Wh/kg	90-220 Wh/kg
Energy density	60-75 Wh/L	140-300 Wh/L	160 Wh/L	280-400 Wh/L
Specific power	180 Wh/kg	250-1000 Wh/kg	150 Wh/kg	600-3400 Wh/kg
Cycle life	500-800	500-1000	1000	1000-8000
Self-discharge	2-4% /month	20-30% /month	0% /month	2-5% /month
Temperature range	-20-60 ℃	-20-60 ℃	270-350 ℃	-20-60 ℃
Relative costs	Low	Moderate	Low	High

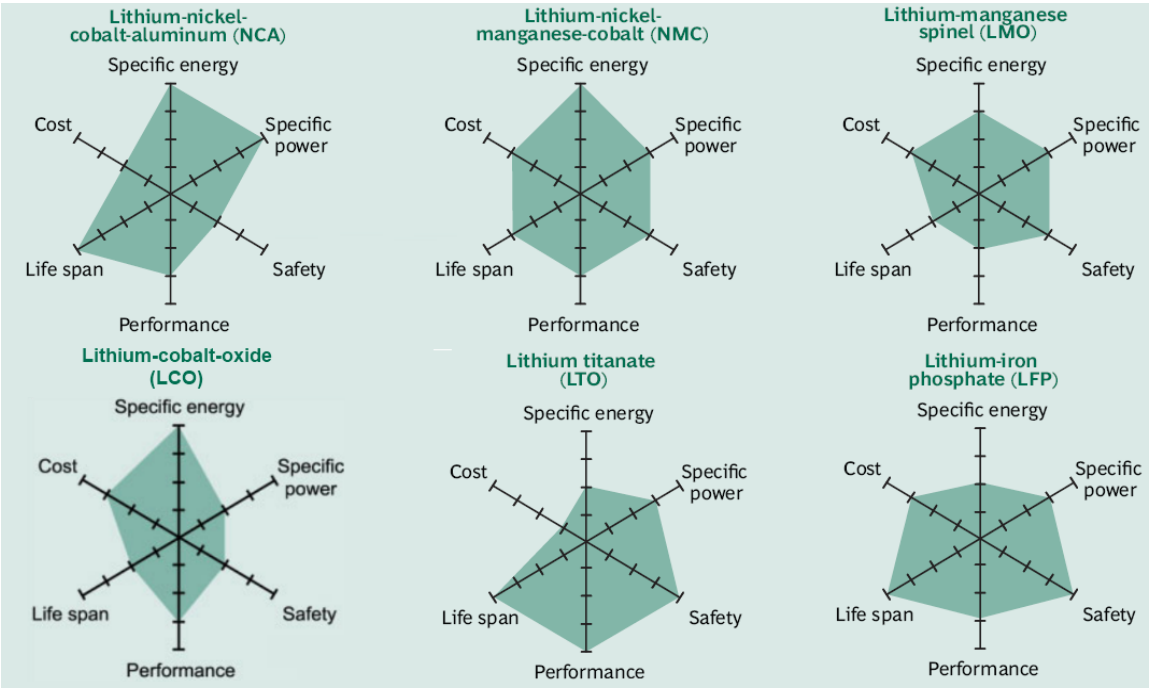

Figure 2 : Comparison of suitable Li-ions for EV. The more the colored shape extends along a given axis, the better the performance in that direction [23]

Table 2- Examples of different Li-ion batteries used in EVs [24]

Developer	Chemistry	Vehicle	Year
A123	Doped Lithium nanophosphate	Volt-EV Vue-PHEV Think	2010 2009 2009
Panasonic JCI-Saft	Lithium nickel cobalt Aluminum oxide	Toyota-PHEV S400-HEV Vue-PHEV	2010 2009 2009
Hitachi	Lithium cobalt oxide	GM-HEV	2010
Available Cells	Lithium manganese Oxide	Tesla-EV	2008
Altair Nanotechnologies	Lithium titanate spinel	Phoenix Electric	2008
EnerDel	Lithium manganese Titanate	Think	2009
Compact (LG) NEC	Manganese spinel	Volt-EV Nissan-EV	2010 2010

The most common Li-ion type in small consumer electronics (laptops-cell phones) is lithium-cobalt-oxide ($LiCoO_2$/LCO) due to its high specific energy. Tesla Motors uses laptop sized LCO cells in their EVs combined with a liquid cooling system safety issues; but low specific power and life span prevents this type to be a good choice for EVs [25]. Lithium-iron-phosphate ($LiFePO_4$/LFP) on the other hand does not experience thermal runaway and has almost no fire hazards, since no oxygen is released at high temperatures [26]. $LiFePO_4$ cells have good life span, low costs per Ah and kW [26, 27], good power capabilities and are extremely safe, but the specific energy is low and the performance is poor at low temperatures.

The batteries can either be of high power density type or high energy density type. Power density provides a good measure on how much energy can be released due to discharge at a given time with regards to kg or liters. Energy density is the amount of energy with regards to kg or liters. A high energy density battery is useful in applications where a longer driving distance is required e.g. in a PHEV which is intended to be driven on pure electricity for longer distances. A high power density battery is useful in an application where a short but intensive power pulse is required; e.g. in an ordinary HEV as the electric motor often only assists the combustion engine in short periods [28].

2.2 Li-ion Cell Operation

A Li-ion battery cell consists of two electrodes, anode and cathode, with a separator in between, and current collectors on each side of the electrodes. The cathode is made of a composite material and defines the name of the Li-ion battery cell. The anode is usually made out of graphite or a metal oxide. The electrolyte can be liquid, polymer or solid. The separator is porous to enable the transport of lithium ions and prevents the cell from short circuiting and thermal runaway [29]. Figure 3 shows composition of Li-ion battery.

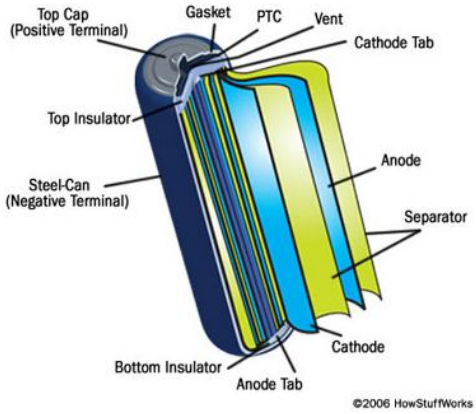

Figure 3: Composition of a cylindrical Li-ion battery [30]

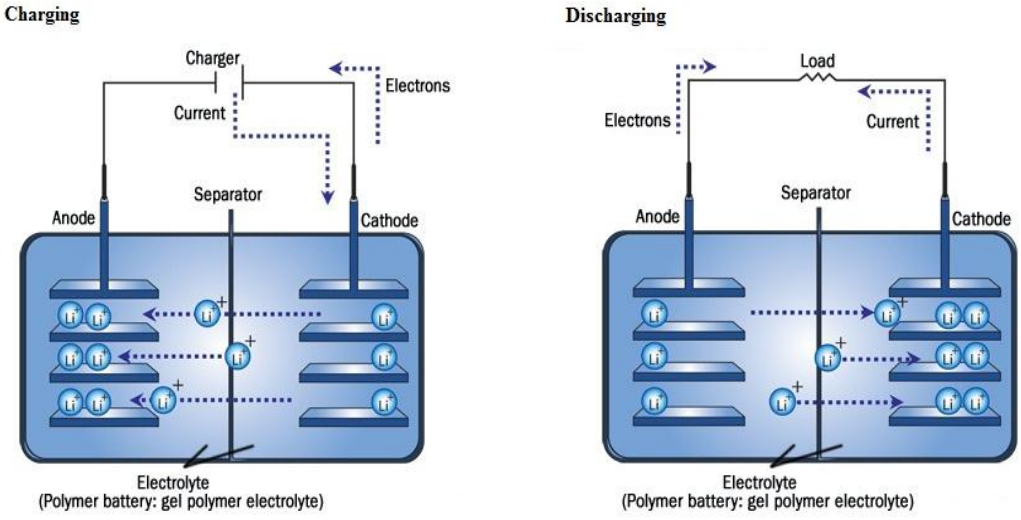

Figure 4: Charge and discharge mechanism in Li-ion battery [30]

During discharge the lithium ions diffuse from the anode to the cathode through the electrolyte. The lithium ions will intercalate (Intercalation refers a reversible chemical process of binding a

molecule between other molecules. Deintercalation is the reversible process) into the cathode, causing the cathode to become more positive. Due to the potential difference between the cathode and anode, an electric current will flow through the external circuit, supplying power to the load. During charging the opposite effect occurs. The current will cause the lithium ions to deintercalate from cathode and diffuse to the anode. At the anode intercalation of the lithium ions occurs, charging the battery. These processes are shown in Figure 4 for a Li-ion cell.

2.3 Cathode

Cathode materials are usually a metal oxide capable of intercalating lithium ions. For the cathode, it is important to hold large amount of lithium without significant change in structure, have a good chemical and electrochemical stability with electrolyte, be a good electrical conductor and diffuser of lithium ions, and be of low cost. The thermal stability and the rate capability of the battery is also largely dependent on the cathode material [31].

$LiCoO_2$: $LiCoO_2$ is most the most commonly used cathode material [32] shown in Figure 5. Lithium ions are intercalated between sheets of CoO_2 is 274 mAh/g, but an anisotropic structural change occurs at $Li_{0.5}CoO_2$, so the realizable capacity is limited to about 140-160 mAh/g [33-36]. Coatings like $AlPO_4$ have been developed to improve capacity retention and thermal stability [31]. The discharge capacity of $LiCoO_2$ is good; 136 mAh/g at a 5C rate has been demonstrated with multiwalled carbon nanotubes (CNT) augmented cathodes [36]. However, cobalt is relatively expensive compared to other transition metals such as manganese and iron, despite the attractive electrical properties of $LiCoO_2$ cathodes.

$LiMn_2O_4$: $LiMn_2O_4$ is a promising cathode material with a cubic spinel structure, shown in Figure 6. In the figure, the corners of each tetrahedral and octahedral are oxygen atoms. The theoretical specific capacity is 148 mAh/g. Current designs achieve between 115 and 130 mAh/g at modest discharge rates of 1C or less [37-39]. $LiMn_2O_4$ nanowire cathodes have been demonstrated to have excellent high power capabilities of 107 and 102 mAh/g at 5C and 10C, respectively and with virtually no capacity loss after 100 cycles. Other transition metals like Ni, Co, and Fe can also be added to $LiMn_2O_4$ in varying amounts to increase capacity and improve capacity retention during cycling [32].

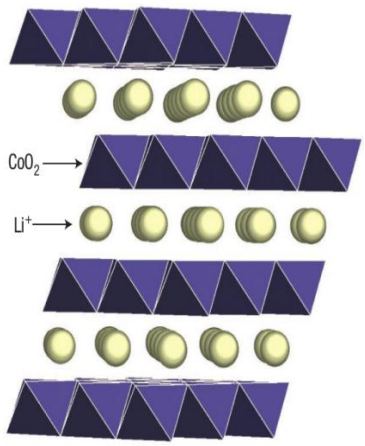

Figure 5 : Layered structure of $LiCoO_2$ [40]

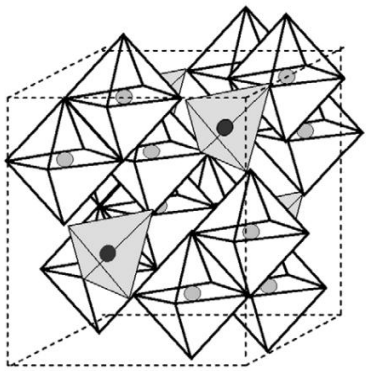

Figure 6 : Cubic crystal structure of $LiMn_2O_4$ [41]

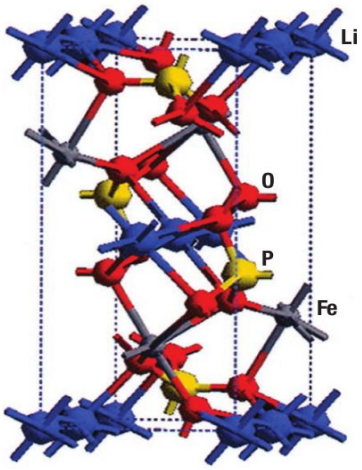

Figure 7 : Olivine structure of $LiFePO_4$ [42]

$LiFePO_4$: $LiFePO_4$ is one of the most recent cathode materials to be introduced. Its olivine structure, shown in Figure 7, is very different from the layered and spinel structures of other lithium ion chemistries, and its intercalation mechanism is also different, involving phase changes. It has a theoretical specific capacity of 170 mAh/g, a figure which has been approached by recent advances [43]. A composite material such as $LiFePO_4$/C with a nano-carbon wire network has been shown to have excellent high rate performance, achieving 129 mAh/g at a 10C rate and retaining over 90% of its capacity after 400 cycles at 10C [44]. $LiFePO_4$ has the added advantage of being inexpensive and environmentally friendly.

2.4 Anode

Anode materials are typically carbonaceous in nature. It is important for the anode, similarly to cathode, to be able to hold large amounts of lithium without significant change in structure, have good chemical and electrochemical stability with the electrolyte, be a good electrical and ionic conductor, and be of low cost.

Graphite: Today, graphite is one of the most common anode materials in lithium ion batteries, stacked in layers. It undergoes a reversible lithium-intercalation reaction from 0 to 0.2 V vs Li/Li+ and is favoured for its small volume change during lithiation and delithiation [45]. With graphite anodes, high coulombic efficiencies of over 95% have been achieved, but they have a relatively low theoretical specific capacity of 372 mAh/g [46]. Although this is already higher

than the specific capacity of the commonly used cathode materials, higher specific capacity anodes are still desirable because they contribute to a lower overall battery density.

Among carbonaceous materials, CNTs are the most promising materials being developed. Purified CNTs of the single walled variety can reversibly intercalate lithium ions with a maximum composition of $Li_{1.7}C_6$, equivalent to 632 mAh/g. Etching can increase the reversible capacity to 744 mAh/g, and capacities as high as 1000 mAh/g have been reported using ball milling treatments [47]. Multiwalled CNTs have a reported reversible capacity of up to 640 mAh/g. Although CNTs have high reversible capacities, they also have large irreversible capacities as high as 1488 mAh/g for purified single walled CNTs [47]. This lithium, which cannot be cycled, causes growth of SEI and reduces overall capacity. Two major issues that must be solved before CNT anodes can be widely adopted are excessive irreversible capacity and methods of large-scale fabrication [48].

Silicon: Silicon is another leading alternative anode material to carbon and has been extensively researched. Pure Si anodes alloy readily with lithium and have a huge theoretical capacity of 4200 mAh/g, but are impractical as they undergo great volumetric changes and thus have poor cycleability. Composite materials have been developed to mitigate the effects of mechanical stresses of lithiation and delithiation. One method is to house the active silicon material in inert matrices made of materials such as C (e.g. graphite, pitch, CNTs), TiC, SiC, TiN, or Cu/C. The inactive matrix absorbs the mechanical stresses and strains experienced by the active phase, resulting in improved cyclability. Nanowires have also been proposed as an anode material because lithium diffusion occurs only in one dimension and mechanical stresses can be well accommodated. Low cyclability even at small currents and significant irreversible capacities remain challenges in the development of silicon based anodes [48].

2.5 Separator

Lithium-ion cells use separator called microporous film to prevent the physical contact between the Cathode and Anode while permitting free ion flow. The battery performance can be adversely affected by the presence of separator material as it increases electrical resistance as well as battery density [49]. Therefore, care must be taken in order to select an appropriate material. Commercially available liquid electrolyte cells use microporous polyolefin materials,

such a polyethylene (PE) or polypropylene (PP). The Li-ion separators include following requirements [50]:

- High machine direction strength to permit automated winding
- Does not yield or shrink in width
- Resistant to puncture by electrode materials
- Effective pore size less than 1 μm
- Easily wetted by electrolyte
- Compatible and stable in contact with electrolyte and electrode materials

Currently available microporous polyolefin separator materials are either homogenous or a laminate of polyethylene and polypropylene. Pore sizes of 0.03 to 0.1 μm, and 30 to 50% porosity are commercially available [50]. The separator films form an important element of battery in an over temperature scenario. The low melting point of polyethylene (PE) materials enables their use as a thermal fuse. As the temperature rises to the softening point of the polymer, the membrane begins to shrink, and consequently pore size is reduced. The flow of Li+ ions is disrupted and the reaction rate is decreased. If the temperature continues to rise, the separator is required to be capable of shutting down the reaction entirely, below the thermal runaway threshold. For currently utilized PE-PP bilayer separators shutdown occurs at about 130 °C and melting occurs at about 165 °C [49].

2.6 Current Collectors

Current collectors comprise the component of the battery responsible for transferring the flow of electrons from the electrodes to an external circuit [50]. Several types of current collectors are available: mesh, foam, and foil. To minimize overall size and improve volumetric capacity of cells, metallic foils which are thin and light are preferred. Current collectors are an electrochemically inactive volume in the cell, but form the substrate that the electrochemically active materials are applied to. Active materials are applied onto the thin current collectors with a conducting agent and an adhesive binder. Hence, current collectors should possess high electrical conductivity to reduce cell resistance as well as chemical stability in contact with liquid electrolyte over the operation voltage window of electrodes [51]. Different current collectors can result in significant difference on the performances of the lithium ion batteries [52]. The most

commonly utilized current collectors in commercial batteries are: copper foil for the positive electrode (Cathode), and aluminum foil for the negative electrode (Anode) [53].

2.7 Electrolyte

The choice of electrolyte in lithium ion batteries is critical for the performance as well as the safety. The electrolyte is typically a lithium salt dissolved in organic solvents. A good electrolyte must have low reactivity with other cell components, high ionic conductivity, low toxicity a large window of electrochemical voltage stability (0-5V), and be thermally stable.

Typically, for lithium ion batteries, in liquid electrolytes, a mixture of alkyl carbonates such as ethylene carbonate (EC), diethyl carbonate (DEC), dimethyl carbonate (DMC), and ethyl-methyl carbonate (EMC) is used with $LiPF_6$ as the dissolved lithium salt. EC is a necessary component for adequate solid electrolyte interface (SEI) growth. Many lithium salts are possible, but it is difficult to find one that is chemically stable, safe, and forms a high conductivity solution. $LiPF_6$ offers the best compromise between these criteria and has been the long-time standard in lithium ion batteries. Some of the well-known salts and their major disadvantages are shown in Table 3 [54].

Table 3 : Well-known lithium salts for use in electrolytes & their major disadvantages [54]

Salt	Disadvantages
$LiAsF_6$	Toxic
$LiClO_4$	Thermal runaway leading to explosion
$LiBF_4$	Interferes with anode passivation
$LiSO_3CF_3$	Low conductivity
$LiN(SO_2CF_3)_2$	Corrodes aluminum cathode current collector
$LIC(SO_2CF_3)_3$	Corrodes aluminum cathode current collector
$LiPF_6$	Thermally decomposes to HF and PF_3O, deteriorates both anode and cathode

The main objective of electrolyte development has been to improve the thermal operating range of lithium ion batteries. Current batteries rapidly deteriorate above 60 ^{0}C. High operating temperatures are very desirable in high discharge applications where the amount of cooling available is limited, such as on electric vehicles.

Certain boronate salts have been found to improve thermal stability, particularly an unsubstituted five member ring salt known as lithium bisborate (LiBOB). Cells using this salt were

successfully cycled at 60 ^{0}C without degradation, but the salt is difficult to prepare [55]. A combination of $LiPF_6$ + $LiPF_3$ $(CF_2CF_3)_3$ salts have also been proposed which maintain cyclability even after 100 cycles at 80 C with moderate capacity loss [54]. LiBOB has been investigated as an additive to standard $LiPF_6$ based electrolytes and was observed to stabilize the SEI, reduce degradation of cathode materials and improve overcharge tolerance [56].

Ionic liquids have also been proposed as an alternative to alkyl solvents as they are generally good flame retardants and have low heats of reaction. In addition to enhanced safety, ionic liquids have very high ion concentrations, so transport kinetics is favourable. However, ionic liquids are expensive and do not tend to facilitate SEI formation, so they are only stable at lower voltages [55].

2.8 Battery Glossary

Some basic definitions related to Li-ion battery are presented in this section.

Cell, modules, and packs – Hybrid and electric vehicles have a high voltage battery pack that consists of individual modules and cells organized in series and parallel. A cell is the smallest, packaged form a battery can take and is generally on the order of one to six volts. A module consists of several cells generally connected in either series or parallel. A battery pack is then assembled by connecting modules together, again either in series or parallel. An exploded view of A123 prismatic battery module and pack is shown in Figure 8. A battery pack comprised of A123 modules is shown in Figure 9.

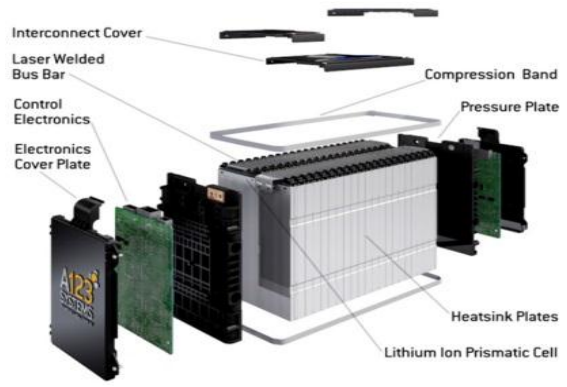

Figure 8 : Exploded view of A123 25S2P prismatic module [57]

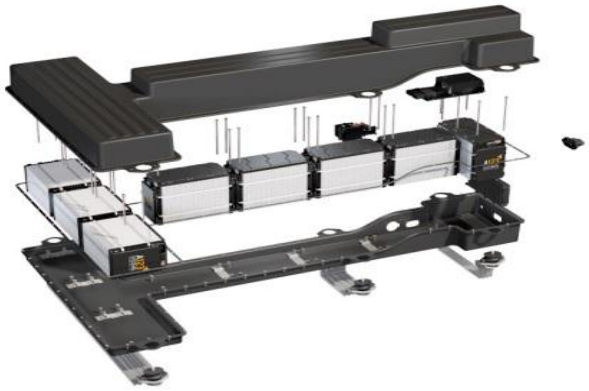

Figure 9 : Battery pack comprised of A123 modules [58]

Secondary and Primary Cells – Batteries for hybrid, plug-in, and electric vehicles are all secondary batteries. A primary battery is one that cannot be recharged. A secondary battery is one that is rechargeable.

C and E-rates - The charge and discharge current of a battery is measured in C-rate. Most portable batteries are rated at 1C. This means that a 100 Ah battery would provide 100A for 1 hour if discharged at 1C rate. The same battery discharged at 0.5C (1/2C) would provide 50A (100 x 0.5=50) for 2 hours. At 2C, the 100Ah battery would deliver 200A for 1/2 hour (30 minutes). 1C is often referred to as a 1 hour discharge; a 0.5C would be 2 hour and 0.1C a 10 hour discharge. Similarly, E-rate describes the discharge power. A 1E rate is the discharge power to discharge the entire battery in 1 hour.

State of charge (SOC) - The state of charge refers to the amount of charge in a battery relative to its predefined "full" and "empty" states i.e. the amount of charge in Amp-hours left in the battery. Manufacturers typically provide voltages that represent when the battery is empty (0% SOC) and full (100% SOC). SOC is generally calculated using current integration to determine the change in battery capacity over time.

Depth of discharge (DOD) – It is a measure of how much energy has been withdrawn from a battery and is expressed as a percentage of full capacity. For example, a 100 Ah battery from which 40 Ah has been withdrawn has undergone a 40% depth of discharge (DOD). Depth of discharge is the inverse of state of charge (SOC). A battery at 60% SOC is also at 40% DOD.

State of health (SOH) - The state of health (SOH) is a measure of the condition of the battery compared to its initial or ideal state, measured in percentage points. i.e. The state of the battery between the beginning of life (BOL) and end of life (EOL) in percentage. The EOL of a battery is reached when the battery cannot perform according to the minimum requirement. There is no universally accepted method of characterizing SOH. Any of the following, in single or in combination, might be used: internal resistance, impedance/conductance, capacity, voltage, ability to accept charge, and number of charge/discharge cycles.

Cycle life - Cycle life refers to the number of times a battery must be charged and discharged before its nominal capacity falls below 80% (or some other predetermined threshold) of its rated value. Cycle life is given for a particular DOD and determined at specific charge and discharge conditions. Typically, higher DOD translates to a lower life cycle.

Open Circuit Voltage (OCV or Voc) - The open circuit voltage (OCV) is the voltage when no current is flowing in or out of the battery, and, hence no reactions occur inside the battery. OCV is a function of state-of-charge and is expected to remain the same during the life-time of the battery. However, other battery characteristics change with time, e.g. capacity is gradually decreasing as a function of the number of charge-discharge cycles.

Terminal Voltage (V) - The voltage between the battery terminals with load applied. Terminal voltage varies with SOC and discharge/charge current.

Nominal Voltage (V) - The reported or reference voltage of the battery, also sometimes thought of as the "normal" voltage of the battery.

Cut-off Voltage (V) - The minimum allowable voltage. It is this voltage that generally defines the "empty" state of the battery.

Charge Voltage (V) - The voltage that the battery is charged to when charged to full capacity. Charging schemes generally consist of a constant current charging until the battery voltage reaching the charge voltage, then constant voltage charging, allowing the charge current to taper until it is very small.

Float Voltage (V) - The voltage at which the battery is maintained after being charged to 100% SOC to maintain that capacity by compensating for self-discharge of the battery.

Capacity or Nominal Capacity (Ah for a specific C-rate) – The coulometric capacity, the total Amp-hours available when battery is discharged at a certain discharge current (specified as a C-rate) from 100% SOC to the cut-off voltage. Capacity is calculated by multiplying the discharge current (in Amps) by the discharge time (in hours) and decreases with increasing C-rate.

Energy or Nominal Energy (Wh (for a specific C-rate)) – The "energy capacity" of the battery, the total Watt-hours available when battery is discharged at a certain discharge current (specified as a C-rate) from 100% SOC to the cut-off voltage. Energy is calculated by multiplying the discharge power (in Watts) by the discharge time (in hours). Like capacity, energy decreases with increasing C-rate.

Specific Energy (Wh/kg) - The specific energy of a battery is expressed as a nominal energy per unit mass, such as Wh/kg. It is highly dependent on the battery chemistry and packaging.

Specific Power (W/kg) - The Specific power of a battery is expressed as a nominal power per unit mass, such as W/kg or kW/kg. It is highly dependent on the battery chemistry and packaging.

Energy Density (Wh/L) - The energy density of a battery is expressed as a nominal energy per unit volume, such as Wh/L. It is highly dependent on the battery chemistry and packaging.

Power Density (W/L) - The power density of a battery is expressed as a nominal power per unit volume, such as W/L or kW/L. It is highly dependent on the battery chemistry and packaging.

Internal resistance- The internal resistance is sometimes considered as the ohmic resistance of the cell, which is the direct voltage change after application of a current step on a cell in equilibrium [59]. Another definition for the internal resistance is the sum of the ohmic, activation and diffusion polarization resistances [60], which is the largest possible voltage drop in the cell. Nevertheless, the result in power dissipation in the form of heat will result due to the complete voltage drop. The voltage drop can be mainly divided as:

- IR drop is due to the current flowing across the internal resistance of the battery, by ohmic resistance.
- Activation polarization refers to the various retarding factors inherent to the kinetics of an electrochemical reaction, like the work function that ions must overcome at the junction between the electrodes and the electrolyte.
- Concentration polarization takes into account the resistance faced by the mass transfer (e.g. diffusion) process by which ions are transported across the electrolyte from one electrode to another.

Figure 10 depicts the typical polarization curve of a battery with the contributions of all three of the above factors shown as a function of the current drawn from the cell. Since, these factors are current-dependent, the voltage drop caused by them usually increases with increasing output current. The internal resistance of a battery is dependent on temperature, C-rate and SOC. Different values for the internal resistance can be found depending on the measurement method [61]. This is caused by the time constants associated with the activation and diffusion polarization resistances; whether the battery electrodes are in equilibrium or not is also important in determining the value of the internal resistance.

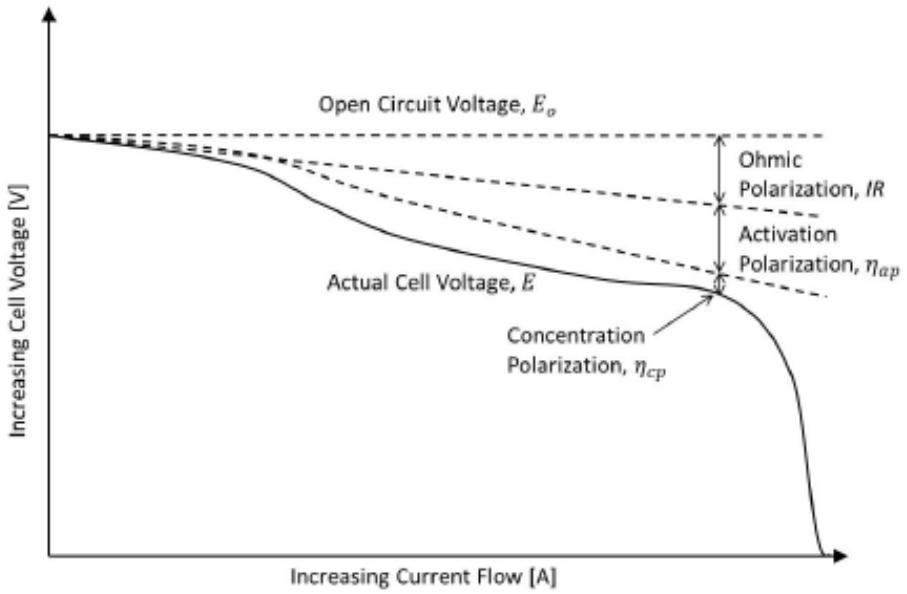

Figure 10 : Typical polarization curve of a battery [62]

2.9 Types of Lithium-ion Batteries

There are several types of configurations available for lithium-ion battery construction. The most prominent types are coin (wrist watch batteries and computer batteries), cylindrical (TV remote control batteries and vehicle batteries) and prismatic (vehicle batteries). Coin and cylindrical types are most commonly used in consumer electronics, and have been the subject of the earlier works in the battery electrochemical field. Usually, cylindrical cells designs are limited to below 4 Ah and prismatic cells designs are used for higher capacity ratings [50]. Stacked prismatic batteries consist of many individual cells with electrical connections to a common negative and positive current tab. A schematic representation of this is shown in Figure 11. Alternating sheets of positive and electrode current collector sheets are stacked between sheets of separator, such that the current tab of each positive sheet and each negative sheet are aligned on opposite sides. Both sides of the electrode sheets form electrochemical cells with adjacent electrodes across the separator layers. An aluminum laminate material is used to form a pouch that the stack of cells is placed within. The current tabs present at the top of each current collector sheets are joined together and attached to a larger output tab that extends to the exterior of the pouch.

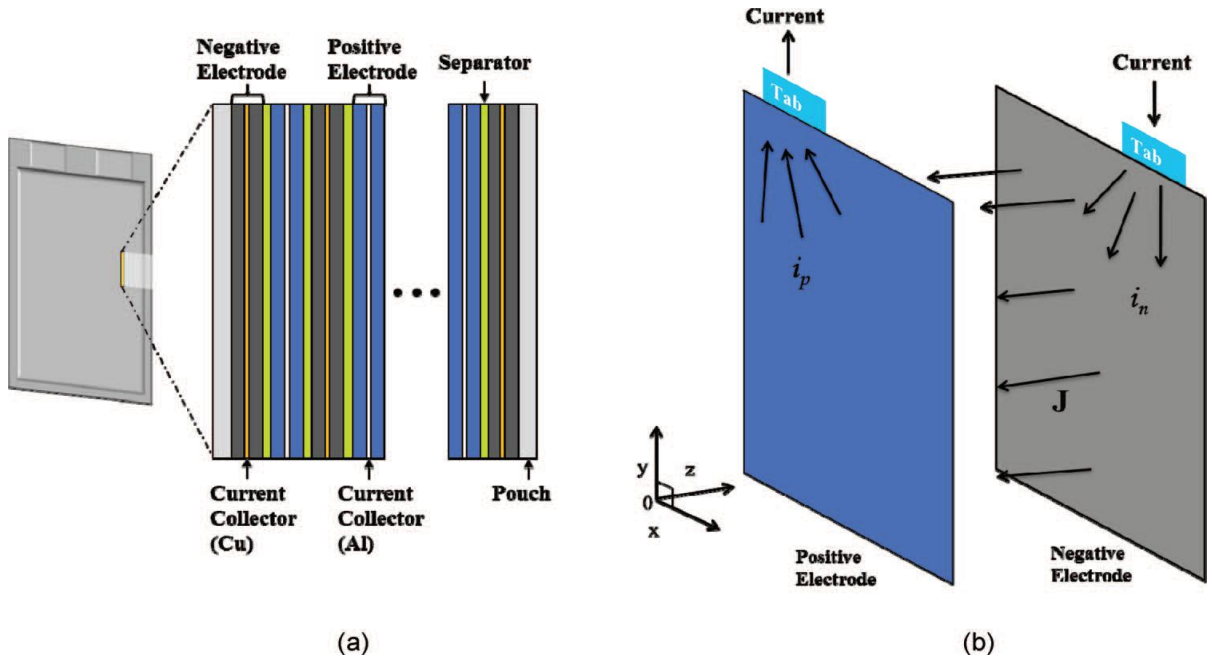

Figure 11 : Multi layered prismatic battery and current flow in a battery cell [63]

2.10 Thermal Management of Batteries

Thermal management of batteries is critical in achieving the desired performance in a low-temperature environment and the desired life in the high-temperature environment. The heat generated inside a battery must be dissipated to improve reliability and prevent failure [64]. Lithium ion batteries degrade rapidly at high temperatures, while cold temperatures reduce power and energy output, thus limiting their driving range or performance capabilities [65, 66]. A thermal management system is necessary in transportation applications in order to regulate the batteries to operate in the desired temperature range; and to reduce uneven temperature distribution [64]. In a battery pack, uneven temperature distribution could lead to electrically unbalanced modules which lower the performance of the pack and vehicle [67].

Many cooling systems, especially active ones, require heat to be rejected outside the vehicle, which requires additional flow ducting and a heat exchanger. Vehicles have limited physical space available and packaging can become an issue. Some air cooling techniques, such as those in the Toyota Prius, pass cooled cabin air (cooled by the vehicle's air conditioner) through the battery pack. In liquid or fin cooling systems, a secondary refrigeration loop to reject the heat may be needed [64]. Battery pack thermal management and control systems have been

demonstrated commercially and in the literature utilizing: air or liquid systems, insulation, phase-change materials, within both active and passive approaches. Several papers that investigate these various strategies are presented following:

2.10.1 Air Cooling

The main advantage of air cooling systems is their simplicity over liquid coolant systems. Another advantage is electrical safety. However, air cooling systems have a lower heat transfer coefficient, making it more difficult to achieve a uniform temperature on the pack. Liquid cooling systems, on the other hand, are more effective and occupy less volume, but have higher complexities, weight, and cost. Figure 12 depicts a schematic of battery thermal management system using air as a coolant fluid developed by Pesaran [68].

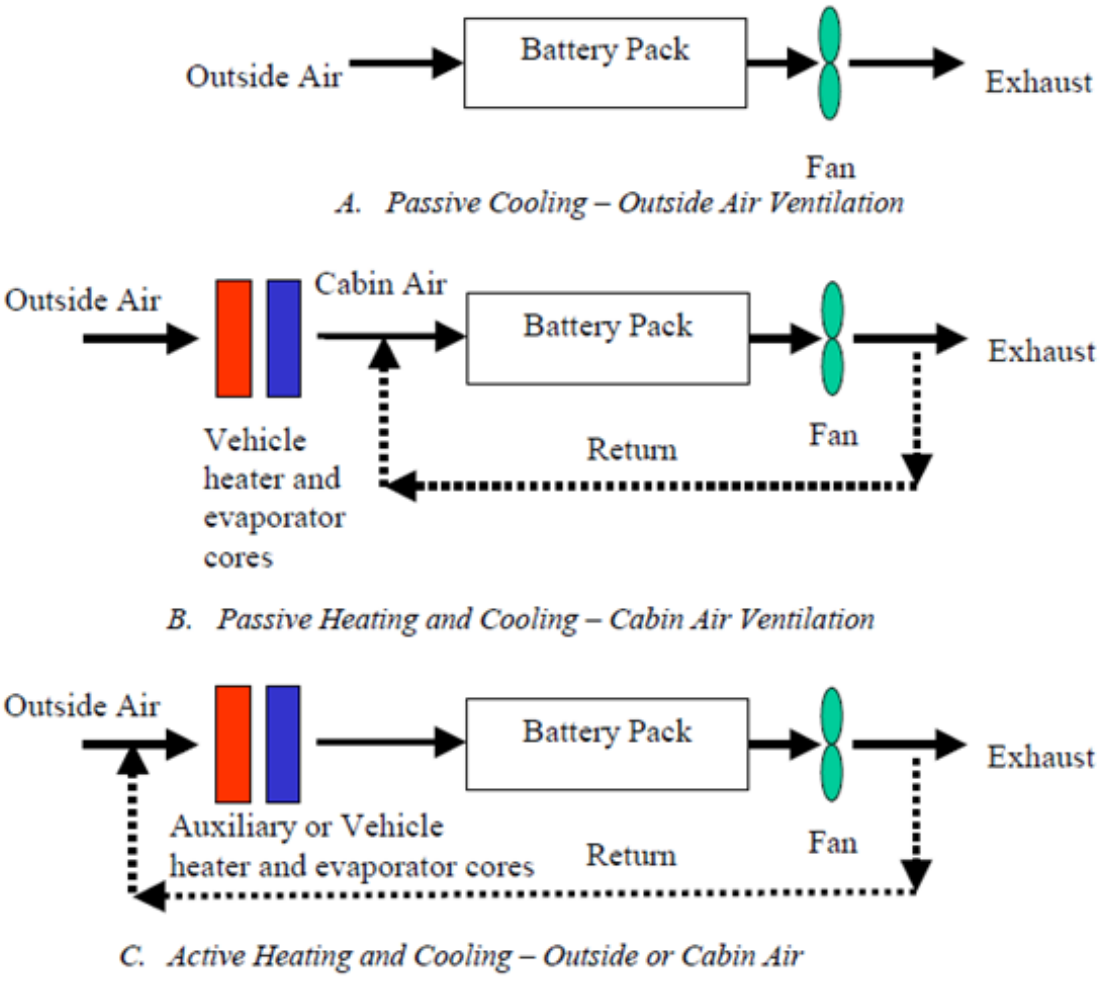

Figure 12 : Battery thermal management system (BTMS) using air [68]

Pesaran [68] divided the design process of a BTMS into seven general steps:

1. Define the design objectives and constraints of a BTMS
2. Obtain the module/pack heat generation and heat capacity
3. Preliminary analysis to select an initial strategy
4. Perform a detailed analysis to evaluate the impact of different parameters
5. Preliminary design of the BTMS
6. Build and test a prototype BTMS
7. Improve the BTMS

Pesaran [68] also described the pros and cons of different BTMSs, such as cooling system with series or parallel air distribution. He claimed that for parallel cooling, where the total air flow is split into equal portions, more uniform temperature distribution in the pack is achievable. Parallel configurations, however, require very careful design of air manifolds. Hence, large battery packs usually use a series-parallel configuration.

In a different approach to cooling channels, Sun et al. [69] modeled a battery pack to optimize cooling channel configuration. The pack was composed of stacks which were assembled beside each other. The air enters and exits the pack using the lower and upper ducts, respectively, and flows between the stacks to cool them down Figure 13. The simulations showed that the average temperature of the stacks close to the inlet and outlet of pack is lower compared to the farther locations shown in part (A). This was due to the uneven flow rate in the channels resulted from the pressure drops in the ducts. Therefore, the uniformity of flow rates was improved by tapering the upper duct shown in part (B). In this way, the temperature difference across the pack was reduced from 4 ^{0}C to 1.3 ^{0}C. The method presented in [69] is a good example of utilizing thermal models in BTMS development.

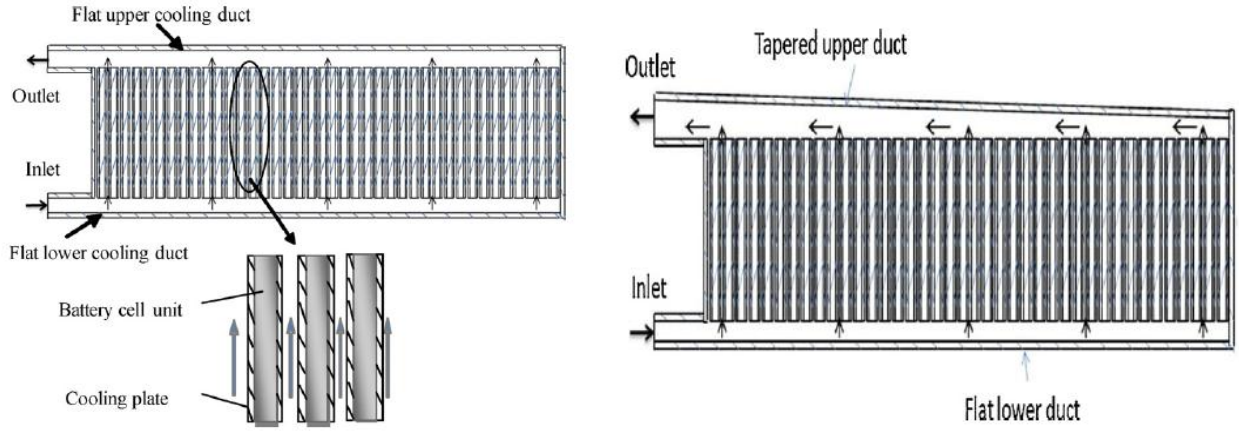

A) baseline "U-type" flow **B) tapered "U type" flow**

Figure 13: Schematic of a (A) baseline (B) tapered "U type" battery pack [69]

Yeow et al. [4, 70] also conducted a series of studies to improve cooling of Lithium-ion batteries using indirect methods. In the indirect method, the cooling fluid is not in direct contact with the battery while in the direct method the coolant flows over the surface of the battery. In this method, the coolant moves through a series of tubes embedded in a cold plate which is in contact with the battery or thermal fins. In their work, stacks were cooled using a thin aluminum plate in contact with the surface. The thermal fins extract heat from the stack and transfer it to the liquid cooled cold plates at the side of the stacks. Some parametric studies, such as the effect of employing one or two cold plates, were conducted on this BTMS [4].

Figure 14, (A) and (B) the measured and simulated cell temperatures under 2C discharge with single cold plate cooling is shown and, in (C) and (D) the heat rejections to single as well as dual cooling cold plate with boundary condition 1 at different discharge rates are shown. Figure 14 shows that the dual cold plate cooling had about twice the cooling capacity of the single cold plate cooling. He also concluded that the cell temperature distribution can be influenced significantly by the location of cold plate. Furthermore, they proposed a thermal fin which can rapidly conduct heat to the cold plates [70]. These fins contain embedded heat spreaders that improve the uniformity of temperature distribution on the stack surface.

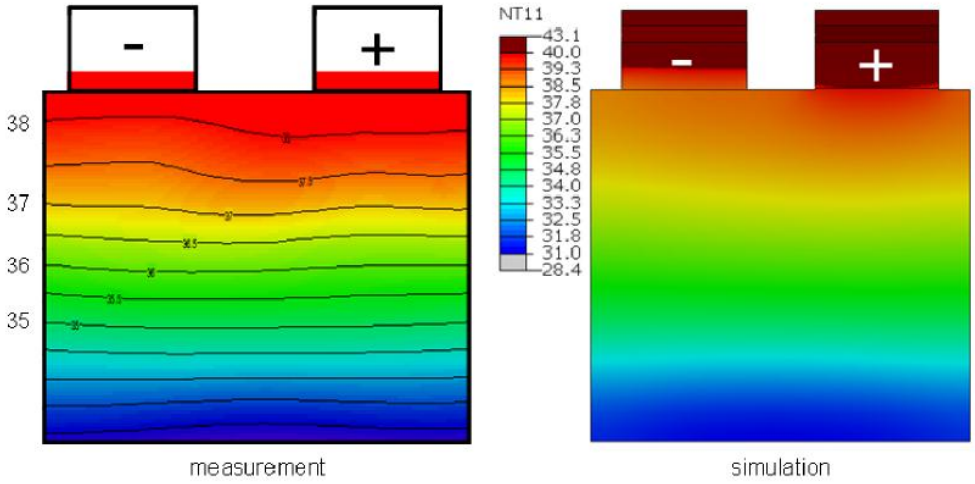

A: Measured **B: Simulated**

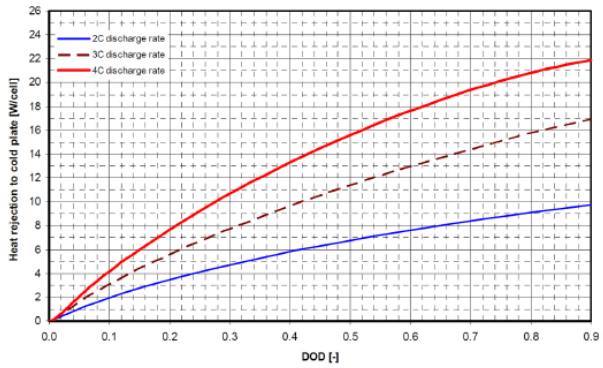

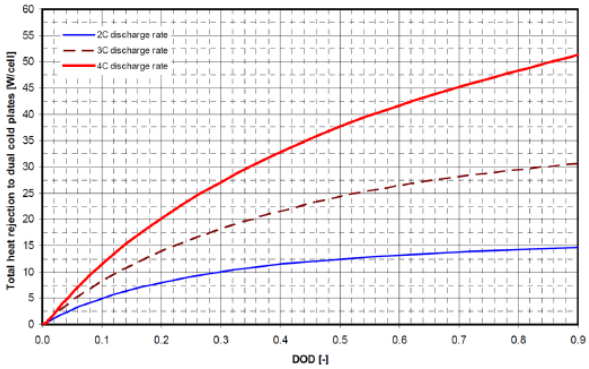

C: Single Cold Plate **D: Dual cold plate cooling**

Figure 14 : (A) and (B) Measured and simulated cell temperatures under 2C discharge with single cold plate cooling (C) and (D) Heat rejections to single and dual cold plate with BC1 boundary condition at different discharge rates [4]

2.10.2 Liquid Cooling

Active thermal management methods utilize forced fluid convection to absorb heat from individual batteries or subgroups of batteries within a pack. Karimi and Dehghen in their work [71], evaluated thermal management using both air and liquid cooling. A pack consisting of twenty, prismatic $LiCoO_2$-20 Ah batteries were modeled with a battery thermal model based on 1) ohmic heating and, 2) reaction entropy changes alone. A schematic of the modeled pack is shown in Figure 15 and a flow network model was used to determine the effect of several

coolant flows on the final temperature distribution of a pack undergoing constant current discharge. Air and silicon oil were chosen as a cooling medium in a battery pack.

Two flow configurations were modeled: a U-configuration, where flow enters and exits the same side of the pack casing, and a Z-configuration where the inlet and outlet are at opposite ends of the pack and on opposite sides of each end. The aim is to evaluate thermal distribution in the pack by measuring the standard deviation of temperature. Figure 16 compares temperature distribution at the end of 2C discharge rate in a battery pack.

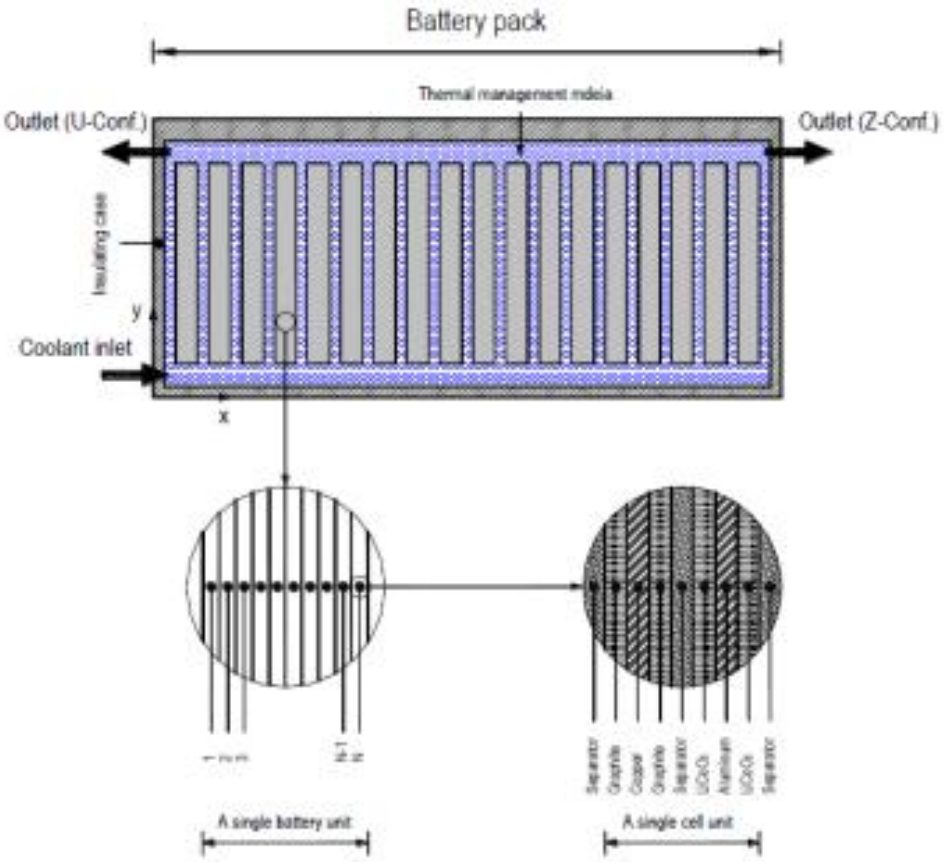

Figure 15: Schematic of Lithium-ion battery pack thermal management system [71]

Numerical results from the temperature distributions show that for both air and silicon oil, the Z-configuration for flow results in a more uniform temperature distribution than the U-configuration. Furthermore, silicon oil results in a much smaller temperature deviation (0.15 °C vs.7.33 °C after 2C discharge). The authors conclude that the penalty for the improved thermal control is that parasitic power is much higher for silicon oil, due to the high viscosity.

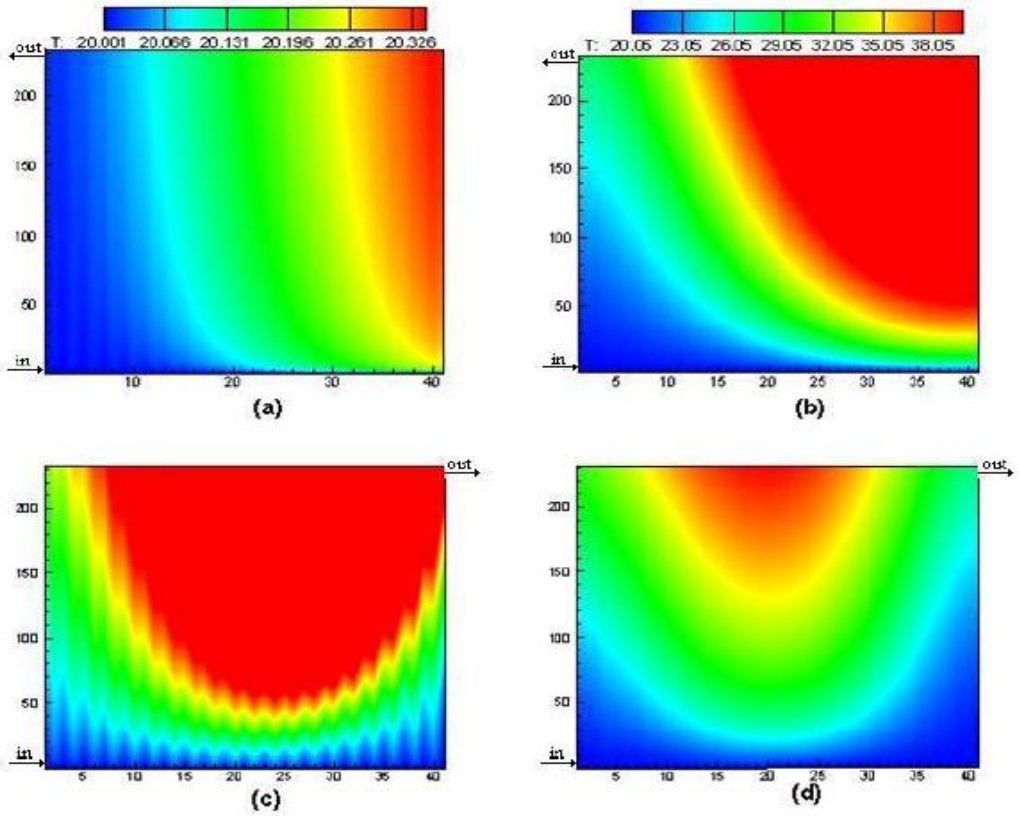

Figure 16 : Temperature distributions in a prismatic pack for 4 cooling. (A) Silicon oil, U-pattern, (B) Air, Z-pattern, (C) Silicon oil, Z-pattern, (D) Air, Z-pattern [71]

In addition to this study, the tab location and tab size are important and should be optimized for effective thermal management of batteries and cooling of battery pack. Kim et al. [72] investigated the effect of tab location on uniformity of temperature distribution on the battery. They concluded that placing positive and negative current collector tabs in the middle and on opposite sides of collectors is the best configuration as shown in Figure 17 (B). The configuration was shown to lead to a lower and more uniform temperature distribution compared to the configuration with tabs at the ends of the same side of collectors as shown in Figure 17 (A).

In another study, Kim et al [73] examined four different cell designs with different aspect ratios, and tab size and location. They showed that some measurable responses, like output potential, do not vary between cell designs. However, the internal kinetics and temperature distribution of the battery is significantly influenced. The author also found that the width of tabs has a minor effect

on temperature distribution, while increasing the surface area of the cells significantly raises the temperature non-uniformities on the battery surface.

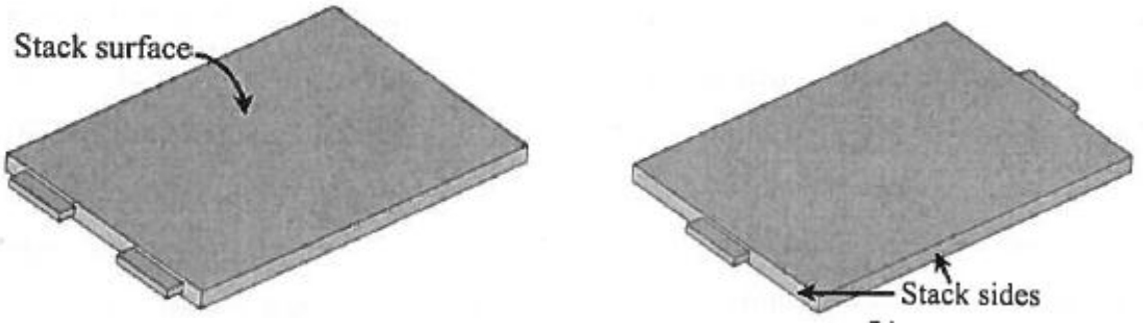

(A) Same side **(B) Opposite sides**

Figure 17 : Schematic representation of tab locations (A) same side, and (B) opposite sides

2.11 Experimental Works

In much of the literature, examples of empirical thermal measurements are performed merely to verify or evaluate a numerical model. In general, numerical models dominate the literature and a lack of experimentally research was noted especially research on the thermal experimentation. Empirical thermal studies found in the literature are summarized in the following subsections.

2.11.1 Thermal Measurements via Thermocouples

The most popular method of thermal parameter measurement is via direct measurement, which comprises measurement via contact between a sensing element and some part of a battery or battery containment structure. In most cases thermocouples are used, as illustrated by the following review of direct thermal measurement studies. Thermocouples are the most commonly used thermal sensors. Many thermal models are validated on the basis of matching the collected temperature data. Ye et al. [74] developed and validated a thermal model based on the battery surface temperature measurements. The experiment consisted measurement of the surface temperature of a prismatic battery (11.5 Ah) at a single location, the center of the battery's largest surface. The battery was discharged at various rates of 0.2C, 0.5C, 1C, and 2C inside a temperature-controlled box with several initial temperatures (0 °C, 10 °C, 25 °C, and 55 °C). To minimize heat transfer to the box and ambient air, insulation was wrapped around the battery.

The quasi-insulated allows the assumption that all heat generated remains within the battery, and the resulting temperature measured represents the total heat generated during operation.

Mi and Li in [75] presented numerical and analytical thermal results for a pack consisting of 48 batteries. The thermal response of an individual cell with a single thermocouple was measured as the battery underwent discharge. The measured response was used as an input heat term to a commercial FEA code. In the physical experiment, the battery was placed in a test chamber in a vertical position with natural convection cooling. A single thermocouple was used to measure the surface temperature of the battery, while another thermocouple monitored ambient temperature. This difference between the battery surface temperature and ambient temperature was used to quantify the heat dissipation by radiation and natural convection means. The total heat generated by a cell is given as equation (1).

$$Q_{gen} = A_{total} h_{rad}\left(T_{battery} - T_{air}\right) + 2A_v h_v (T_{battery} - T_{air}) \quad (1)$$

$$h_{rad} = \varepsilon\sigma(T_{battery}^2 + T_{air}^2)(T_{battery} + T_{air}) \quad (2)$$

$$Nu_L = \left[0.825 + \frac{0.387(Ra_L)^{1/6}}{\left\{1 + \left(0.492/Pr\right)^{9/16}\right\}^{8/27}}\right]^2 \quad (3)$$

The study assumed that the surface of the battery was painted black and the emissivity was 1, and the radiation heat transfer coefficient is given as equation (2). The author also used equation (3) known as Churchill and Chu Equation to calculate the Nusselt number.

In addition to this, researchers increase temperature data resolution by adding more thermocouples. Yang and Chen in [76] explained an experimental study on $LiFePO_4$/C prismatic 8 Ah batteries by placing the battery in the incubator and fixing 10 temperature probes on the battery surface. Within an incubator set to 25 °C, a single battery was charged and discharged at rates between 1C and 25C. The results were analyzed to determine the maximum temperature difference between locations of the battery (ΔT_{max}), and the average rate of temperature increase $(dT/dt)_{average}$ for all charging and discharging conditions. The relationships between these

values and charge-discharge rate were found to be linear. Results from this experiment are compiled in Table 4.

Table 4 : Results compared from article (x represents discharge rate) [76]

	$(dT/dt)_{average}$	ΔT_{max}	T_{max}
Charging (10C)	1.6 °C/min	4.9 °C	36.0 °C
Discharging (10C)	3.68 °C/min	4.8 °C	30.4 °C
Discharging (all)	y = 0.254x + 0.455	y = 0.365x +1.136	y = 0.268x + 27.704

Another example of using distributed thermocouples to capture thermal gradients is provided by Wiliford et al. in [77]. The authors used 16 K-type thermocouples on a prismatic $LiCoO_2$-4.5 Ah battery with C/3, 1C, 2C, and 4C discharge rates. The battery was suspended in a Plexiglass frame for natural convection cooling. The experiment was performed to provide validation of a thermal model based on electrode entropy changes. The thermocouples locations are shown in Figure 18.

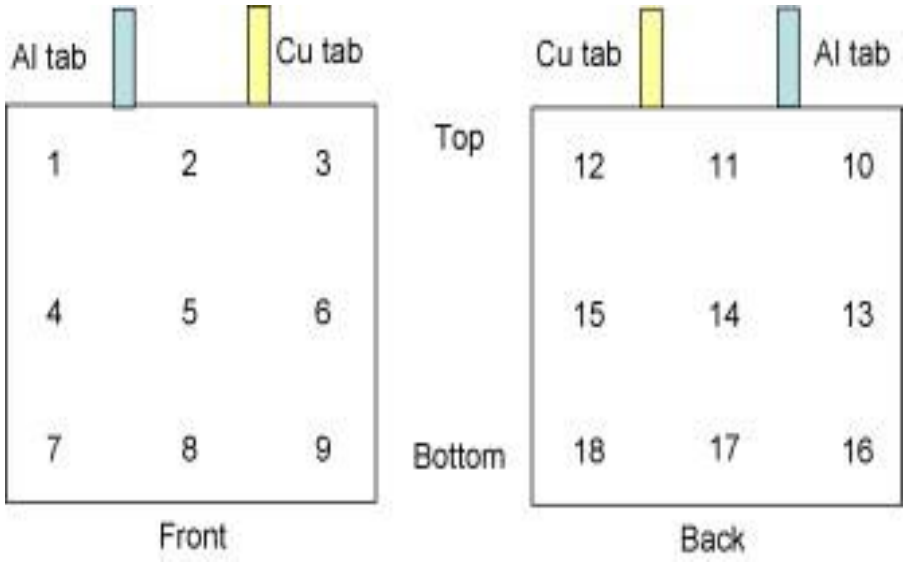

Figure 18: Thermocouple locations on 4.8 Ah prismatic [77]

The surface temperature variation was measured during each discharge. Temperatures around the positive, aluminum tab were found to be consistently higher (about 5 °C) than those at the negative, copper tab. In comparing experimental and model results, the authors only utilize point 14 in Figure 18 in defining the battery temperature. The author used equation (4) for the heat generation rate.

$$\dot{Q} = I^2 R \ - T \, \Delta S \left[\frac{I}{n \, F} \right] \qquad (4)$$

where, I is the current density (A/cm^2), R is the material resistivity (Ω-cm), T is temperature (K), ΔS is entropy change (J/mole K), n equals one electron per reaction, and F is the Faraday constant.

2.11.2 Thermal Measurements via Calorimeter

Another method of heat generation measurement is by calorimeter. There are two methods used to measure the heat generation rates of Li-ion batteries. 1) Accelerated rate calorimeter (ARC), and 2) Isothermal heat conduction calorimeter (IHC), both apply a control volume around the battery and calculate the heat generation rate $\dot{Q}$ [78] by using Equation (5).

$$\dot{Q} = m \, C_p \, \frac{dT}{dt} + h \, A \, (T_{surf} - T_{sink}) \qquad (5)$$

where m is the mass of the battery (kg), C_p is the heat capacity of the battery (J/Kg K), dT/dt is the change in battery temperature with respect to time (V/K), hA is the calorimeter constant (W/K), T_{surf} is the surface temperature of the battery (K), and T_{sink} is the sink temperature surrounding the battery (K).

The ARC method measures the heat generation rate by measuring the temperature rise in battery and heat rejected from the battery to the surrounding according to Equation (5). Hong et al used accelerated rate calorimeter to measure the heat generation rate. He used 1.35Ah Sony 18650 cylindrical battery at 308 K and discharge rates of C/3, C/2, and C/1 with maximum measured heat generation rate of 1.63 (W/L) [79]. Al Hallaj et al did some experiments on 18650 cylindrical batteries and found that the maximum heat generation rate of 0.26 W/L for less than C/10 discharge and charge rate of C/3 [80].

The IHC method uses a large heat sink in contact with battery surface in order to keep the battery at constant temperature (Isothermal) operation during measurements, and therefore eliminates the first term in Equation (5). This method restricted the measurements to low discharge rates, since the fast discharge rates of the battery leads to higher heat generation rates which heat sink cannot extract, resulting in temperature gradient within battery [78]. Kim et al in [81] utilized a

three-cell isothermal micro calorimeter to investigate the dependence of thermal behavior on the charge/discharge rate with $Li_xMn_2O_4$ Coin cells of 2016 size (20 mm diameter and 1.6 mm height). The heat generation rate of the battery was measured using temperature sensors placed between battery and the heat sink and selected discharge rates of C/10, C/5, C/2, and 1C from 300 to 308 K. The corresponding maximum heat generation rates were 0.82 W/L between C/10 and C/5 discharge rate, 0.97 W/L for discharge rate of C/5 to C/2, and 3.21 W/L for discharge rate of C/2 to 1C [81]. Kobayashi et al in [82] measured heat generation rates of Sony 18650 Li-ion batteries using Calvet type conduction micro-calorimeter, which has isothermal aluminium vessel in contact with test battery, and a thermocouple was used to measure the amount of heat transfer from battery to the heat sink. The battery was discharged at 1/50C and 1/10C with an ambient temperature of 300 K, and the measured maximum heat generation rate was 0.97 W/L for discharge rate between C/10 and C/5. Onda et al in [83] used small cylindrical Li-ion batteries to measure the heat generation rate with a thermal bath as an isothermal heat sink. The battery was wrapped in a thin film for an electrical insulation, and using K-type thermocouple the temperature of battery was recorded with discharge rates of C/10, C/2, and 1C. The corresponding heat generation rates were 11.0 W/L, 27.5 W/L, and 84.5 W/L. Bang and Yang in [84] used same equipment as Kim et al in [81] to measure in-situ heat generation rates of coin type $LiMn_2O_4$ Li-ion cell at discharge rates of C/10, C/7, C/3, and 1C with battery temperatures between 330 K and 330 K. The heat generation rates were 0.63 W/L for discharge rates of C/10 to C/5, 2.65 W/L for discharge rates of C/5 to C/2, and 7.51 W/L for discharge rates of C/2 to 1C.

Thomas and Newman In [85], performed isothermal calorimetry on 2325 (23 mm diameter, 25 mm height) size coin cells to provide comparison and validation of a model. The test cell was encased in a copper box packed with copper shot to fill the voids in the calorimeter and decrease the time response of the sensing element within. Heat generation rates were measured as the cell was discharged at C/8, C/3, and 2C rates.

Lv et al. in [86] measured heat generation and temperature response of several 18650 batteries to verify a modeling method. The batteries were initially warmed to 30 °C, then charged and discharged at 1C, 1.5C and 2C. The temperature and temperature response $(dT/dt)_{average}$ was measured. Since the batteries were discharged in an adiabatic condition, the temperature rise

accounts for all the heat generated in the cell. The authors use the energy balance in equation (6), to calculate dT/dt based on over-potential and resistance values generated by the model.

$$\frac{dT}{dt} = \frac{I^2R + I\eta}{c_p m} \tag{6}$$

where I^2R and the $I\eta$ are the heat generated from the total resistance and polarization of the cell respectively, and C_p is the average specific heat capacity of the cell (J/g °C) and m is the total mass of the cell (g), and dT/dt is average temperature rise rate. The results were compared with experimental data and found to be highly consistent, with any small errors accounted for by other processes not evaluated in equation (6). This provides empirical evidence that the greatest effect on heat generation and energy loss for lithium-ion batteries is total resistance and over potential

2.11.3 IR Image (IR Thermography)

As a non-invasive method of temperature measurement, infra-red (IR) thermography is an excellent tool. Within the literature many examples exist of researchers utilizing IR thermography to capture thermal gradients. Several selected works are reviewed.

In the same way that single or multiple thermocouples have been used to validate electro-thermal or chemical models, IR images have been used as well. Keyser and Pesaran in [87], utilize thermal image of Generation-I (4.5 Ah), Generation-II (5 Ah), Generation-III (8 Ah), lithium polymer cells to measure heat generation and temperature distribution. Figure 19 shows the thermal images of Gen-I, Gen-II, and Gen-III cell.

The first and second generation cells showed signs of localized heat during thermal imaging underneath the positive electrode during discharge, whereas the Gen-III cell remained relatively uniform in temperature. As the cell was improved and better electrodes designed, the Gen-III became the most efficient of the cells tested. It exceeded an efficiency of 91% for all currents below 48 amps. In comparison, the Gen-II cell was only 78% efficient at 30 amps. Furthermore, the Gen-III cell showed signs of being slightly endothermic during the initial 2 hours of a C/5 discharge and showed that the heat generation during a C/5 discharge is not constant and highly dependent on SOC of the cell.

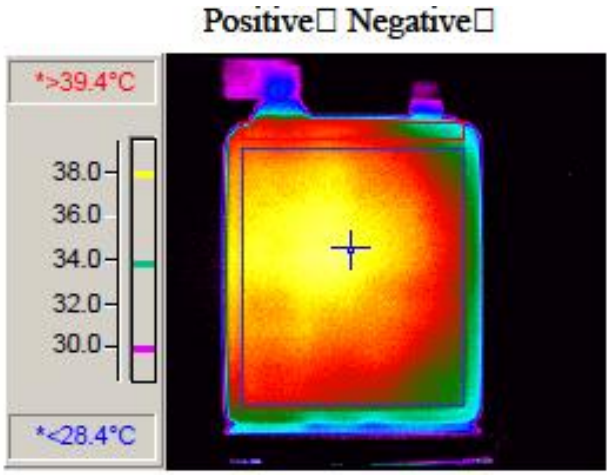

(a) Thermal Image of Gen-I cell after 9 amp discharge

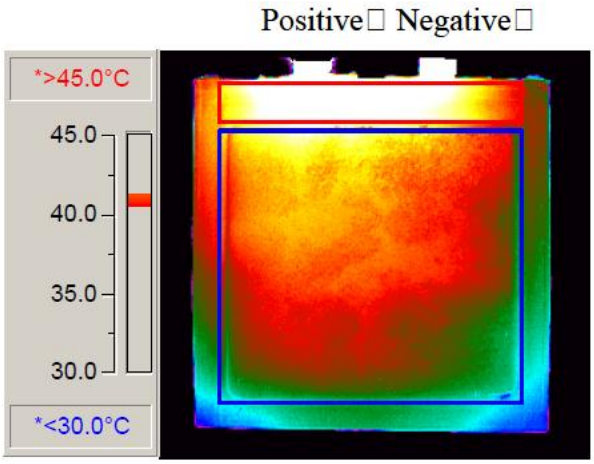

(b) Thermal image of Gen-II cell after 30 amp discharge

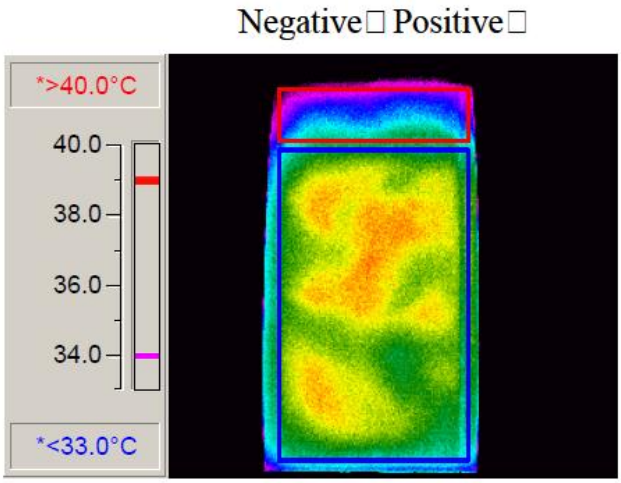

(C) Thermal image of Gen-III cell after 30 amp discharge

Figure 19 : Thermal image of Generation I, II, III cell [87]

In another study, Niculuta and Veje in [88], also utilize IR thermography to measure the surface temperature profile of a discharge of 14A, 35A, and 70 Ah $LiFePO_4$ battery. This enabled visual determination of the spatial temperature distribution, and resulted in validation of a three-dimensional electro-thermal model. Figure 20 shows the compared images and it was found that the maximum surface temperature measured during experiment was 32.1 °C and the model gave a maximum temperature of 33.5 °C.

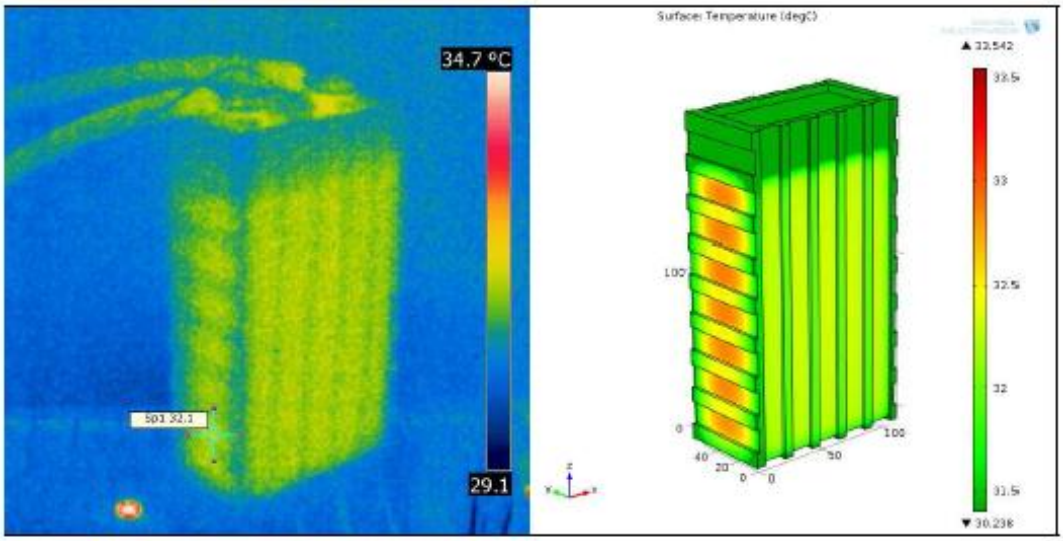

Figure 20 : The battery cell surface temperature distribution after discharging at 14A[88]

The experimental work consisted of placing the cell vertically within an environmental chamber. The door of the chamber was replaced with a plexiglas sheet complete with a viewport for the thermal camera lens. The chamber was set to lab temperature to reduce error associated with lab air infiltrating through the view port. The authors find that with currents of 35A (C/2) or higher used to charge/discharge the cell, the temperature profile is not uniform.

2.12 Heat generation and Thermal runaway

Heat is generated in a battery cell by (1) ohmic heating (or Joule's effect) caused by current transfer across internal resistances and over potential (2) entropy change from electrochemical reactions (i.e., reversible endothermic/exothermic part of reaction). For some electrochemical pairs, another electrical energy loss (and thus heat generation) could result from overcharging a fully charged cell.

The heat generation rate in a cell can be calculated from Eq. (7) [65, 89, 90]

$$\dot{Q} = I\,(E - V) - I\left[T\left(\frac{dE}{dT}\right)\right] \qquad (7)$$

The first term in Eq.1, "*I (E-V)*" is heat generation due to internal resistance (irreversible heat dissipation) and second term "$-I[T(dE/dT)]$ " is known as reversible heat resulting from

changes in open circuit potentials with respect to the temperature at the two electrodes. At practical EV and HEV rates, the second term is usually small compared to the first term. Hence, the heat is generated and released from the cell during both charge and discharge [90]. Thermal runaway can occur if this heat is not removed properly, as elevated temperatures trigger additional heat generating exothermic reactions [16]. These reactions then increase battery temperature further; creating a positive feedback mechanism that causes battery temperature to climb sharply if heat is not dissipated well. As a result thermal runaway can occur that results into complete cell failure accompanied by fire or explosive gas release. Furthermore, even if thermal runaway does not occur, significant degradation of battery capacity can lead by consistently operating at elevated temperature (>50 ^{0}C) [15].

Current collectors create additional Ohmic heating due to the high current densities that occur in planar prismatic type batteries. In another work, Equation (8) was developed to include two added terms that account for heat generated in the current collector tabs [91] .

$$\dot{Q} = I\left(E - V - T\left(\frac{dE}{dT}\right)\right) + A_p R_p I_p^2 + A_n R_n I_n^2 \qquad (8)$$

As heat is generated in the cell during both charge and discharge, the need for adequate cooling arises. The temperature of the cell will continue to increase without adequate processes to remove heat. The heat generation of cell stacks and the collection of stacks into a pack lead to a need for battery pack thermal management. Researchers have examined achieving thermal control with air or liquid systems, insulation, thermal storage (phase-change material), active or passive approaches, or a combination [92].

2.13 Battery Modeling

Determination of battery state is very important in the model-based design and operation of EVs. Good voltage prediction also helps in determination of vehicle range, charge and discharge power capacity, and power train efficiency. During operation, real-time estimation of battery SOC, SOH, and battery temperature are needed in order to manage the battery and optimize its efficiency. Two types of battery model have previously been developed: equivalent circuit models, and electrochemical models.

2.13.1 Equivalent Circuit Modeling

Battery modeling based on differential equations can provide a deep understanding of the physical and chemical process inside the battery and is useful when designing a cell; however, high computational time makes these models impractical for applications that require several model iterations. Therefore, to reach a reasonable economy in computations, battery losses are represented as equivalent electrical circuit components. Equivalent circuit-based modeling is the preferred method of modeling since it does not require an in-depth understanding of electrochemistry of the cell but is still capable of providing useful insight into battery dynamics.

2.13.1.1 R_{int} model:

The R_{int} model is one of the simplest models shown in Figure 21. The model consists with OCV (V_{oc}), and two kind of internal resistance ($R_{discharge}$ and R_{charge}) to account for different resistance values under discharging and charging respectively. These two parameters model all forms of internal resistance including internal ohmic and polarization resistances. The diodes shown imply that during charging and discharging only one resistance ($R_{discharge}$ or R_{charge}) is used. The battery terminal voltage (V_{batt}) is represented as the OCV plus the voltage rise or drop across the resistor. Finally, the R_{int} model can be parameterized directly from experimental data and is very efficient as there is no need to evaluate the differential equations. However, it is unable to give the simulation of transient or time-variant behaviour.

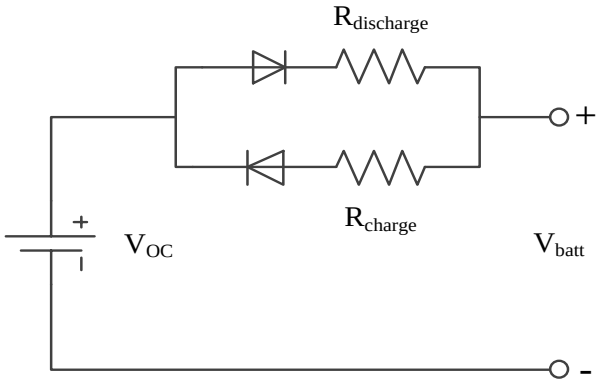

Figure 21 : Schematic diagram of R_{int} model [18]

2.13.1.2 Single RC model:

The single RC circuit model, also known as the Thevenin, first-order RC model or R-RC model is depicted in Figure 22. It improves upon the R_{int} model by adding a resistive-capacitive

element. Total battery resistance is given by a combination of charge transfer (R_{ct}), ohmic (R_{ohm}), and diffusion (C_{diff}) resistances. The capacitive element allows the model to simulate time dependent and transient behaviour.

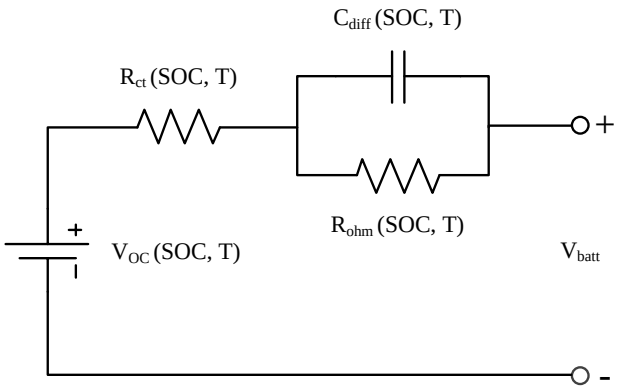

Figure 22 : Equivalent circuit diagram for the single RC battery model [18]

In the R-RC model, it is not easy to determine the resistance and capacitance values directly from experimental data. Instead, parameter estimation methods such as genetic algorithms [93], multi-swarm particle swarm optimization [94], or least squares curve fitting [95] are employed to fit the model to experimental data. Huria et al [96] suggest that this type of model is sufficient for most industrial applications. Hu [94] and He [93] compared many different equivalent circuit models and found that the R-RC model performs well despite its simplicity.

2.13.1.3 Dual RC model:

The dual RC circuit model, shown in Figure 23, is also known as the second-order RC model or dual polarization model which adds a second RC element to the single RC circuit model. The second RC element gives greater resolution of transient behaviour by separating concentration polarization and activation polarization effects [93]. Concentration polarization refers to the voltage drop caused by the formation of concentration gradients within the battery, and activation polarization refers to the voltage drop required to drive a chemical reaction. Parameterizing the dual RC model is similar to the single RC model – the same parameter estimation algorithms can be used, but computational cost is going to be higher due to the additional variables. The dual RC model is more accurate than the single RC model, and both are suitable for system level battery modeling [93] [94] [96]. Higher order RC models are possible,

but are typically not employed because the extra computational cost is not worth the marginal increase in fidelity.

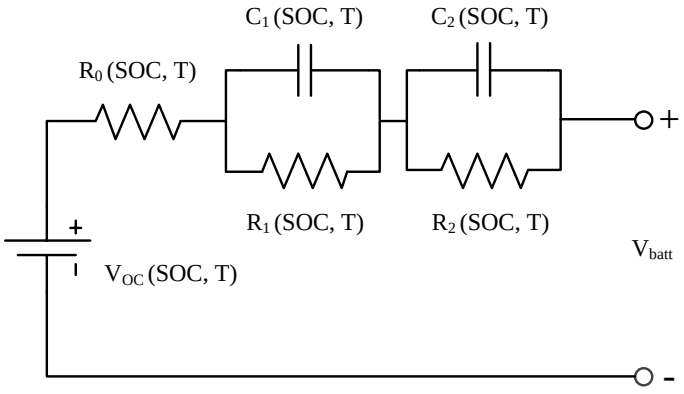

Figure 23 : Equivalent circuit diagram for the dual RC battery model [18]

To model either the short or long term behavior of battery cells many different types of models can be developed, each with its own advantages and disadvantages. Depending on the application and specifications, a choice between the models can be made. As this research is going to be conducted from the point of view of a mechanical engineer, the battery is seen as a part of a larger electrical-mechanical system and the resulting short and long term behavior of the battery cells is of more interest rather than which electrochemical processes caused the behavior. An equivalent circuit-based model is therefore desirable since it is fast and does not need deep understanding of the phenomena inside the battery and also the outputs of the model can be directly connected to the rest of the system.

2.13.2 Battery Thermal Modeling

The topic of thermal modeling of Li-ion batteries is a research area that has experienced steady growth in interest. Early research focused on defining a model of a single electrode pair comprising a single battery cell. Later efforts expanded modeling to include multi-cell stacks, module, and battery packs. This section is thus organized into two sections: 1) Single cell modelling and 2) Module and Pack modelling

2.13.2.1 Single Cell Modeling

Pal and Newman, in [65] developed a 1D lumped thermal model for the single cell sandwich. The model was a modification of the 1D model presented by Fuller and Doyle. Newman added

an energy balance to the model using equation (9). Model parameters were input to represent a cell utilizing Li|PEO_{15} – $LiCF_3SO_3$|TiS_2 electrode pair.

$$\dot{Q} = I\left(V_{oc} - V - T\frac{\partial V_{oc}}{\partial T}\right) = h_{conv}(T - T_{\infty}) + m_c c_p \frac{dT}{dt} \qquad (9)$$

where, Q is the heat generation rate (W), I is current (A), V is voltage (V), m_c is the mass of cell (kg), c_p is the average heat capacity (W/kg K), h_{conv} is the convective heat transfer coefficient (W/m^2 K), T is temperature (K), and T_{∞} is ambient temperature (K). The left side of the energy balance equation represents the heat generation terms and is equivalent to equation (7). Convective cooling heat removals on the right as well as sensible heat stored in the battery are accounted for as the battery temperature rises. Several simulations were performed with two boundary conditions to investigate the performance of Li-ion cells: isothermal and adiabatic. In isothermal simulations, all heat generated in the cell is assumed to be transferred out of the system as it is generated. As such, the temperature of the cell is fixed. It was observed that, as temperature of operation increases, the cell potential is higher at each utilization point. In addition, the heat generation rate increases as the temperature of operation decreases. This is due to decreased electrical conductivity at lower temperatures, resulting in higher Ohmic heat generation. In adiabatic simulations all heat generated in the cell is assumed to remain in the cell as sensible heat. This results in a rising temperature as the battery is discharged. In general it was observed that, as the discharge rate increased, the cell temperature was higher at each utilization point. Also, heat generation rate increased due to increased discharge rates.

Kim et al [73] developed a 3D model for Li-ion cells by dividing the battery into three subdomains: particle domain, electrode domain, and cell domain. The particle domain deals with solid-phase particles in the positive and negative electrodes and concerns the diffusion inside the particles as well as the reaction at the particle surface. The electrode domain includes diffusion and current flow in the electrodes and electrolyte. Finally, the cell domain is utilized for the electrical and thermal behaviour calculations of the battery. The current and temperature distributions over the cell are calculated in this domain. Three domains are decoupled and solved separately in this method, but the physics between them is still coupled by the inter-domain information exchange. This model, however, requires a lot of computational effort, which prevents it from being employed to study the battery module or packs.

Finally, Gerver and Meyers, in [97] presented a 3D electrochemical battery thermal model simulating coupled thermal and electrochemical phenomena in Li-ion batteries simultaneously. They modeled the current collector via a number of electrochemical resistors. The electrochemical resistors were also nonlinear curve fittings to the 1D electrochemical models derived from the basic electrochemical equations of the battery. Combining the electrochemical resistors and 2D resistor networks and solving the subsequent equations determined the battery variables in three dimensions. A visual schematic of the model structure is displayed in Figure 24 (A), with current collector sheets showing 16 nodes, and defined locations for current flow in and out of the cell.

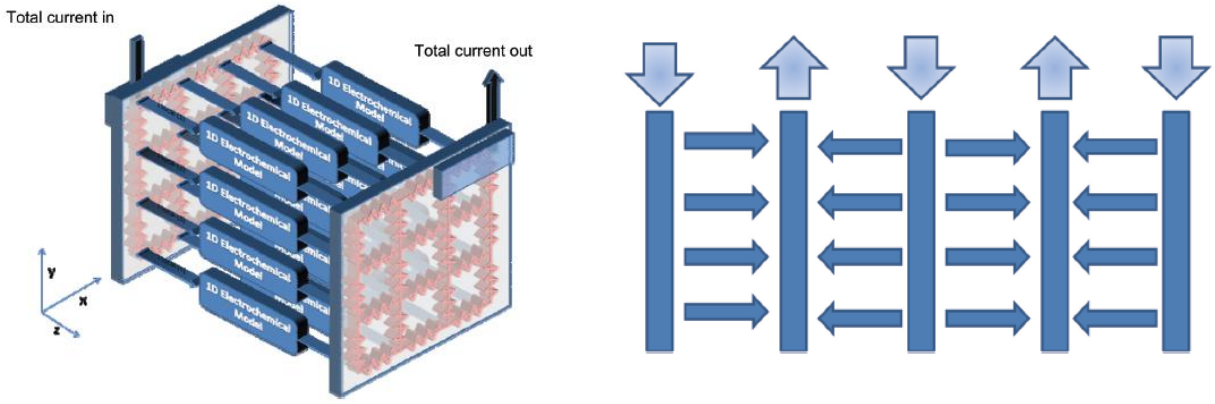

(A) Schematic of model structure **(B) Diagram of current flow**

Figure 24 : Schematic of model structure and diagram of current flow [97]

They also connected all cells and solved the entire system simultaneously to address the current distribution between cells. In the model, since the cells are parallel, the current which enters a current collector can go into either the cell on the left or the right (Figure 24-B). The reported results showed that the current of the cells in the middle of the stack increases with time, while for the outer cells the current drastically decreases.

Electrochemical heat generation is determined from equation (7) as in previous models. Resistive heating in the 2-D current collectors is calculated via the finite-difference equation shown as equation (10).

$$\dot{Q} = 0.5\left[\frac{\left(V_{x,y} - V_{x-1,y}\right)^2}{R_{x-\frac{1}{2},y}} + \frac{\left(V_{x,y} - V_{x+1,y}\right)^2}{R_{x+\frac{1}{2},y}} + \frac{\left(V_{x,y} - V_{x,y-1}\right)^2}{R_{x,y-\frac{1}{2}}} + \frac{\left(V_{x,y} - V_{x,y-1}\right)^2}{R_{x,y+\frac{1}{2}}}\right] \quad (10)$$

where $V_{x,y}$ is the voltage on the current collector in the center of the node (x, y) and R is the local current collector resistance, which varies based on local temperature. Heat transfer between nodes of the model is based on the standard heat conduction equation shown as (11).

$$\rho C_p \frac{\partial T}{\partial t} = k_x \frac{\partial^2 T}{\partial x^2} + k_y \frac{\partial^2 T}{\partial y^2} + k_z \frac{\partial^2 T}{\partial z^2} \quad (11)$$

where k is the thermal conductivity, T is the temperature, t is time, ρ is density and Cp is heat capacity. The x and y direction are in the plane of the current collector and the z direction is between cells in a stack. The output of the model is transient current and temperature distributions. They obtained 5 simulations with different thermal boundary conditions. The output of the model is transient current and temperature distributions. In general it was found that cooling the battery closer to the areas of highest heat generation leads to greater uniformity in both current and temperature distribution.

In [74], Ye et al. produced an electro-thermal model of $LiMn_2O_4/LiC_6$ by coupling electronic conduction, mass transfer, energy balances and electrochemical mechanisms. The model is used to determine lithium ion diffusivity and chemical reaction rates at different operating temperatures. These rates are established to explain the decrease in capacity and power experienced during low temperature operation.

In general it is found that cooling the battery closer to the areas of highest heat generation leads to greater uniformity in both current and temperature distribution.

2.13.2.2 Pack and Module Modeling

Pack modeling is important because it explains the combined effect of the many small heat generating elements within. By investigating the collection of batteries in various arrangements and with various thermal control and cooling methods, researchers can generate solutions that increase the commercial value of lithium ion battery packs. Pack dynamics directly affect vehicle range and economic lifetime of electric vehicles [92].

Pesaran et al. in [92] presented a fundamental heat transfer model for a pack. The model assumes that, as heat is generated in a module, it is either removed/rejected to the surrounding area, accumulated in the module, or both. The overall energy balance for a battery module is defined in equation (12).

$$\dot{q} - h_b A_{bs}(T_{bs} - T_f) - \sigma \varepsilon F_{bf} A_{bs}(T_{bs}^4 - T_f^4) = M_b C_b \left(\frac{dT_{ba}}{dt}\right) \qquad (12)$$

where $\dot{q}$ is the heat generation rate in module (W), h_b is the heat transfer coefficient between battery surface and its surrounding fluid (W/m^2 K), A_{bs} is the battery surface area exposed to the surrounding fluid (m^2), T_{bs} is the battery surface temperature (K), T_f is the surrounding fluid temperature (K), σ is Stephen-Boltzman constant, ε is the battery surface emissivity, F_{bf} is the shape factor between the battery and its surroundings, M_b is module mass (kg), C_b is weighted-average module heat capacity (J/kg K), dT_{ba} is average module temperature (K), and t is time (s). This model assumes an average temperature for each battery, and ignores the three-dimensional temperature distribution within each battery. The overall energy balance can be used to obtain the temperature distribution in a pack of modules. For example, if a certain amount of a fluid is passed around a module, the fluid temperature change can be obtained from overall energy balance for the module:

$$h_b A_{bs}(T_{bs} - T_f) = \dot{m}_f \, C_f (T_{out} - T_{in})_{module} \qquad (13)$$

Note that T_f is the average fluid temperature, $\dot{m}_f$ is the mass flow rate of fluid around each module, C_f is the fluid specific heat, T_{in} is the incoming fluid temperature to the module, and T_{out} is the temperature of fluid leaving the module. The overall temperature change in the fluid can be obtained from the overall energy balance in (14):

$$N\left(\dot{q} - M_b c_b \frac{dT_{ba}}{dt}\right) = \left[\dot{m}_f C_f (T_{out} - T_{in}) - \dot{M}_f C_f \left(\frac{dT_f}{dt}\right)\right]_{pack} \qquad (14)$$

where N in (14) is the number of modules in the path of $\dot{m}_f$ and $\dot{M}_f$ is mass of the fluid. The authors analyze a hypothetical battery pack consisting of 30 sealed prismatic batteries with a cooling coefficient applied to the surfaces of each battery. By assuming symmetry in the

horizontal plane the model is solved in 2D using an iterative process. The energy balance between the battery surface temperature and its surroundings was used to find the temperature change of the fluid, while temperature distribution in any single battery was determined via superposition principle.

An air flow of 0.08 kg/s enters the pack at one end and splits into three paths to cool a series of 10 battery modules in each path. The air gap is set such that the heat transfer coefficient is about 35 [W/mK]. Figure 25 shows the resulting variation of air temperature, battery surface temperature, and battery centerline temperature along the length of the path in the flow direction at steady state. The air temperature rises by 1.3 °C as it passes by each module, resulting in a variation of 13 °C between the inlet and the outlet [92].

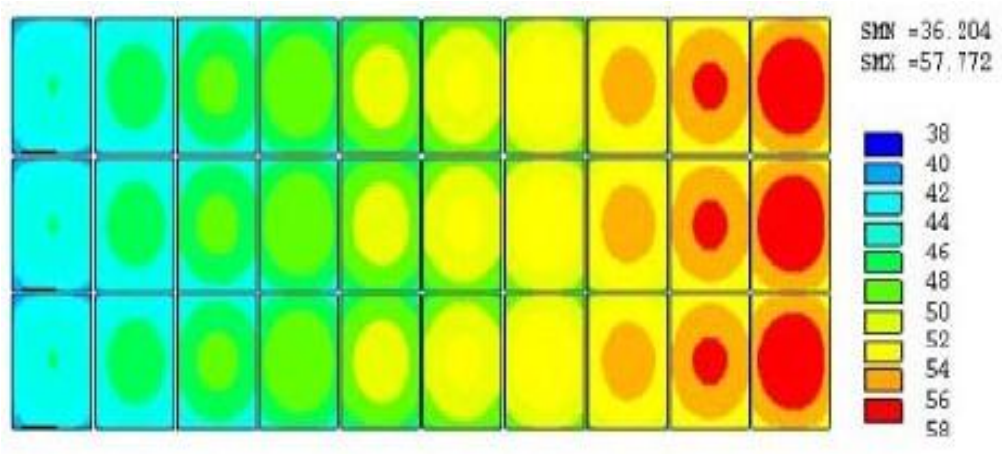

Figure 25 : Steady-state 2-D temperature distribution in battery pack cooled by an air flow (W) [92]

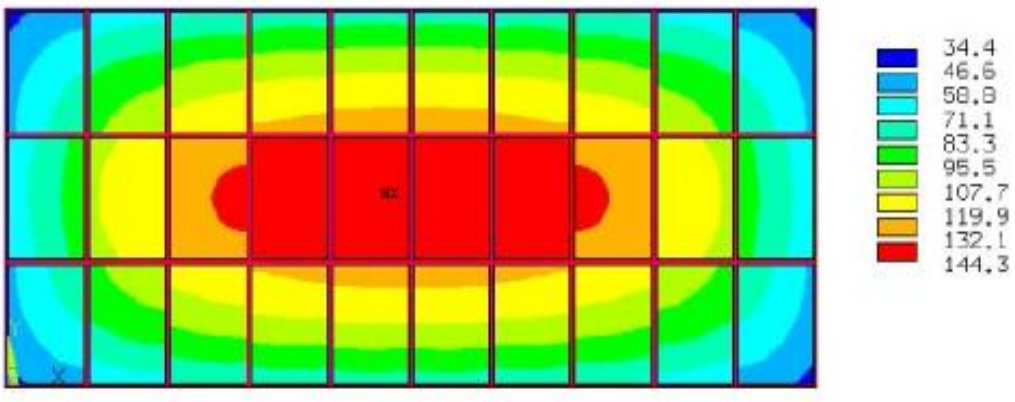

Figure 26 : Steady-state 2-D temperature distribution in an enclosed battery pack [92]

There is also a variation of about 4.5 °C within each battery module. Although this cooling arrangement is not ideal, it is comparatively better than placing the pack in a closed box, as shown in Figure 26.

Wu et al. in [66], developed a coupled thermal-electrochemical model to analyze the effect of heat generation from cell level to pack level in a $LiCoO_2$ based cell. Interconnection resistances for both series and parallel connected battery packs are compared. Each cell is described by a coupled thermal and electrochemical model. The electrochemical model is based on ion diffusion and the Butler-Volmer equation. The thermal model incorporates Ohmic heat due to internal contact resistances (q_c), heat from the reaction current and over potentials (q_r), and ionic Ohmic heat from the motion of Li-ions through the solid and electrolyte phase (q_j). These terms are defined in equations (15), (16), and (17).

$$q_c = I^2 \frac{R_c}{A} \tag{15}$$

$$q_r = A \int_x^{x+dx} j^{Li}(\emptyset_s - \emptyset_e - U)\, dx \tag{16}$$

$$q_j = A \int_x^{x+dx} \left[\sigma^{eff} \left(\frac{\partial \emptyset_s}{\partial x}\right)^2 + k^{eff} \left(\frac{\partial \emptyset_e}{\partial x}\right)^2 + k_D^{eff} \left(\frac{\partial \ln c_e}{\partial x}\right)\left(\frac{\partial \emptyset_e}{\partial x}\right)\right] dx \tag{17}$$

where A is the plane area of the electrode parallel to current collector (cm^2), x is the Cartesian coordinate inside singe anode/separator/cathode layer in the direction perpendicular to the separator (cm), j^{Li} is the reaction current density (A/cm^2), $\emptyset_s$ and $\emptyset_e$ are the potential of solid electrode phase and electrolyte phase, an U is thermodynamics OCV, σ^{eff} is conductivity of active materials in the electrodes (S/cm), k^{eff} is effective conductivity of the electrolyte (S/cm), k_D^{eff} is the effective diffusional conductivity of a species (A/cm). The lithium concentration and charge distribution in the electrolyte and solid phases are coupled through Butler-Volmer equation (18)

$$j^{Li} = a_s i_o \left\{\exp\left[\frac{\propto_a F}{R\,T}\,\eta\right] - \exp\left[\frac{\propto_c F}{R\,T}\,\eta\right]\right\} \tag{18}$$

Where a_s is the active surface area per electrode unit volume for electron transfer reactions (1/cm), $\propto_a$ is transfer coefficient of anode, F is the Faraday's constant (C/mol), R is the

universal gas constant (J/mol K), T is the temperature (K), η is the over potential (V), and $\propto_c$ is the transfer coefficient of the cathode. The lumped unsteady heat transfer equation in (19) was used to account for sources of heat. Convective cooling and sensible heat are included with the three heat source terms. Heat generated by entropy changes in the reaction is considered negligible and is ignored.

$$\rho c_p \frac{\partial T}{\partial t} = q_r + q_j + q_c - hA_{surf}(T - T_{amb}) \quad (19)$$

Isothermal 1C discharges were simulated for a 6 Ah cell to test the effect of temperature on lithium ion battery performance. It was observed that battery performance improves with increased temperature. As the temperature increases, useable capacity and output energy increase as well. This is due to faster diffusion of lithium through the faster solid phase and to the fact that the system is less hindered by lithiation limits. The performance of the battery is thus improved, as the solid state diffusion is often the rate determining step [66].

2.14 Degradation mechanisms of Li-ion cells

It is important to study the various types of degradation mechanisms of Li-ion cells because the heat generation from cell/module/pack is directly related to the degradation and life of the battery. Li-ion cells undergo degradation in terms of capacity and power capability during usage and storage. The degradation of cell occurs much faster during cycling than storage under the same conditions. The normal and accelerated degradation mechanisms for cycling and storage are described in the following subsections.

2.14.1 Degradation of Li-ion cell due to storage

During storage, the active anode material is exposed to the electrolyte through the porous Solid Electrolyte Interphase (SEI) layer, and side reactions enhance this SEI layer. High temperatures or high SOCs result in more severe capacity fading as well as resistance growth (power fading) in the cell. Therefore, to improve battery life and to slow down the electrochemical processes, Li-ion cells should be stored with less than 100% SOC and around 15°C (optimal conditions 40% SOC and 15°C) [98]. This will allow Li-ion cell last many times longer than one stored at 100% charge, particularly at high temperature.

2.14.2 Normal Degradation of Li-ion cell due to cycling

Capacity fade primarily occurs on the electrode/electrolyte interphase under influence of intercalation and deintercalation of lithium ions. Ideally, loss of lithium ions and active materials are the only mechanisms that degrade a Li-ion cell. But, in practice, other degradation mechanisms accelerate the capacity fading. Power fade is also coupled to capacity fading. The growth of the SEI layer results in the internal impedance rise of the battery cell and the deformation of the electrodes in a lower conductivity. As a result, due to the loss of active material the power fading occurs. Capacity fading can be divided into four stages as shown in Figure 27.

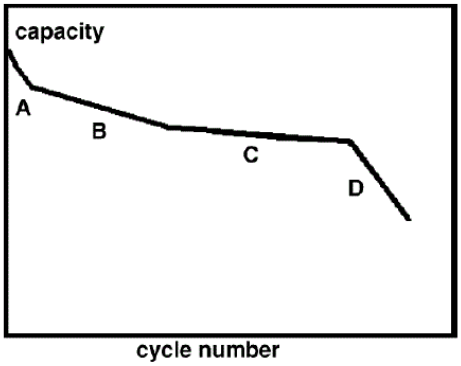

Figure 27 : The general shape for capacity versus cycle number [99]

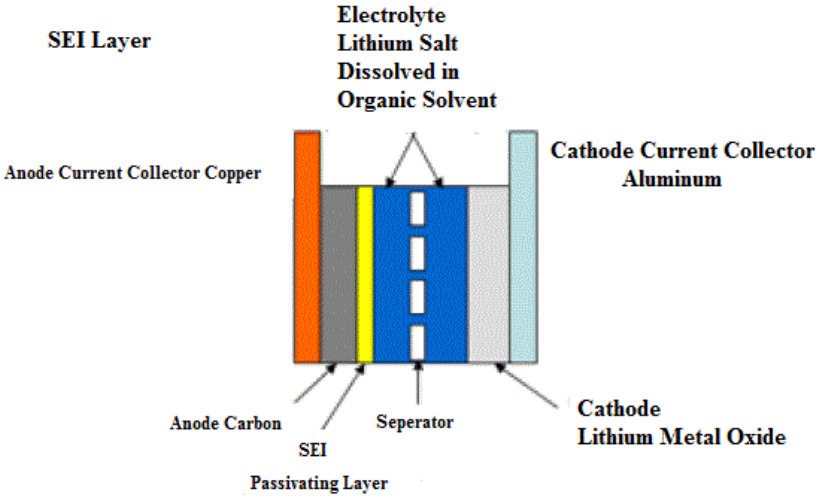

Figure 28 : Schematic of SEI film layer in Li-ion battery [100]

Stage-A: During stage “A”, on the interphase of the anode with the electrolyte of the separator a SEI film will form as a side reaction; due to this there is a fast decrease in capacity. This stage

does not last for many cycles because as the cell is cycled more, the side reaction rate will gradually decay [101]. A schematic of a SEI film layer in Li-ion cell is given in Figure 28**.**

Stage-B: In the stage B, anode is the limiting electrode [101]. Because of SEI film layer formed on the anode, less active material is available and less lithium ions are intercalated into the anode during charging. As a result the loss rate of lithium ions will be slower, and the SEI layer protects the anode from reduction reactions with the electrolyte. During continuous intercalation and deintercalation the SEI layer cracks and more active material will be exposed. This will cause more side reactions and the SEI layer will continue to grow, leading to a less porous SEI layer and loss of lithium ions.

Stage-C: In stage C, the degradation rate of the active cathode material is higher than the loss of lithium ions. On the cathode/electrolyte interphase layer similar to the SEI layer is formed, which is named the Solid Permeable Interphase (SPI) [102]. Due to cycling, this layer will also grow and limit the active cathode material. The anode is however still the limiting electrode in this stage, as there is still more active cathode material available than lithium ions.

Stage-D: In stage D, the cathode becomes the limiting electrode due to the high degradation rate of the cathode. Less active cathode material is available than the amount of 'cycle able' lithium ions [101]. Not all the lithium ions that were intercalated into the anode during charging can be intercalated into the cathode during discharge. Hence, more and more lithium ions are stuck inside the anode. The cathode will be fully intercalated during discharge, which raises the active cathode material loss rate. These added effects cause an accelerated capacity fading and the capacity will rapidly decrease.

The severity of these stages is not the same for different types of Li-ion cells. For example, for $LiFePO_4$, the main capacity fading mechanism of cells is the loss of lithium ions by the lithium ion consuming SEI film later formation, which also results in a loss of active anode material [103]. Loss of cathode material happens at a lower rate for $LiFePO_4$ cells, since neither cycling nor temperature change enhances the formation of the SPI layer [102]. This causes $LiFePO_4$ cells to have a much higher cycling life compared to other chemistries.

2.14.3 Accelerated degradation of Li-ion cell due to cycling

In real life applications Li-ion cells experience accelerated degradation due to certain stress factors. Stress factors such as deep DODs, elevated C-rates, high or low temperatures, and operating at high SOCs can have negative impact on the cell capacity and cause accelerated degradation. These stress factors are described in following subsections.

2.14.3.1 Depth of discharge (DOD)

The cycle life of a cell strongly depends on the DOD. Figure 29 shows cycle life versus DOD curve for different battery cell chemistries. The more intercalation and deintercalation takes place in the electrodes due to deeper discharge. The loss of lithium ions and active electrode material is higher for larger DOD cycles. At high DODs, additional degradation mechanisms can occur resulting in decomposition and dissolution of cathode material and capacity fading [104]. DOD has no influence on the capacity fading of $LiFePO_4$ cells, but the charge or energy processed is the determining factor [105].

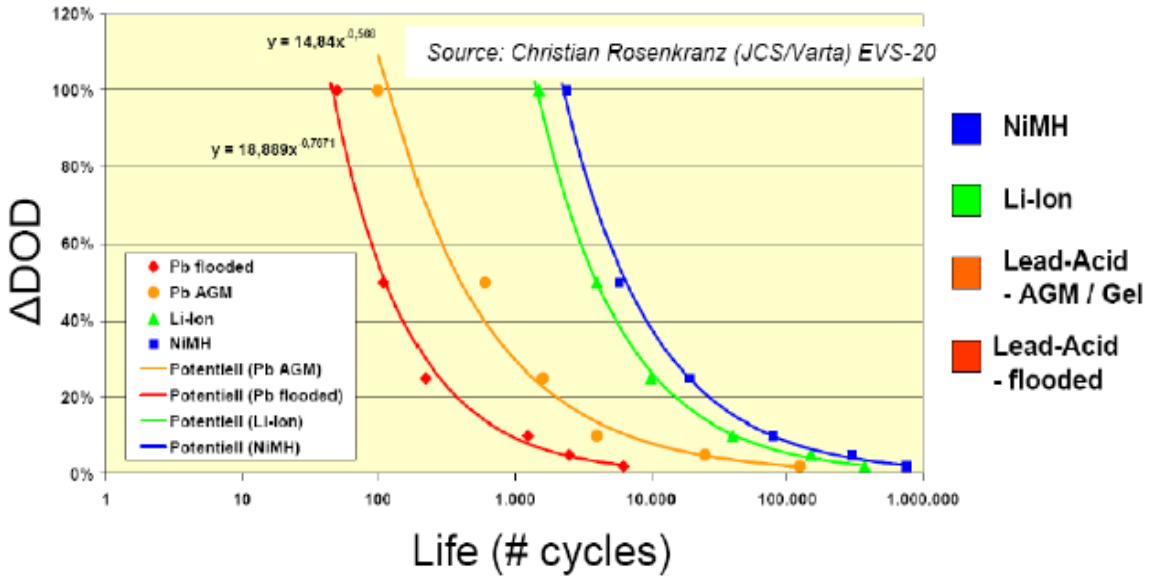

Figure 29 : Cycle life vs. ΔDOD curve for different battery cell [106]

2.14.3.2 Elevated C-rate Effect

High C-rates generate more heat and cause the temperature of the cell to rise invoking the high temperature degradation mechanisms. High currents also cause local over potential of the electrodes earlier stage at certain areas of the cell. High C-rates will also cause the SEI layer on

the anode to crack faster. More active anode material is exposed and the SEI layer will restore itself, reducing lithium ions from the battery cell process. High C-rates will furthermore cause additional strain on the electrode materials, resulting in increased deformation and loss of active material [104]. These effects will result in power fading and capacity fading.

2.14.3.3 Temperature Effect

The discharge capacity of Li-ion cells is strongly influenced by temperature. Li-ion cells have an optimal temperature operating range and outside this range the battery cell undergoes severe loss of capacity. High and low temperatures have different effect on the battery life. In Figure 30 an example of the temperature range for optimal life cycle is shown. It can be seen that the decay of cycle life is different for high and low temperatures, as different degradation mechanisms deteriorate the battery.

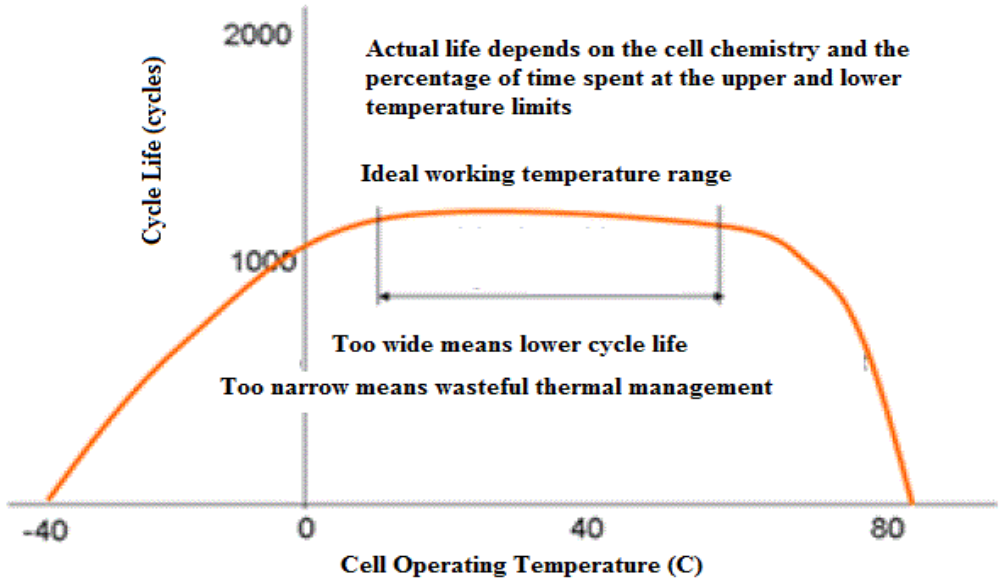

Figure 30 : An example of a battery cell's temperature range for optimal cycle life [107]

At **low temperature**, due to the higher activation energy needed for the chemical reactions and lower ion diffusion; there will be a loss of capacity and deliverable power. However, when the temperature is restored to nominal level, the capacity and power capabilities will be recovered. Under normal discharge, low temperature on its own does not have any permanent influence on capacity fading, but during charging, lithium plating is likely to happen because the intercalation rate at the anode is inherently slower than the deintercalation rate [108].

In the long term operating at **high temperature** can cause severe damages to the cell. As shown in Figure 31 increasing temperatures results in higher capacity fading. Due to high temperatures the SEI layer will slowly break down and dissolve into the electrolyte. The active material of the anode will be partly exposed to the electrolyte again, causing the side reactions. The damaged SEI layer will be restored due to the side reactions or a precipitation of the dissolved SEI particles will take place. Also parts of the cathode can dissolve into the electrolyte and incorporated into the SEI layer. As a result the intercalation at the anode will be more difficult and the ionic conductivity will be lowered. The same degradation mechanism happens at the cathode side with the SPI layer. Another degradation mechanism is the deformation of the anode and cathode.

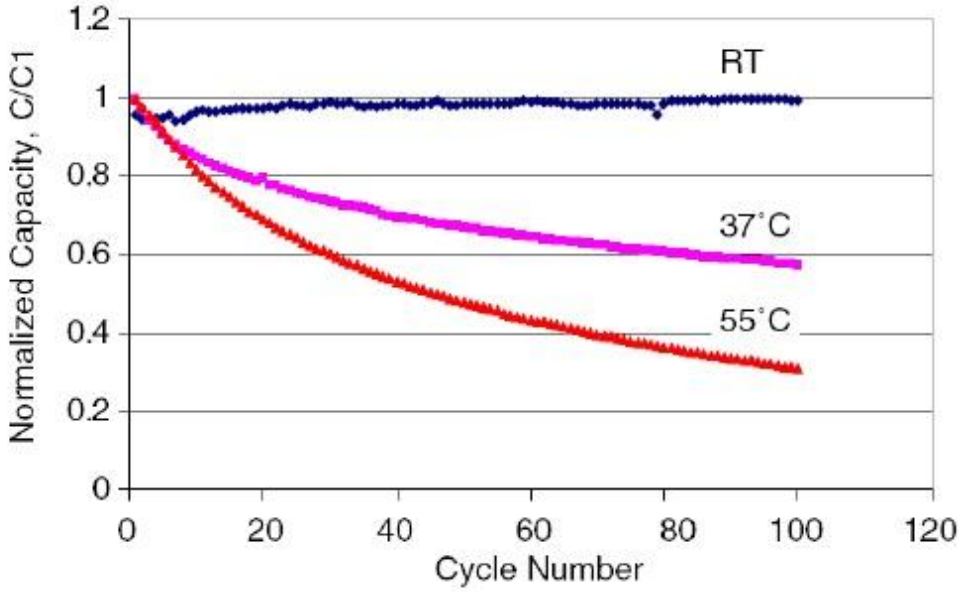

Figure 31 : The accelerated capacity fading due to high temperatures [109]

2.14.3.4 State of charge

At higher SOC battery cell is more reactive, which will accelerate degradation of the cell. At high SOC the anode will be highly energized and self-discharge will also be higher and the SEI layer will grow faster. Furthermore, electrolyte oxidation occurs at high SOC, leading to impedance increase [110]. These effects result in capacity and power fading. During storage for a long time, a high SOC will have a more profound effect. In case of overcharge or over discharge, other degradation mechanisms come into play as follows:

2.14.3.5 Overcharge

When the cell is charged over the specified voltage, a small increase in capacity is initially obtained, but the cycle life is strongly reduced. This effect is stronger as the end of charge voltage increases. During overcharge electrical energy is pumped into the battery, but more intercalation can hardly take place. This will be represented by a sharp increase of internal resistance and the temperature [111]. Decomposition of the binder and electrolyte, forming insoluble products, blocking the pores of the electrodes, and causing gas generation subsequently may take [112].

2.14.3.6 Over discharge

When the cell is discharged under the specified cut-off voltage, two degradation mechanisms severely damage the cell. 1- Corrosion of the copper current collectors and dissolution into the electrolyte resulting in loss of contact with anode and power fade [113]. 2- Decomposition of the SEI layer on the anode. The high anode potential will cause dissolution of the SEI layer. Upon recharge the exposed active material will cause side reactions to restore the SEI layer and reducing lithium ions, causing capacity fading [114].

Chapter 3

Part-I: Heat Generation and Cooling

3.1 Design of Hybrid Test Stand for Thermal Management

In 2008, a hybrid test stand was designed and built at the University of Waterloo to perform component degradation studies and to enable scaled Component-In-The-Loop (CIL) testing [115]. Due to cost and safety implications the system was designed at $1/50^{th}$ scale of the full powertrain to allow for the testing of smaller fuel cells and single cell batteries. A hybrid test stand is modified for this work. The hybrid test stand was modified so that fuel cell components were not connected to the power bus. This enabled the test stand to behave in full EV mode, where only batteries are charged and discharged using the electrical distribution grid of the lab. Figure 32 shows a schematic representation while Figure 33 shows picture of the modified hybrid test stand for thermal management.

To allow for significant flexibility, high and low voltage supplies and loads were integrated. The low-voltage supply and load were Lambda ZUP20-40-800 and TDI Dynaload RBL232 50-150-800 respectively. TDI Load box, Lambda power supply and all other necessary components are shown in Figure 33. The system was designed in order to allow for battery only, fuel cell only, and hybrid testing. From the main bus, DC/DC and fuel cell are removed during battery testing.

The voltage, current and temperature of the cell are monitored by the MotoTron controller (CTRLPCM00200) which is shown in Figure 33. The MotoTron controller interfaces via RS232 communication to the test stand computer-1. The test stand computer-1 manages Lab-view program (measurements of battery voltage, current, charge-discharge cycle, cycle number, and time) which record values at one second intervals and test stand computer-2 manages the Keithley-2700 (Data Acquisition) program (measurements of battery surface temperature, heat flux, and water inlet and outlet temperature for top and bottom cold plates).

There are two E-stop (Emergency shutdown) buttons in the test stand. One is near MotoTron controller and another one is near cell housing and can be easily seen in Figure 33 and Figure 34. The E-stop circuit controls the 12V supply to the normally-open contactors, thereby acting in series with the MotoTron control circuit that usually controls the ground path of the contractor control circuit. The E-stop circuit was integrated that caused an immediate opening of the contactors on the power lines in the event that one of two E-stop buttons was hit.

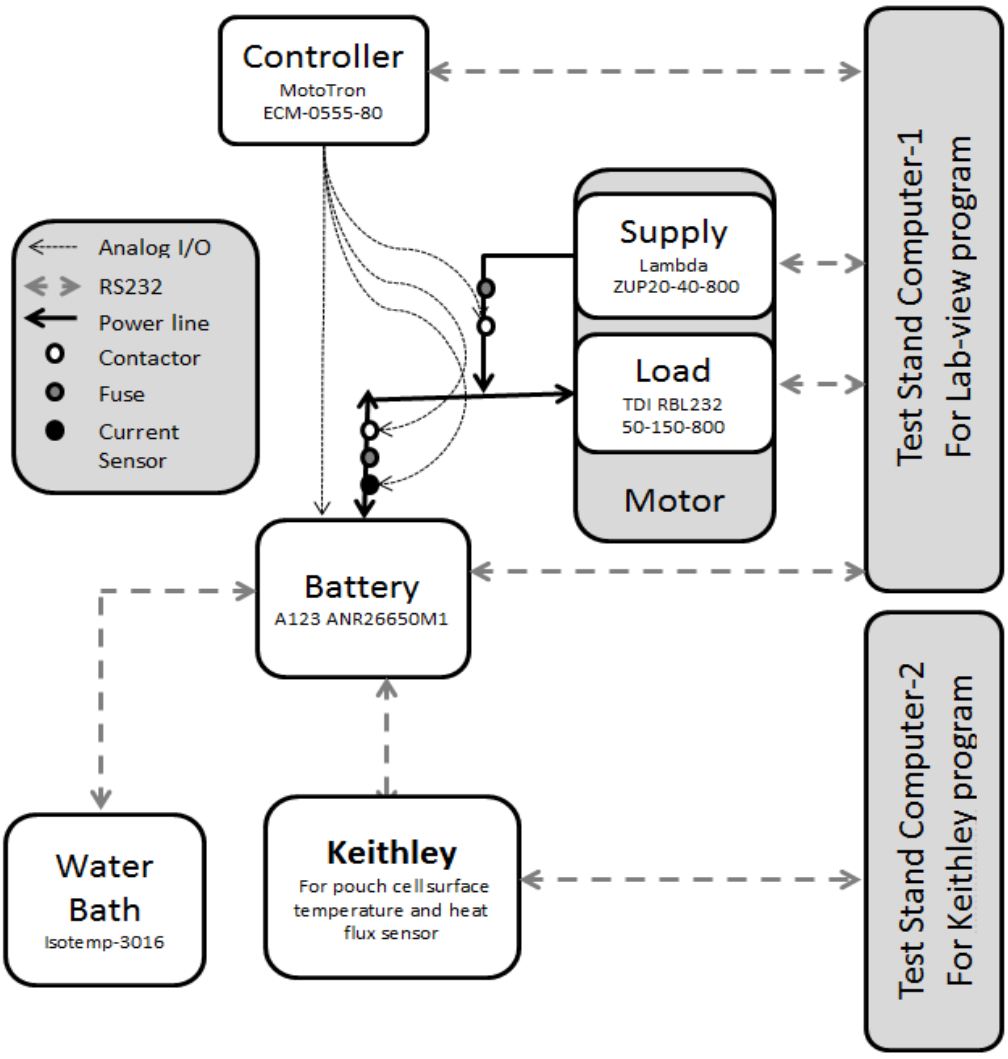

Figure 32 : Schematic representation of modified hybrid test stand for thermal management

Three thermocouples were connected to the MotoTron controller allowing one thermocouple per cell in the original hybrid test stand design. These thermocouples were repurposed to measure

lab temperature, as the thermal data collection system was implemented to record and monitor battery temperatures.

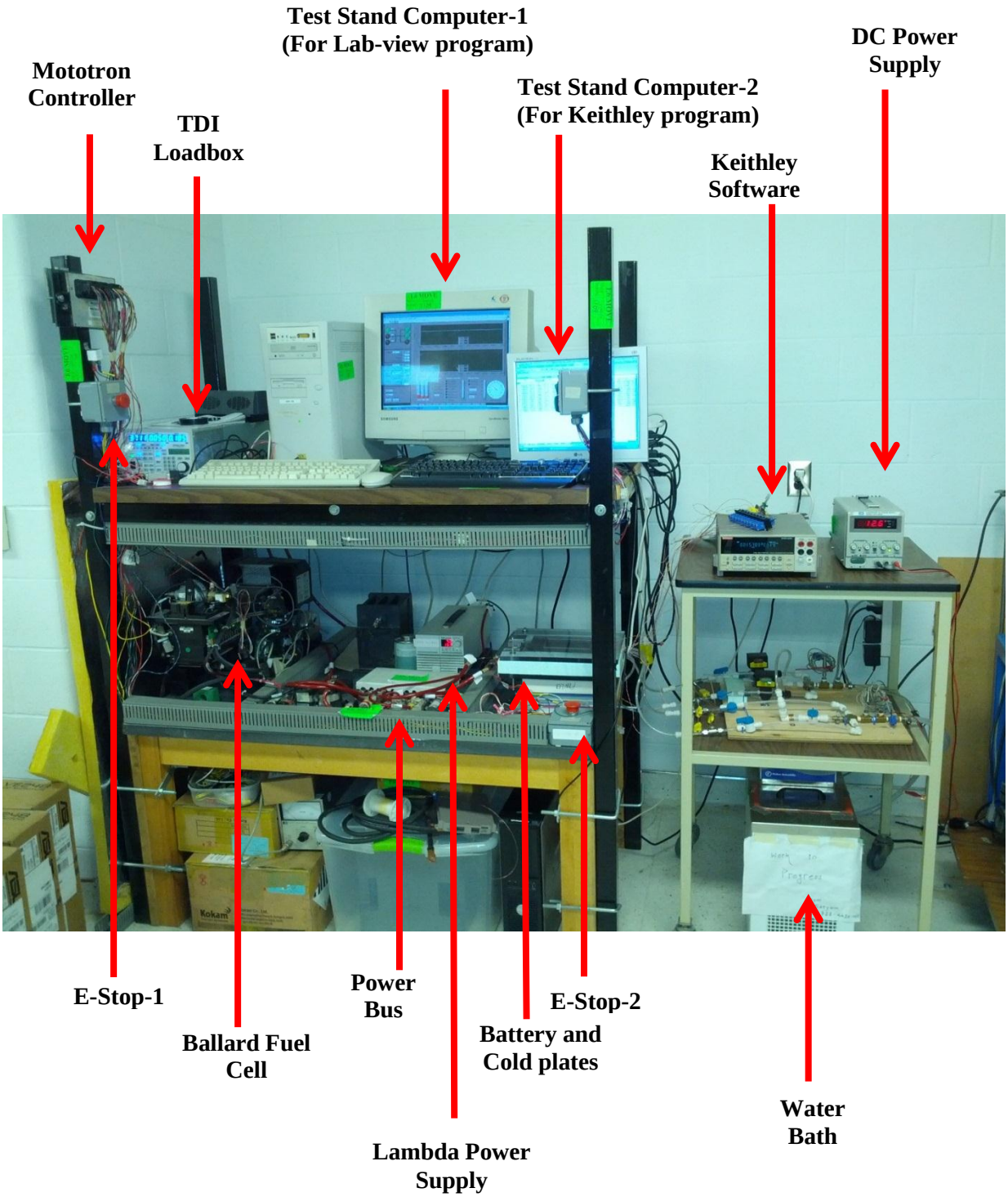

Figure 33 : Picture of modified hybrid test bench for thermal management

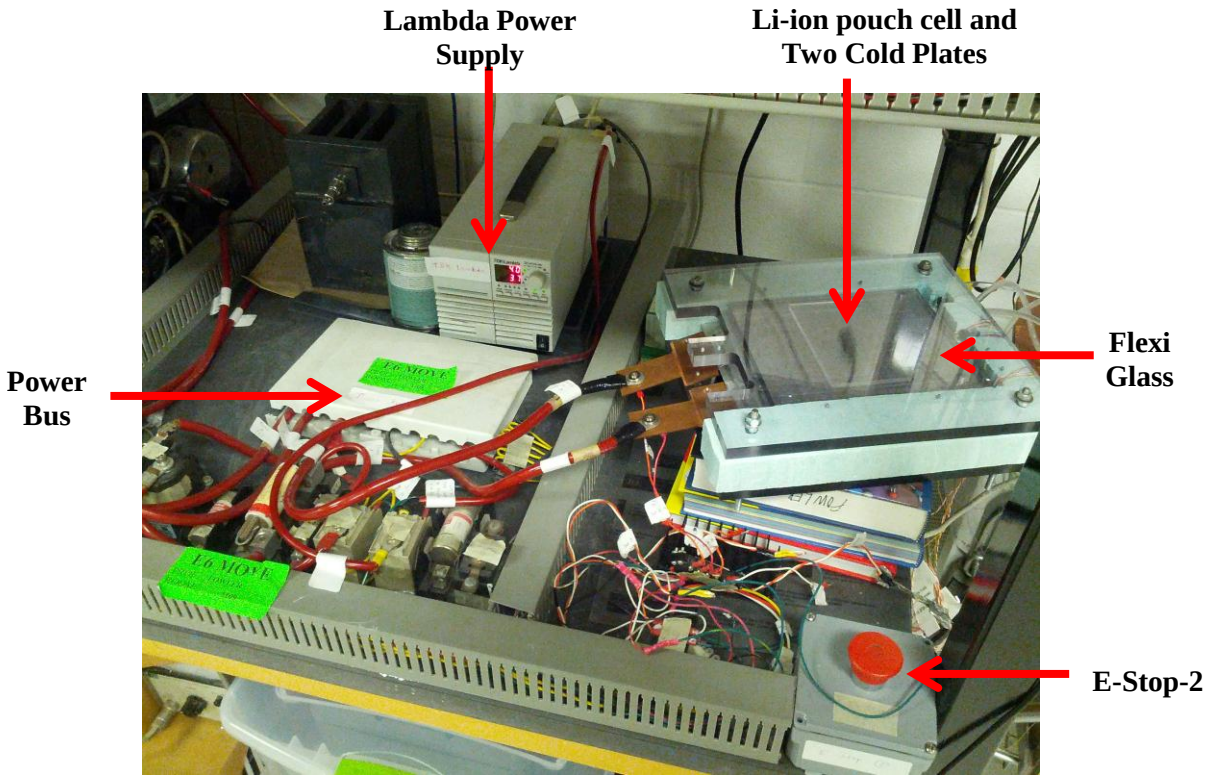

Figure 34 : Pouch cell and two cold plates set-up

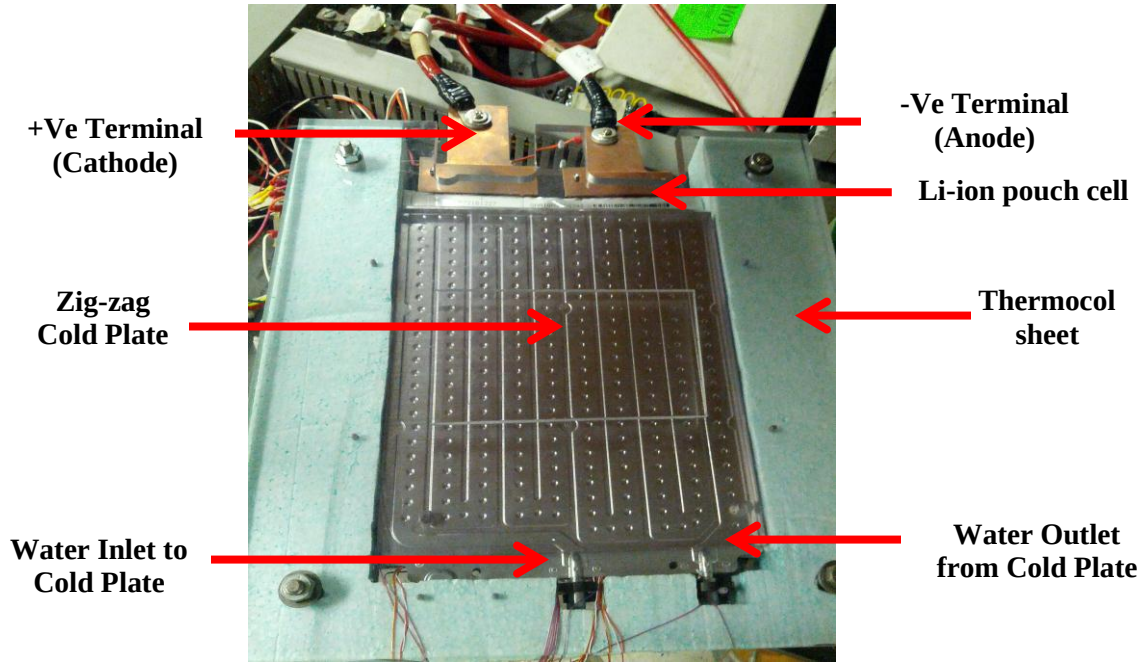

Figure 35 : Zig-zag cold plate set up (Active cooling)

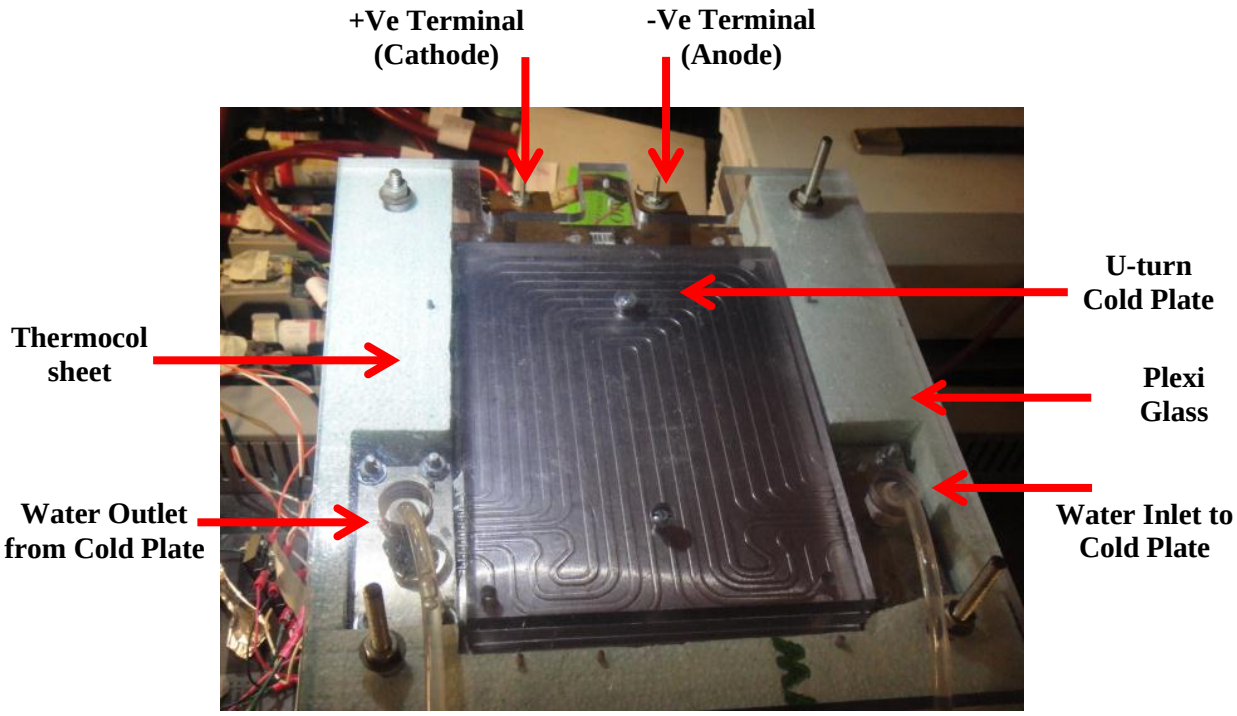

Figure 36 : U-turn cold plate set up (Active cooling)

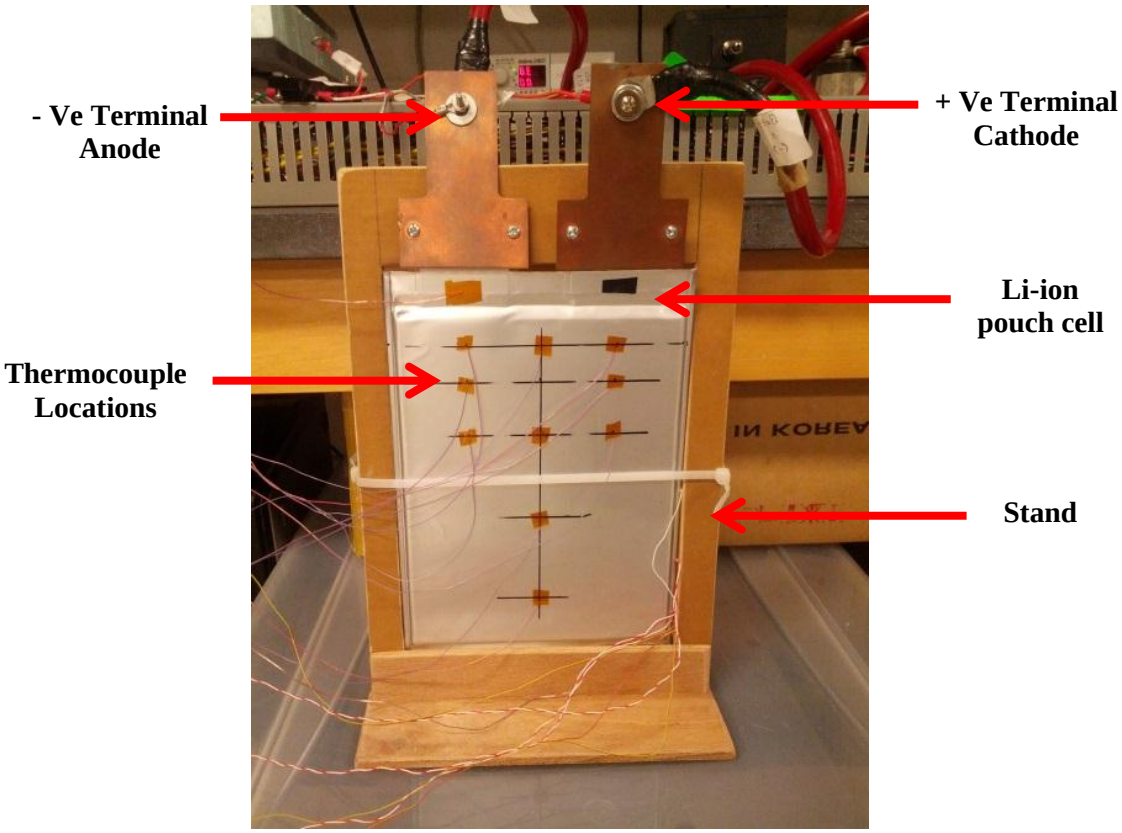

Figure 37 : Passive air cooling set-up

The locations of thermocouples and heat flux sensors attached the battery surfaces and cooling system is discussed in detail in following sections 3.1.2 and 3.1.3. All thermocouples and heat flux sensors are connected to the Keithley-2700 data acquisition system, which is connected to the test stand computer-2.

Two different commercial cooling plates were selected from industry to remove heat from the battery. Both coolant plates were manufactured from two stamped aluminum plates that are joined in a nickel-brazing process. The first plate tested was the "zig-zag" plate. This plate was characterized as having a single flow channel with the inlet placed at the top. The single flow channel ran down the length of the plate before turning back on itself, stepping one channel width across the plate with each turn. This flow pattern results in a thermal profile where coolant temperature gradient is largest across the width of the plate. Figure 35 shows the pictorial view of the zig-zag cold plate set-up.

The second plate tested was the "U-turn" cold plate. This plate was characterized as having multiple flow channels with inlets and outlets (9-inlets and 9-outlets) placed on the edges of the plate, near the bottom of the battery. The coolant flow paths are symmetrical down the center of the plate such that the flow channels were mirrored about the centerline. Figure 36 shows a picture of one of the two U-turn cold plates used in this test set-up. One cold plate is at the top of the pouch cell and the other cold plate at the bottom of the pouch cell. A Li-ion pouch cell is insulated from three sides (left, right, and bottom of the pouch cell along the height of the pouch cell) using polystyrene insulation to prevent heat loss from the pouch cell to the surrounding environment.

The thermal data acquisition system, the thermocouple locations, heat flux sensors locations, battery cooling system, sensors and flow meter, compression rig, battery, experimental plan and procedure, and data analysis method are presented in next section.

3.1.1 Thermal Data Acquisition

All measurements were performed using a Keithley 2700 data acquisition system. A 20 channel M7700 analog input module was used to connect to output terminals of all instruments. Data logging was programmed and controlled by a Windows based Excel add-in patch "ExcelLink" that provides instantaneous recording of values to an Excel sheet. This software is particularly useful as the immediate Excel format is easily worked with. The data acquisition hardware described is shown in Figure 38.

Figure 38 : Keithley 2700 data logger and M7700 input module

Sensors monitored by the thermal data collection system consisted of the following types: Thermocouples (TC) and Heat Flux Arrays (HFA). The majority of sensors were placed on the battery surfaces within the compression rig, while the remaining sensors were installed on the battery cooling system.

3.1.2 Thermocouple Locations

Thermocouples were installed on the principal surface of the battery to measure temperatures at ten discrete points. T-type 30 gauge, special limits of error (SLE) thermocouple wire were used on one side, and three additional K-type thermocouples integral to the heat flux arrays were present on the alternate side. The K-type thermocouple locations are discussed in next section. The location of T-type thermocouples is shown in Figure 39 and listed in Table 5.Kapton backed adhesive tape was used to adhere the thermocouples to the battery surface.

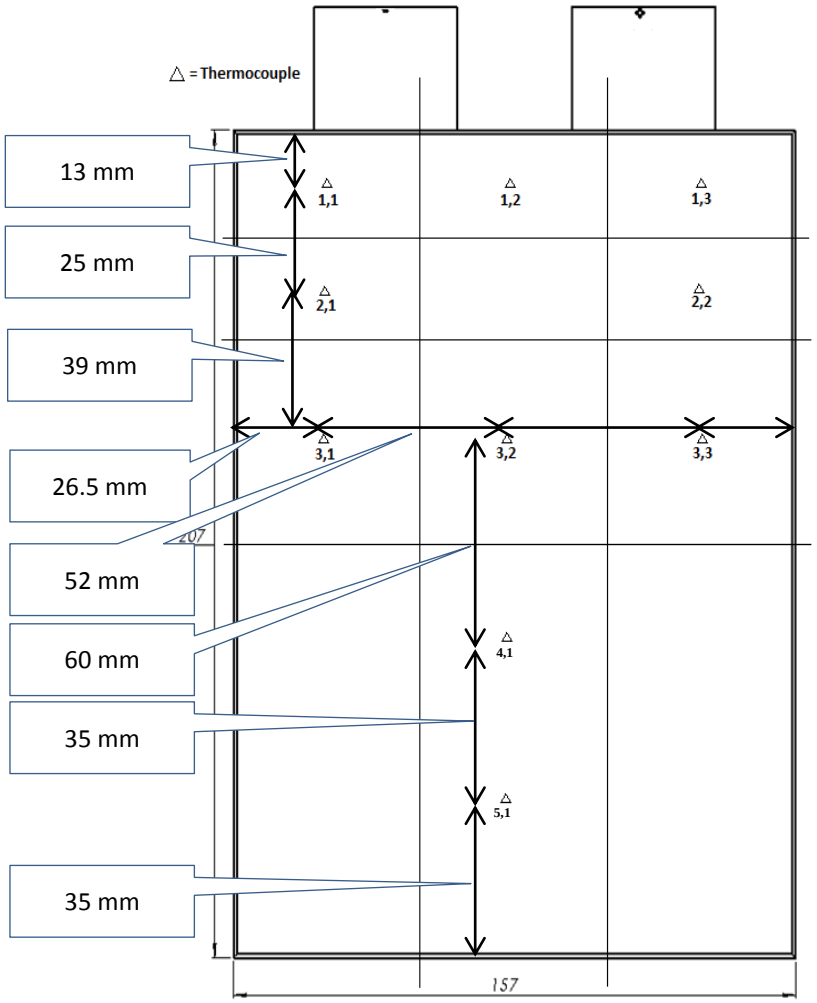

Figure 39 : Thermocouples locations on top surface of the cell

Table 5 : Distance of thermocouple locations from bottom left corner of the cell surface

Thermocouple	X (mm)	Y (mm)
1,1	26.5	194
1,2	78.5	194
1,3	130.5	194
2,1	26.5	169
2,2	130.5	169
3,1	26.5	130
3,2	78.5	130
3,3	130.5	130
4,1	78.5	70
5,1	78.5	35

3.1.3 Heat Flux Sensors Locations

Three thin-film heat flux sensors were installed on the surface opposite to the locations of the thermocouples. The locations of these three sensors are shown in Figure 40, and the x and y coordinates of HFA center points is given in Table 6.

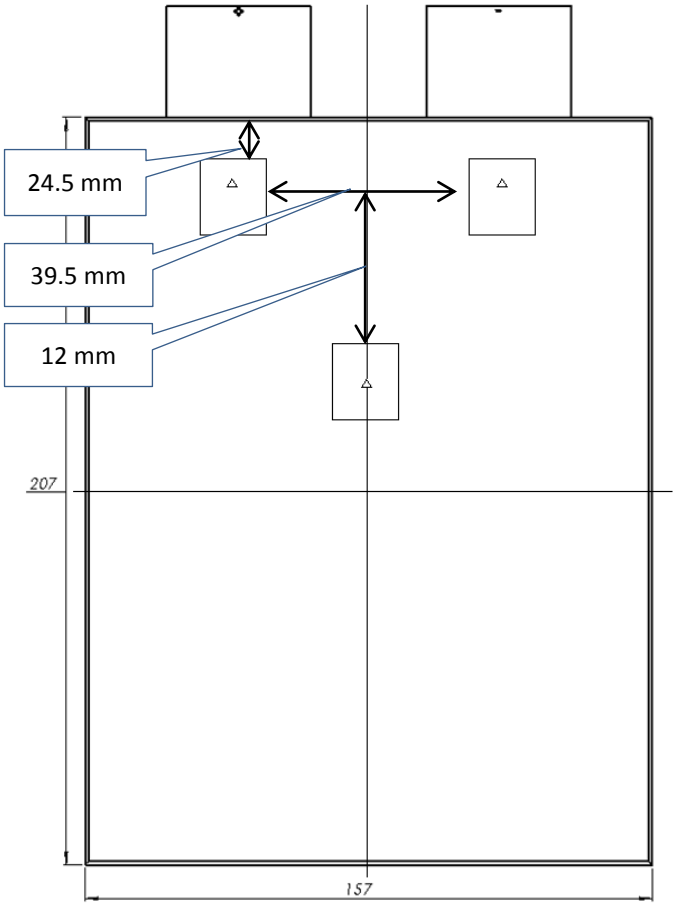

Figure 40: Locations of heat flux sensors

Table 6 : Locations of heat flux sensor centre-points distance from bottom left corner of the cell surface

Heat Flux Sensor	Location	Type of HFS	X [mm]	Y [mm]
1	(+) Electrode	HFS-4	104.7	169.8
2	(-) Electrode	HFS-4	52.3	169.8
3	Mid-surface	HFS-3	78.5	122.7

These sensors function as a self-generating thermopile transducer. They require no special wiring, reference junctions or signal conditioning. The HFAs utilize a multi-junction thermopile

construction on a polyimide film laminate. The output of the sensors provides an average measurement of surface heat flux in a 25.4 x 25.4 mm area (1 inch^2). Kapton backed adhesive tape was used to adhere the thermocouples to the battery surface.

3.1.4 Battery Cooling System

The battery cooling system consisted of a closed loop of tubing connecting two cooling plates (P1, P2) to a Fisher Scientific Isotemp 3016 fluid bath. Sensors were placed along the flow path to record properties of the fluid. A schematic of the system is shown in Figure 41. The cooling plates were placed within the compression rig directly against the principal surfaces of the battery such that heat generated within the battery was principally removed by conduction to the surfaces of the cooling plates.

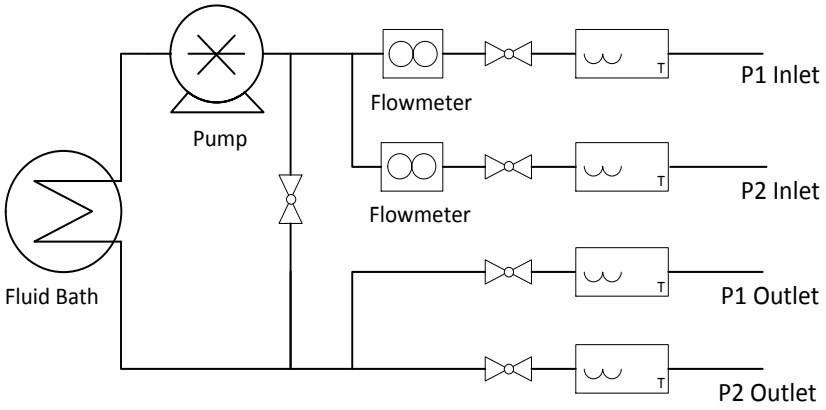

Figure 41: Schematic of cooling system flow from bath to upper and lower cold plates

3.1.5 Sensors and Flow Meter

Two types of sensors monitor the battery cooling system: thermocouples and flow meters. These sensors are required to determine the heat gained or lost by the fluid within the cooling plates. T-type insertion thermocouples are installed directly upstream and downstream of the inlet and outlet to each cooling plate. These thermocouples measure the bulk temperature of the fluid flowing within the coolant line. The Keithley 2700 records the output of these thermocouples.

A Microtherm FS1 30-300ml/min flow meter is installed directly upstream of the inlet to each cooling plate. An LCD display provides instantaneous measurement of volumetric flow. This volumetric flow value was manually recorded at the beginning and end of test cycles.

3.1.6 Compression Rig

For tests that include active cooling using the battery cooling system a special isolating rig was created. The rig was created to isolate the cell from the ambient thermal environment and maintain compression of the cooling plate/battery surface interface. An exploded assembly of the isolating rig without insulation is shown in Figure 42 and the CAD drawing of compression rig is shown in Figure 43.

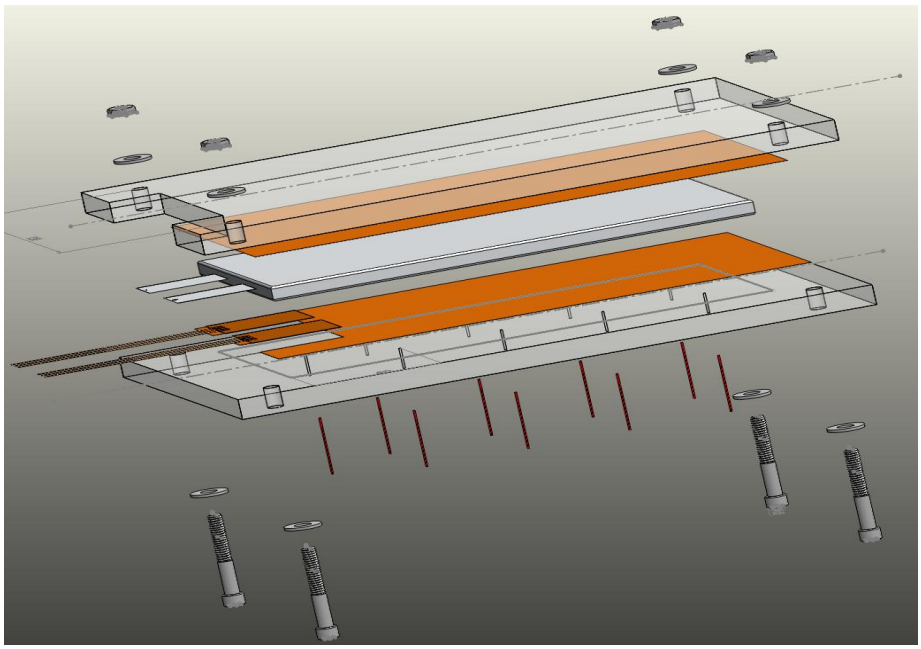

Figure 42: Exploded view of test rig

The rig is comprised of two transparent 12.7 mm thick polycarbonate sheets and in between the battery and cooling plates are sandwiched. A hole is present in each corner to allow a threaded bolt to pass through. By tightening down the bolt fasteners, the battery is confined to the assembly by pressure.

Spacers were constructed using 9.5 mm thick polycarbonate with dimensions equal to the battery dimensions. These spacers were required to change the distance between the cooling plate and the outer polycarbonate plate so that the inlet, outlet and tubing would fit.

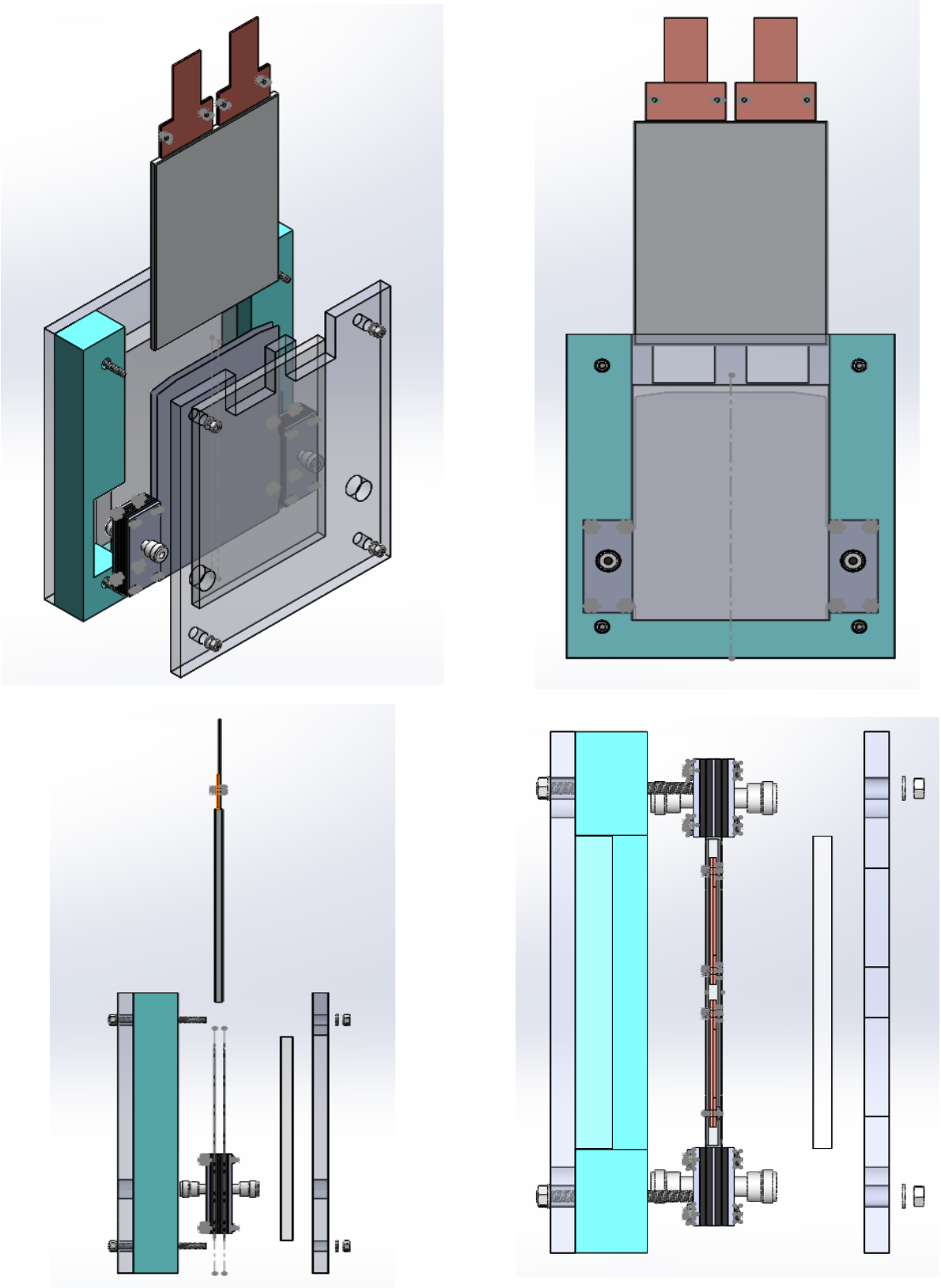

Figure 43 : CAD drawings of compression rig

3.1.7 Battery

In this work, 20Ah lithium-ion prismatic pouch cell, shown in Figure 44 is tested. The pouch cell specifications are given in Table 7. The two holes were made on tabs to connect to the power source and voltage sensing device.

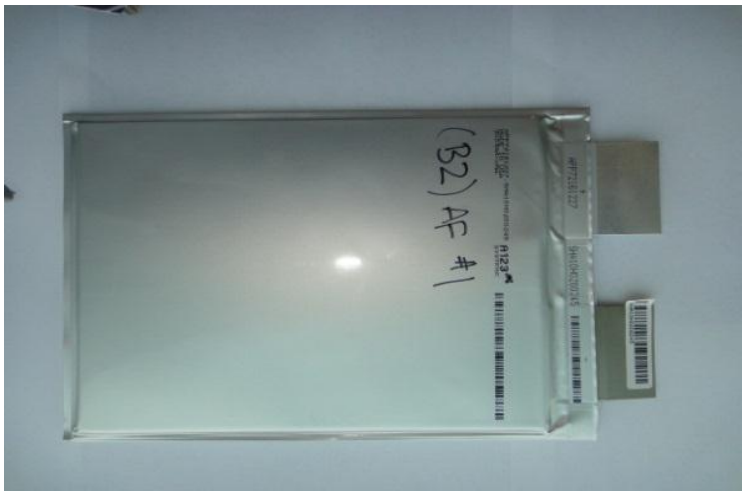

Figure 44 : $LiFePO_4$- 20Ah lithium-ion prismatic pouch cell

Table 7 : $LiFePO_4$- 20Ah lithium-ion prismatic pouch cell specifications

SPECIFICATION	VALUE
Cathode Material	$LiFePO_4$
Anode Material	Graphite
Electrolyte	Carbonate based
Nominal Capacity	20.0 Ah
Nominal Voltage	3.3 V
Nominal Energy	65 Wh
Energy Density	247 Wh / L
Mass	496 g
Discharge Power	1200
Dimensions	7.25 mm x 160 mm x 227 mm
Specific Power	2400 W / kg
Specific Energy	131 Wh / kg
Operating Temperature	- 30°C to 55°C
Storage Temperature	- 40°C to 60°C
Volume	0.263 L
Number of Cycles	Minimum 300, typical 2000
Max Discharge (SOC & Temperature dependent)	300 A
Max Charge (SOC & Temperature dependent)	300 A
Internal resistance	0.5 mΩ

3.1.8 Experimental Plan and Procedure

In this experiment, three different cooling types are tested: passive convection, active zig-zag cold plates, and active U-turn cold plates. For both cooling plates, four different coolant temperatures or boundary conditions are selected: 5 °C, 15 °C, 25 °C, and 35 °C. Four different discharge rates are selected: 1C, 2C, 3C, and 4C. The charge current is 1C. The experimental plan is shown in Table 8.

Table 8 : Experimental plan

Cooling Type	Ambient/Coolant/Bath Temperature [°C]	Discharge Rate
Passive (Ambient air only)	~22	1C, 2C, 3C, 4C
Active (Zig-zag turn cold plate)	5	1C, 2C, 3C, 4C
	15	1C, 2C, 3C, 4C
	25	1C, 2C, 3C, 4C
	35	1C, 2C, 3C, 4C
Active (U-turn cold plate)	5	1C, 2C, 3C, 4C
	15	1C, 2C, 3C, 4C
	25	1C, 2C, 3C, 4C
	35	1C, 2C, 3C, 4C

This procedure was followed to initiate battery cycling and the thermal data collection, and it does not directly describe the procedure for assembling the battery and cooling/instrumentation components within the compression rig. As such, this procedure assumes the cell and cooling components are correctly installed and fully connected to all other components as required.

1. The isothermal fluid bath and pump was turned on minimum 2 hour prior to beginning cycling to bring the battery, bath and compression rig to a steady state temperature. The valves leading to the cold plates were observed and set to open. The isothermal fluid bath was set to the desired cooling temperature or boundary conditions of 5 °C, 15 °C, 25 °C, and 35 °C for the test.
2. The lab view code for the charge discharge stand was loaded and relevant test parameters were input to the program. Relevant test parameters include:
    a. Charge current
    b. Discharge current

c. Number of cycles
d. Drive cycle (charge and discharge cycle)
e. Maximum voltage at end of charge
f. Minimum voltage at end of discharge
g. Measurement sample rate

3. The thermal data acquisition PC and Keithly 2700 were turned on and allowed to initialize. On the PC, the ExcelLink recording software was prepared for data acquisition. The following parameters were recorded within the recording software:
    a. Battery surface temperature (top and bottom surface of the pouch cell)
    b. Heat flux at top surface of the battery near electrodes
    c. Water inlet and outlet temperature at top and bottom cold plate
4. The internal clocks on both PCs were synchronized to the same time to allow combining data files.
5. The charge-discharge test stand and thermal data acquisition were then activated at the same time, such that charging/discharging and data acquisition begin at the same instant.
6. The test continued until the desired number of battery cycles was completed.
7. Two files were created for each test.
    a. Data from thermal data acquisition PC
    b. Electrical charge discharge data

3.2 Data Analysis Method

The data produced in the heat generation and cooling requirements experiment consists of electrical data (battery voltage, and current flow) as well as thermal data: surface temperature data (13 channels), heat flux meter output voltages (3 channels), inlet/outlet cooling system temperatures (4 channels). MATLAB software was used in order to manipulate the large spread sheets of data. The following energy balance equation was used to determine the actual heat output of the battery.

$$Q_{Total} = Q_{stored} + Q_{removed} + Q_{environment} \quad (20)$$

3.2.1 Sensible Heat (Q_{stored})

The heat stored in the battery is termed sensible heat. It is evaluated based on the change in temperature of the battery in conjunction with the specific heat value. Equation (21) is used to evaluate the sensible heat energy stored in the battery when the battery temperature changes from some initial temperature to a final temperature.

$$\underset{t_1\ to\ t_2}{Q_{sensible}} = m_{battery} c_{p,battery} (T_{t_2} - T_{t_1}) \tag{21}$$

A standard method of determining the average temperature across the entire battery surface has been devised to enable sensible heat calculations. For each thermocouple, it is assumed that the measured temperature represents the average of an area extending around the sensor. The areas are determined by defining each area boundary by calculating the x and y midpoint distance between adjacent sensors. Equation (22) is used to evaluate the average battery surface temperature by summing the temperature-area products and dividing by the total area of the surface.

$$\underset{average}{T_{surface}} = \frac{\sum(T_{ij} A_{ij})}{A_{total}} \tag{22}$$

The ten thermocouples measuring surface temperatures shown in Figure 39 are each assigned the areas that correspond to their locations as shown in Figure 45. The physical size of the thermocouple areas is presented in Table 9.

The rate of sensible heat accumulation is directly influenced by the battery heat generation rate and the heat transfer coefficient out of the system. The temperature of the battery increases as heat is generated due to the finite heat transfer coefficient to the surrounding. The rate of sensible heat accumulation is determined from the rate of change of equation (23), where $\frac{dT}{dt}$ is the rate that the battery temperature changes.

$$\dot{Q}_{sensible} = m_{battery} c_{p,battery} \frac{dT}{dt} \tag{23}$$

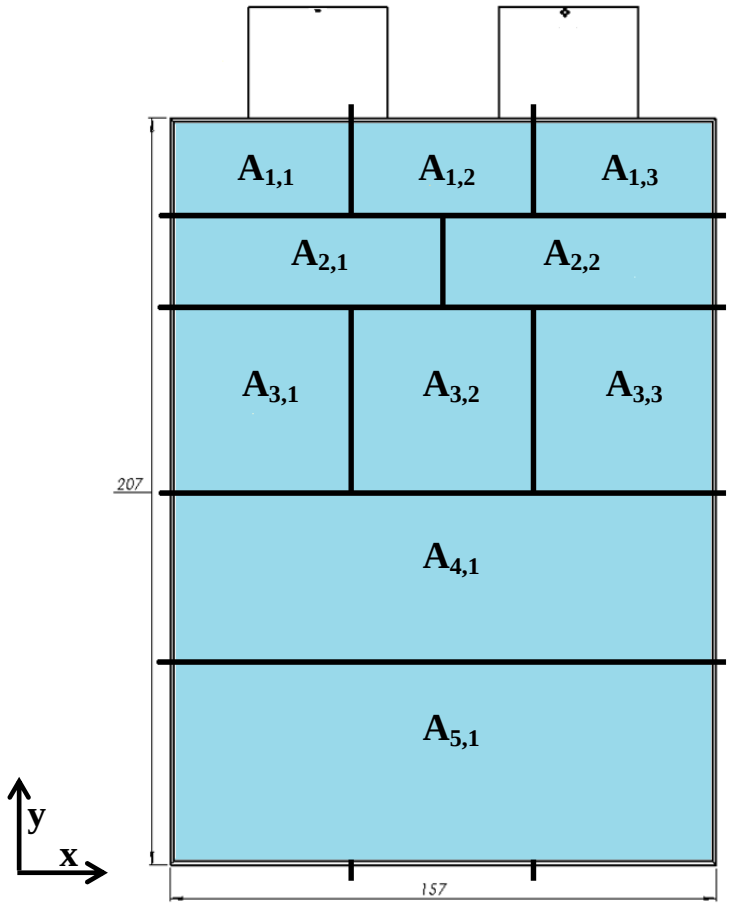

Figure 45: Distribution of areas used to determine average surface temperature

Table 9 : X and Y component lengths of thermocouple areas

Thermocouple	Area	X [mm]	Y [mm]	Area [m^2] (x10^{-3})
1,1	$A_{1,1}$	52.5	25.5	1.34
1,2	$A_{1,2}$	52	25.5	1.33
1,3	$A_{1,3}$	52.5	25.5	1.34
2,1	$A_{2,1}$	78.5	32	2.51
2,2	$A_{2,2}$	78.5	32	2.51
3,1	$A_{3,1}$	52.5	49.5	2.60
3,2	$A_{3,2}$	52	49.5	2.57
3,3	$A_{3,3}$	52.5	49.5	2.60
4,1	$A_{4,1}$	157	47.5	7.46
5,1	$A_{5,1}$	157	52.5	8.24

The rate of temperature change is evaluated by measuring temperature at two times and calculating the rate using equation (24)

$$\frac{dT}{dt} = \frac{(T_{t_2} - T_{t_1})}{t_2 - t_1} \tag{24}$$

The rate of sensible heat accumulation can then be determined via equation (25).

$$\dot{Q}_{\substack{sensible \\ t_1 \, to \, t_2}} = m_{battery} \, c_{p,battery} \, \frac{(T_{t_2} - T_{t_1})}{t_2 - t_1} \tag{25}$$

3.2.2 Heat Removed from Battery ($Q_{removed}$)

A fraction of the heat generated by the battery is removed by cooling processes. In one series of testing, the operating battery was placed in a vertical position and ambient air carried heat away by natural convection. In other tests, cooling plates were present that utilized forced coolant flow to remove heat.

3.2.2.1 Air Cooling

For a fluid at known temperature contacting a surface of known area, heat is transferred via convection and observes Newton's law of cooling.

$$Q_{convection} = h_c \, A \, (T_{surface} - T_\infty) \tag{26}$$

If the heat transfer coefficient, h and surface temperature is known, the corresponding heat transfer can be calculated. Determining h represents the fundamental challenge of thermal convection. The coefficient is not itself a thermo-physical property of the fluid, but is dependent on numerous variables such that:

$$h_c \; = \; f \, (\rho, C_p, \mu, \beta, g, k, [\, T - T_f], L) \tag{27}$$

Nusselt numbers are proportional to h_c via the following relation:

$$Nu_L = \frac{h_c L_{surface}}{k_{fluid}} \tag{28}$$

Correlations for Nusselt numbers have been developed in experimental tests and are readily available in mainstream heat transfer texts. These correlations correspond to specific geometries and care must be taken when selecting the appropriate correlation to use. For buoyancy driven laminar fluid flow across a vertical plate, the following correlation is found [116]:

$$Nu_L = 0.68 + \frac{0.670(Ra_L)^{1/4}}{\left[1 + \left(\frac{0.492}{Pr}\right)^{9/16}\right]^{4/9}} \ldots\ldots Ra_L \leq 10^9 \quad (29)$$

The Prandtl number, Pr is tabulated for different fluid temperature values in heat transfer texts and is evaluated at the film temperature, which is the average temperature between the fluid and the surface to be cooled. The Rayleigh number is calculated by the standard relation:

$$Ra_L = \frac{g\beta}{\nu\alpha}\left(T_{surface} - T_\infty\right) L^3 \quad (30)$$

3.2.2.2 Water Cooling (Cold plates)

Cooling plate heat removal rate is determined by the inlet and outlet thermocouple data, in conjunction with the recorded flow rates. The difference in inlet and outlet temperatures is due to heat conducted from the battery surface. The heat removed by a single cooling plate is calculated using equation (22).

$$\dot{Q}_{Cooling\ Plate} = \dot{m}_w C_{p,w}\left(T_{w,o} - T_{w,i}\right) \quad (31)$$

The total amount of heat removed by the cooling plates for a time period Δt can be determined using equation (32).

$$Q_{Cooling\ Plate} = \dot{m}_w\ C_{p,w}\left(T_{w,out,average} - T_{w,in,average}\right)\Delta t \quad (32)$$

The term $T_{w,out,average}$ is the average measured outlet temperature during the period Δt, as in equation (33). N_T represents the number of temperature readings in the summation.

$$T_{w,out,average} = \frac{\sum T_{w,o}}{N_T} \quad (33)$$

3.2.3 Heat from Environment ($Q_{environment}$)

The compression rig is not perfectly insulated and as such, cooling plates measurements incorporate a component of heat gain or loss from the environment. When the cooling is set to 5°C, a temperature difference of approximately 17°C is established between the inside surface of the compression rig and the ambient air. This results in heat transfer between the ambient

environment and the cooling fluid. This additional heat is measured as an increased temperature difference between the inlets and outlets. For tests above ambient temperature, the opposite occurs. This additional heat affects the temperature difference between the inlets and outlets.

In order to evaluate this effect, the cooling system and thermal data acquisition was activated with the battery in place but no charging or discharging occurring. In this way, the temperature difference between the inlet and outlet of each cooling plate could be recorded. The average difference for each plate along with the respective flow rates used were used to quantify the heat removed or added by the environment using the method presented in above section of cold plates. The heat removed or added by the environment for different coolant temperature is shown in Table 10. The data is plotted in Figure 46.

Table 10 : Ambient heat flow to compression rig for different coolant temperature

Bath Temperature [°C]	$\dot{Q}_{environment}$**[W]**
5	-21.61
15	-11.24
25	4.12
35	18.10

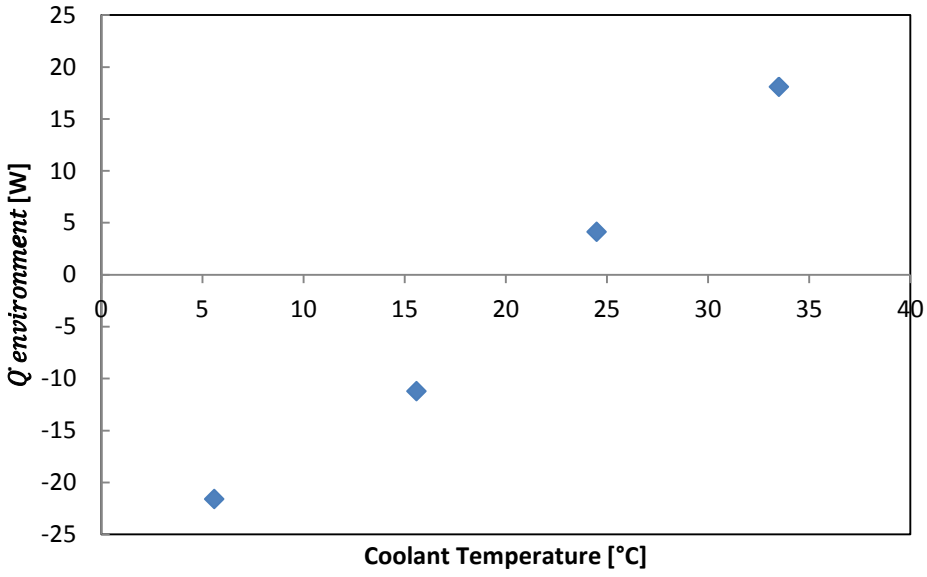

Figure 46 : Ambient heat flow to compression rig for four coolant temperatures

3.3 Results and Discussion

In this section, the temperature distribution on the principle surface of battery, maximum surface temperature of battery, average and peak heat flux, the total heat generation and heat generation rate, effect of discharge rate and operating temperature on discharge capacity, and thermal images are presented and discussed in detailed with different discharge rates and various boundary conditions. The uncertainty analysis associated with above results is presented in Chapter 7.

3.3.1 Battery Surface Temperature Profile

The battery surface temperature profile recorded by ten thermocouples at 4C discharge and 5 °C and 35 °C bath temperature are plotted as a function of depth of discharge (DOD) in Figure 47 and Figure 48. It can be observed that the response of the thermocouple at location (1, 1), (1, 2), and (1, 3) has the faster rate of increase over entire period of 0.0 and 1.0 depth of discharge (DOD). These thermocouples are nearest the negative and the positive electrodes of the battery and indicate the location of highest heat accumulation, and likely the rates of heat generation are highest near the electrodes. By comparing the images, it can be seen that the higher temperature distribution is noted for 4C-35 °C as compared to 4C-5 °C.

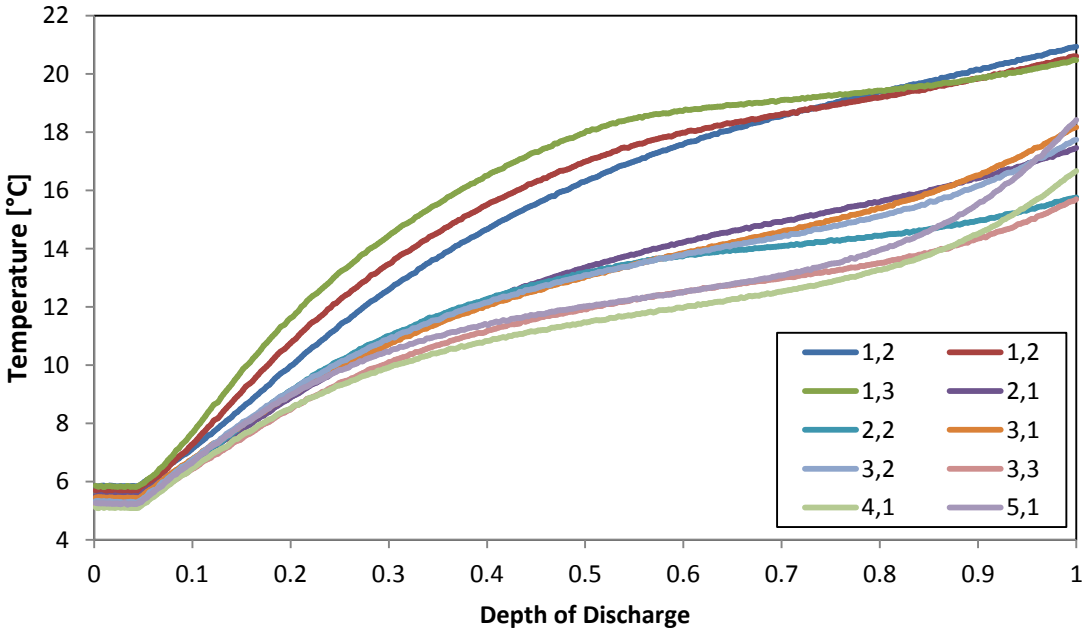

Figure 47 : Surface temperature profile at 4C discharge and 5^0C bath temperature

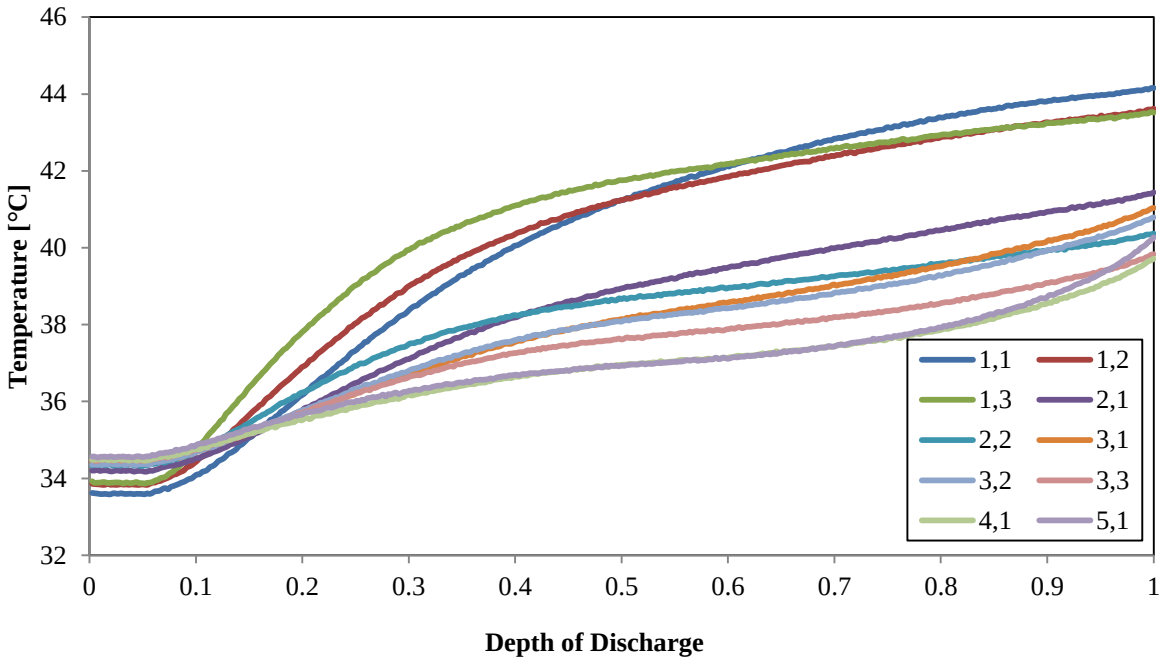

Figure 48 : Surface temperature profile at 4C discharge and 35 ^{0}C bath temperature

3.3.2 Average Surface Temperature of Battery

In Figure 49 the maximum average surface temperatures of the battery for the four discharge rates and operating/cooling/bath temperatures has been plotted. The trend shows that regardless of operating temperature the maximum average surface temperature of the battery increases as the discharge rate is increased. In Table 11 the maximum average surface temperatures are summarized for the test conditions used.

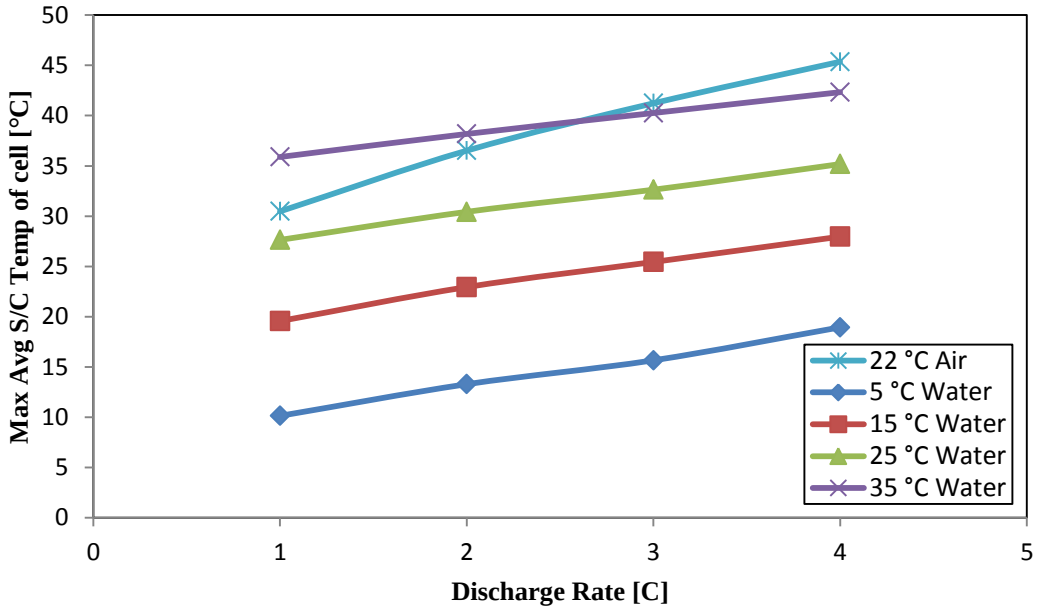

Figure 49 : Maximum average surface temperature of battery for discharge rates and coolant/operating temperatures tested

Table 11 : Maximum average battery surface temperature for different discharge rates and bath temperatures

Cooling Type	Ambient/Coolant/Bath Temperature [°C]	Maximum Temperature [°C]			
		1C	2C	3C	4C
Active (U-turn cold plates)	5 °C	10.1	13.3	15.7	18.9
	15 °C	19.6	22.9	25.4	28.0
	25 °C	27.6	30.4	32.6	35.2
	35 °C	35.9	38.2	40.3	42.3
Passive (Ambient air only)	~22 °C	30.5	36.5	41.2	45.4

Since the increase in coolant/operating/bath temperature can account for much of the differences in Figure 49, it is useful to consider the difference between the start of discharge average surface temperature and the end of discharge average surface temperature. This provides a measure of the buildup of heat within the battery. The differences are plotted in Figure 50. Table 12 shows the linear fit for four different bath temperatures.

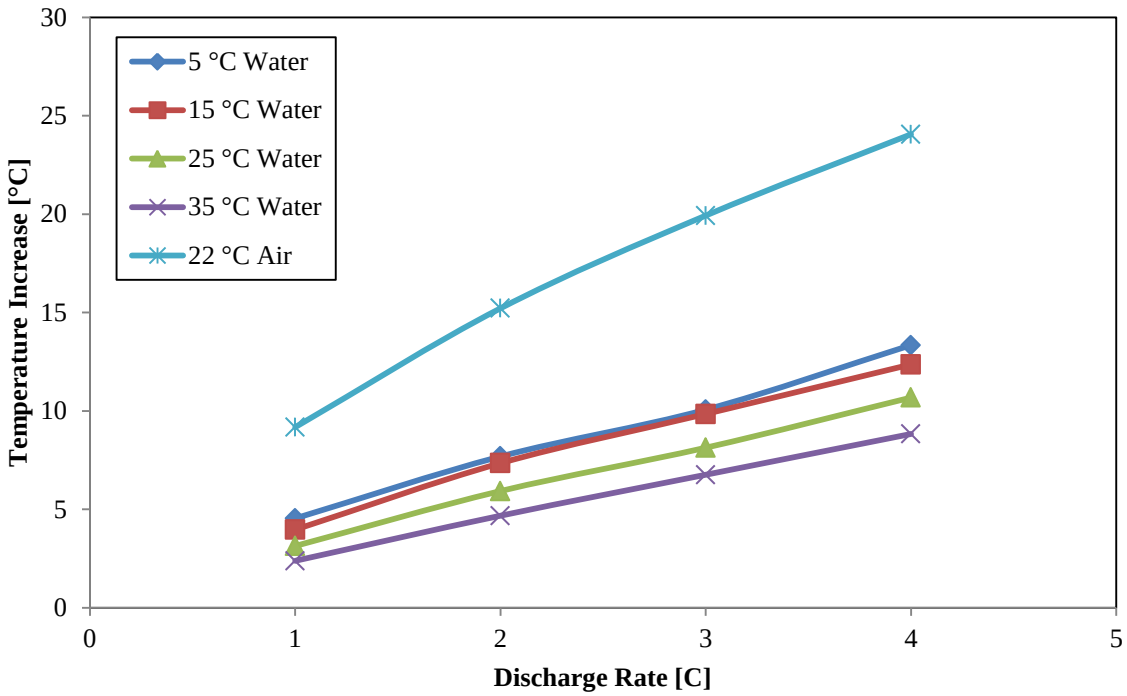

Figure 50 : Difference in average surface temperature between start and end of discharge

Table 12 : Linear fit for four different bath temperatures

Bath Temperature	Linear Fit
5 °C	$2.879\,x\ +\ 1.711$
15 °C	$2.769\,x\ +\ 1.510$
25 °C	$2.483\,x\ +\ 0.764$
35 °C	$2.142\,x\ +\ 0.369$

3.3.3 Average Heat Flux

In Figure 51 the average heat fluxes measured by the three heat flux sensors for all operating temperatures are plotted against discharge rate. To refresh the reader, HFS 1 is located near the positive electrode (cathode), HFS 2 is located near the negative electrode (anode), and HFS 3 is located at the middle of the cell along the height of the cell. It is observed that the highest average heat fluxes were measured at HFS 1 and HFS 2 for 4C discharge rates and 5 °C cooling. In general, for all tests the sensors nearest the electrodes (HFS 1 and 2) measured heat fluxes higher than the sensor located at the middle of the battery surface. The trend observed is that increased discharge rates (between 1C, 2C, 3C, and 4C) and decreased operating temperature (between 35 °C, 25 °C, 15 °C, and 5 °C) results in increased average heat fluxes at the three locations measured.

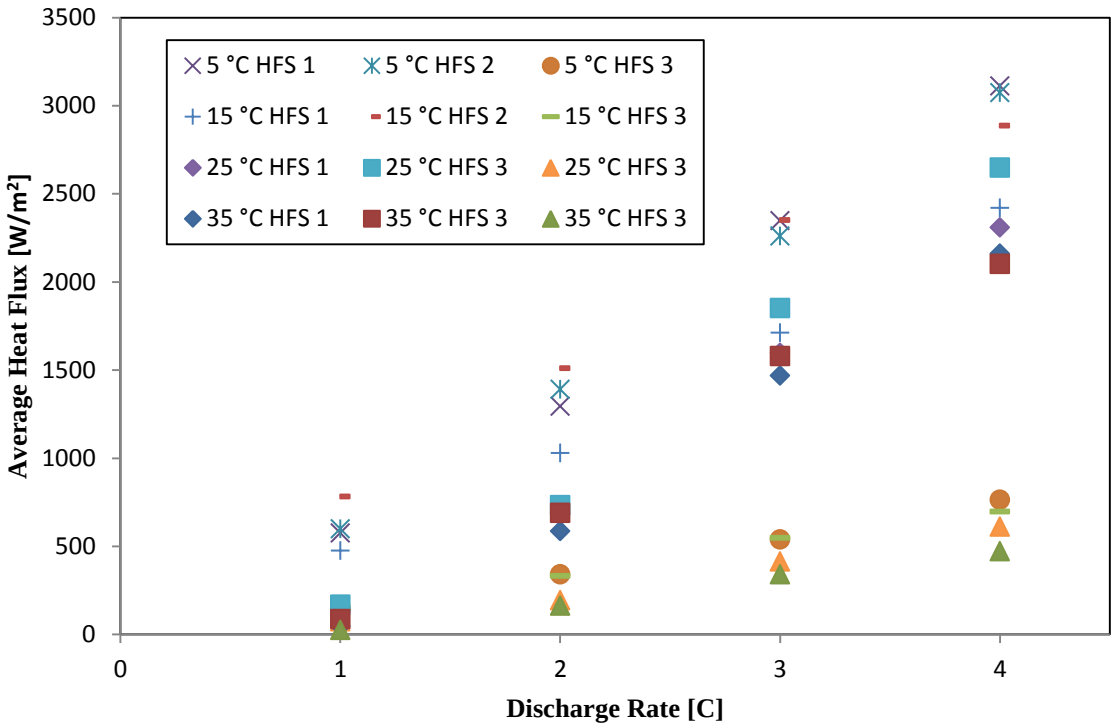

Figure 51 : Average heat flux at 1C, 2C, 3C, 4C discharge rates and different boundary conditions

Table 13 : Summary of average heat flux at 1C, 2C, 3C, 4C discharge rates and different boundary conditions

Cooling Type	Ambient/Coolant/Bath Temperature [°C]	Average Heat Flux [W/m^2]				
		Position	1C	2C	3C	4C
Passive (Ambient air only)	~22	1	42.3	130.3	238.4	343.6
		2	46.3	145.7	239.6	373.4
		3	24.6	71.1	108.6	145.3
Active (U-turn cold plates)	5	1	575.5	1294.5	2347.7	3112.2
		2	599.3	1390.8	2259.5	3072.8
		3	149.4	341.3	539.3	764.1
	15	1	475.7	1029.7	1711.8	2419.0
		2	781.4	1509.9	2351.6	2887.1
		3	157.9	331.7	548.4	697.3
	25	1	148.2	684.9	1597.3	2309.3
		2	168.9	733.2	1851.6	2648.2
		3	74.4	194.8	413.0	611.1
	35	1	47.6	585.6	1468.4	2160.2
		2	86.1	689.7	1579.9	2101.5
		3	25.2	163.3	340.6	471.8

In Table 13 the values of Figure 51 are tabulated along with the average heat fluxes for the passive cooling natural convection cases. For the passive cases, the average heat flux of HFS 2, near the negative electrode is always highest. Liquid cooling cases do not show a definitive pattern between HFS 1 and 2. This is likely due to the slightly uneven cooling gradient across the U-turn cold plate. The coolant temperature and thus plate temperature increases across the width of the battery surface as heat is absorbed. This is in contrast to the passive cooling case, where the vertical orientation of the battery provided a condition where cooling potential is approximately equal across the width of the surface. It could be inferred that the passive cooling cases are a better representation of the differences in heat generation between the three locations.

3.3.4 Peak Heat Flux

In Figure 52, the peak heat fluxes measured by the three heat flux sensors for all operating temperatures (5 °C, 15 °C, 25 °C, and 35 °C) are plotted against discharge rates of 1C, 2C, 3C, and 4C. It is observed that the highest peak heat fluxes were always measured at HFS 2. In general, for all tests the sensors nearest the electrodes (HFS 1 and 2) measured greater peak heat fluxes than the sensor located at the middle of the battery surface. The trend observed is that increased discharge rates and decreased operating temperature results in increased peak heat fluxes at the three locations measured.

In Table 14, the values of Figure 52 are tabulated along with the average heat fluxes for the passive cooling natural convection cases.

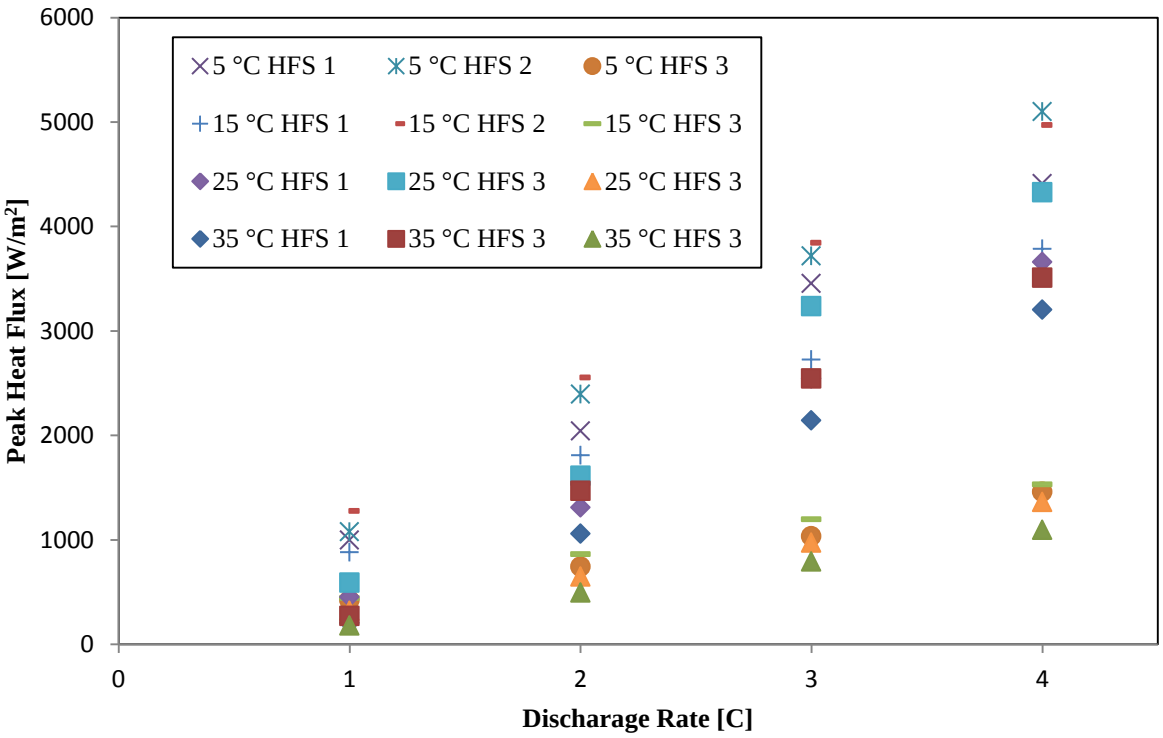

Figure 52 : Peak heat flux at 1C, 2C, 3C, 4C discharge rates and different boundary conditions

Table 14 : Summary of peak heat flux at 1C, 2C, 3C, 4C discharge rates and different boundary conditions

Cooling Type	Ambient/Coolant/Bath Temperature [°C]	Peak Heat Flux [W/m^2]				
		Position	1C	2C	3C	4C
Passive (Ambient air only)	~22	1	134.4	315.7	446.6	630.0
		2	140.5	292.8	485.6	763.2
		3	105.9	195.9	246.6	340.8
Active (U-turn cold plate)	5	1	998.9	2043.4	3454.6	4410.9
		2	1076.7	2395.1	3718.5	5099.7
		3	421.3	744.4	1033.2	1461.3
	15	1	882.5	1808.5	2726.3	3783.9
		2	1275.8	2554.2	3842.7	4972.2
		3	443.2	864.4	1196.1	1532.3
	25	1	453.1	1311.7	2543.9	3660.9
		2	589.1	1613.7	3235.6	4327.5
		3	321.3	648.3	972.3	1363.8
	35	1	204.8	1059.9	2143.7	3202.4
		2	272.6	1469.4	2545.8	3508.4
		3	180.7	495.9	793.5	1094.5

3.3.5 Heat Generation Rate

Figure 53 shows the measured heat generation rates of the battery for 2C discharge rates at 5°C , 15°C , 25°C ,and 35°C coolant/operating/bath temperature as a function of depth of discharge (DOD) varying from 0 to 1. A steep rise is seen in the first 0.04 of discharge, the heat generation rate becomes approximately constant until 0.5 DOD when a steady increase is observed. The increase appears to become steeper as the discharge progresses and is highest just before the end of discharge (>0.95 DOD). It was also noted that the highest heat generation rate was 90.7W measured at 4C discharge rate and 5°C coolant/bath temperature and minimum value (12.5W) was obtained at 1C and 35°C. Furthermore, it can be seen that the increase in discharge rate and thus discharge current causes consistent increase in the heat generation rate for equal depth of discharge points.

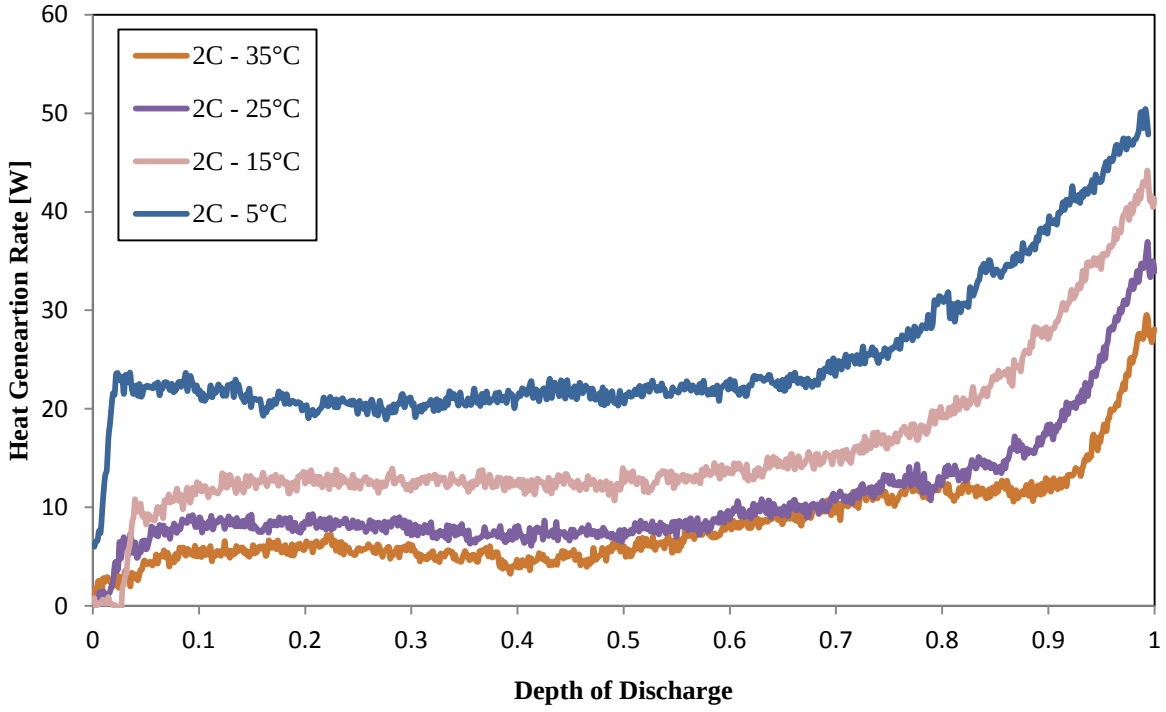

Figure 53 : Heat generation rate at 2C discharge and different bath temperatures

The increased heat generation can be accounted for by looking at Equation (7) and (8) . As the current is increased with the discharge rate, the irreversible Ohmic heating term becomes larger. From Equation (8), the current collector heat generation increases with the square of current. From this it follows that more heat will be generated at higher discharge rates. In Table 15 the

maximum heat generation rates that the battery discharges with liquid cooling plates produced are tabulated.

Table 15 : Summary of maximum heat generation rate at 1C, 2C, 3C, 4C discharge rates and different boundary conditions

Cooling Type	Operating/Coolant Temperature [°C]	Maximum Heat Generation Rate [W]			
		1C	2C	3C	4C
Active (U-turn cold plate)	5	24.0	50.4	68.3	90.7
	15	22.5	44.2	73.8	88.7
	25	19.4	36.9	56.2	82.3
	35	12.5	29.5	38.7	48.5

The battery discharge voltage profile corresponding to 2C discharge and four operating conditions shown in Figure 53 is described in Figure 54. It can be seen that when operating temperature (bath temperature) decreases from 35°C to 5°C, the discharge voltage profile also decreases. Similar plots (heat generation rate and voltage profile) were obtained for 1C, 3C, and 4C discharge rates and different bath temperatures and are presented in Appendix B.

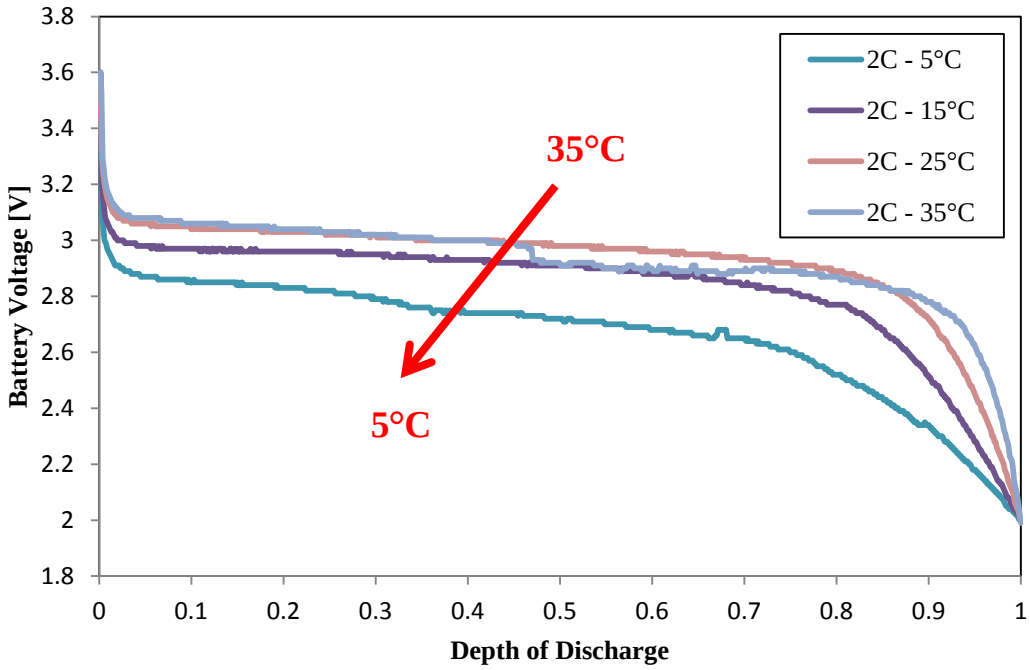

Figure 54 : Battery voltage versus depth of discharge

3.3.6 Total Heat Generated

Figure 55 shows the total heat generated in KJ in the battery during four discharge rates (1C, 2C, 3C, and 4C) are determined using the energy balance presented in Equation (20). In general, the trend shows that increased discharge rate and decreased temperatures result in increased amount of heat produced during a discharge. In Table 16, a summary of the total heat generation values for the above mentioned discharge rates and operating temperatures is provided. The highest value of heat produced was found to be 41.34 kJ when the operating/coolant temperature was at 5 °C and the discharge rate 4C. This is almost twice the heat generated by the equivalent discharge at 35°C (an increase of approx. 30 °C).

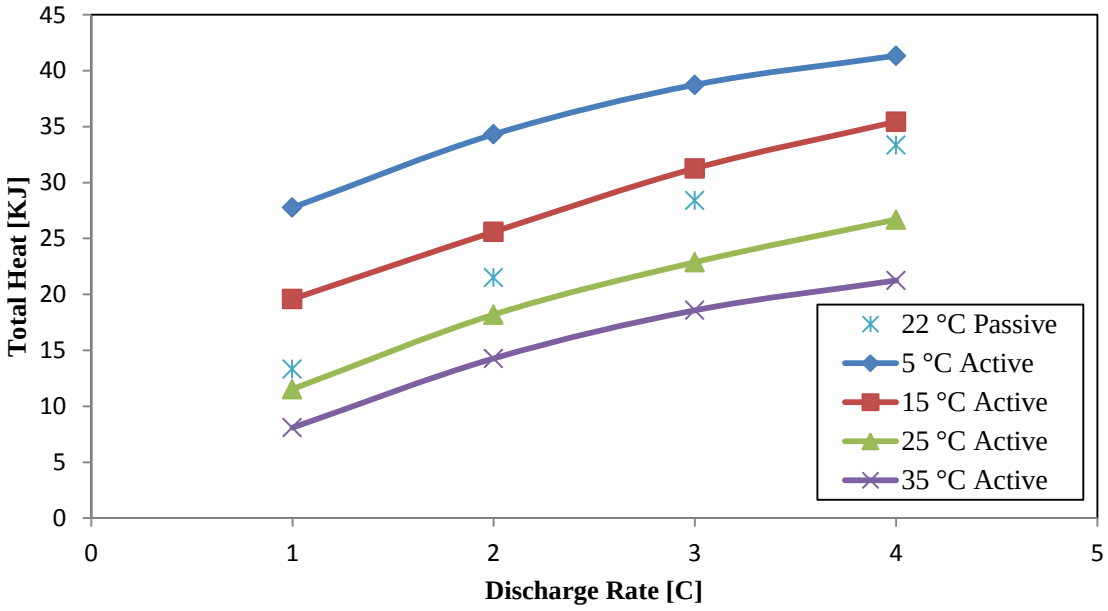

Figure 55 : Total heat generated at different discharge rates and different boundary conditions

Table 16 : Summary of total heat generated at 1C, 2C, 3C, 4C discharge rates and different boundary conditions

Cooling Type	Ambient/Coolant Temperature [°C]	Total Heat Generated [KJ]			
		1C	2C	3C	4C
Passive (Ambient air only)	~22	13.34	21.52	28.41	33.35
Active (U-turn cold plate)	5	27.76	34.31	38.74	41.34
	15	19.59	25.59	31.27	35.44
	25	11.54	18.20	22.88	26.70
	35	8.09	14.28	18.58	21.25

An analysis of uncertainty presented in Chapter 7 determined the uncertainty in total heat generation values is strongly influenced by the range of average surface temperatures measured during a discharge. In Chapter 7, the uncertainty is listed for each operating/cooling temperature. The 5 °C operating temperature tests resulted in the highest values of uncertainty, at 44.9%. The relative uncertainty decreased in higher temperature tests to minimums of 34.5% with cooling plates and 24.5% with 22 °C natural convection cooling tests. The large difference in uncertainty between the cooling plate tests and natural convection tests is due to the absence of flow meter uncertainty when only natural convection accounted for cooling. The flow rate uncertainty is the largest factor in the cooling plate heat calculations and greatly affects the overall uncertainty of heat generation calculations when cooling plates are utilized.

3.3.7 Effect of Discharge Rate and Operating Temperature on Discharge Capacity

In Figure 56, the discharge capacity (Ah) of the battery is plotted against four discharge rates of 1C, 2C, 3C, and 4C for all five cooling conditions (Active cooling : 5°C, 15°C, 25°C, 35°C and passive cooling). This illustrates the effect of discharge rate and operating temperature on the electrical performance of the batteries. This is of particular concern for EV development as battery capacity directly impacts vehicle range. Due to the aggressive charging and discharging profiles used, the battery never discharged the nominal 20 Ah as specified by the manufacturer. Since the charging conditions were held constant between tests, the battery performance in each test is still comparable.

In Table 17 the values displayed in Figure 56 have been tabulated. In general, battery discharge capacity decreases as coolant/operating temperature decreases from 35 °C to 5 °C and battery discharge rate increases from 1C to 4C.

Another measure of discharge capacity is discharge time. The constant current discharges are within 0.1% of the nominal current draw at all times and thus increased discharge times indicate more energy discharged from the battery. In Table 18, the discharge times are summarized.

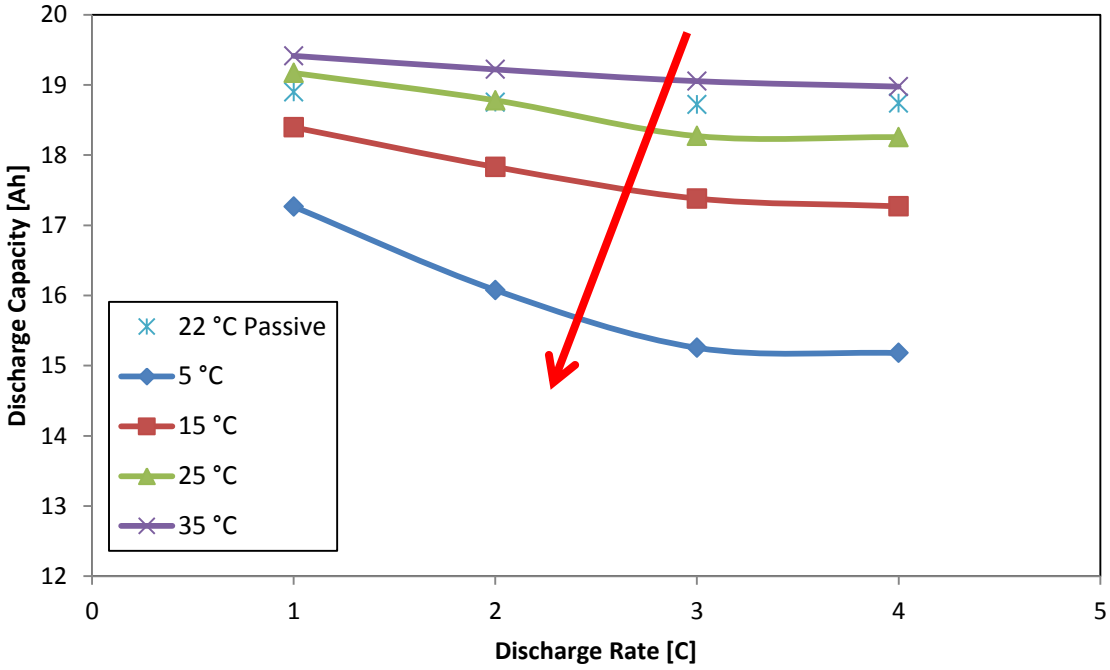

Figure 56 : Effect of operating temperatures on discharge capacities

Table 17 : Summary of discharge capacities at 1C, 2C, 3C, 4C discharge rates and different boundary conditions

Cooling Type	Ambient/Coolant Temperature [°C]	Discharge Capacity [Ah]			
		1C	2C	3C	4C
Passive (Ambient Air Only)	~22	18.90	18.75	18.72	18.74
Active (U-turn cold Plates)	5	17.27	16.08	15.26	15.18
	15	18.40	17.83	17.38	17.27
	25	19.17	18.78	18.27	18.26
	35	19.41	19.22	19.05	18.98

Table 18 : Summary of discharge times at 1C, 2C, 3C, 4C discharge rates and different boundary conditions

Cooling Type	Operating/Coolant Temperature [°C]	Discharge Time [s]			
		1C	2C	3C	4C
Passive (Ambient Air Only)	~22	3406	1689	1123	843
Active (U-turn cold Plates)	5	3100	1445	914	706
	15	3318	1604	1043	778
	25	3448	1689	1096	821
	35	3488	1729	1142	854

3.4 Thermal Image

In order to obtain the thermal image finger-print of the surface of any object, Infrared (IR) equipment is generally used. A camera equipped with an IR detector can capture different energies radiated from different surface temperatures from an object. The IR equipment converts the energy back to the temperature. This is a great tool for finding temperature distribution or hot spots on the surface of an object without using any intrusive temperature sensors.

In this experiment, a thermo graphic camera is used to produces images of battery surfaces to visually observe temperature distribution. Thermal gradients are determined using manufacturer provided software. An S60 FLIR ThermaCam as shown in Figure 57 was used to produce IR images of the battery undergoing discharge. This thermal camera has a 320 x 240 detector, standard temperature range $0 - 500\ ^0C$ and an accuracy of 2 % (typically 2 ^0C). The sensor is able to detect temperature variances as small as 0.06 °C [117].

Figure 57 : Flir S60 Therma Cam [117]

The thermal imaging set up is shown in Figure 58. The battery was placed on a cardboard stand constructed to hold the battery at a 45^0 angle relative to the plane of the thermal detector. This arrangement eliminates the detection of radiation emitted or reflected by the camera and operator. To eliminate reflection from the ceiling and other objects in the environment a large cardboard box was placed over the battery and stand. The camera was positioned on a tripod outside the enclosing box and pointed such that the detector viewed only the battery and interior of the box.

Flir Therma CAM S60 during IR image **Li-ion pouch cell at 45 ^{0} angle**

Figure 58 : Thermal Image set-up

3.4.1 Procedure

In this section, the experimental procedure for recording the IR images of a Li-ion battery during discharging is discussed.

1. The battery was placed in the stand built to hold the battery at 45^0.
2. The isolating box was placed over the battery and stand.
3. The positive and negative leads were connected to the battery electrode tabs. The leads entered the box through an access hole.
4. Charging was performed on the battery until the battery reached a fully charged state.
5. When the battery was fully charged, the camera was oriented in a level position and pointed such that it viewed only the interior of the box and the surface of the battery. Settings in the camera were prepared to record images at 20 second intervals once underway.
6. Discharge current rate was modified in the battery cycling stand computer, and the internal clocks on the camera and computer were synchronized. The battery discharge and camera recording were then activated simultaneously.
7. At the end of discharge, the battery was recharged, and the images were removed from the camera to create space for following tests.

3.4.2 Plan

In this experiment, three constant current discharge rates were selected. The corresponding equivalent current and time are shown in Table 19.

Table 19 : Discharge rates and equivalent current and time.

Discharge Rate	Constant Current value	Time of discharge
2C	40A	1/2 hour
3C	60A	1/3 hour
4C	80A	1/4 hour

3.4.3 Thermal Images at 2C, 3C, and 4C

Thermal images were captured every 20 seconds with the thermal camera. The following subsections are titled "XX Discharge" where "XX" represents the discharge rate. For each set of images, a regular interval was chosen to reduce the number of images displayed. The elapsed time since start of discharge (SOD) is indicated below each image. State of charge at time of image is also indicated to provide a point of comparison between image series. Table 20 lists the image series and their respective interval lengths.

Table 20 : Parameters of image series in following subsections.

Image Series	Figure #	Image Interval (s)	Left Side of Image	Right Side of Image
2C Discharge	Figure 59	240	Positive Electrode	Negative Electrode
3C Discharge	Figure 60	180	Positive Electrode	Negative Electrode
4C Discharge	Figure 61	180	Negative Electrode	Positive Electrode

The image sets of different discharges all illustrate that the heat generation across the surface of the battery is non-uniform. In all images, the area of highest temperature is at the negative electrode, indicating that this is where the greatest source of heat generation is located. Specifically, the hottest spot appears to be where the current collector tabs of the individual electrode sheets are bonded to the external current tab that the external system connects to.

Using Equation (7) to describe this heat generation is clearly not adequate as the heat generation due to the Ohmic heating at the tab/collector interface and within the tab itself is ignored. The images show that this heat generation is far from negligible, and is in fact the largest source of heat generation in this particular battery design. Hence, Equation (8), which contains several additional terms is the correct relation to use when estimating heat generation of prismatic lithium-ion batteries.

In order to minimize this heat generation term, the resistance of the joint formed from bonding the current collectors of the electrodes to the external tab should be as small as possible. On this particular battery design, the thickness of the negative electrode tab is smaller than the positive tab, despite being of equal area. This causes the volumetric current density in the negative tab to increase. Without an equivalent decrease in electrical resistance due to material properties, this will cause higher heat generation as the last two terms of Equation (8) indicate.

3.4.4 IR Image at 2C Discharge

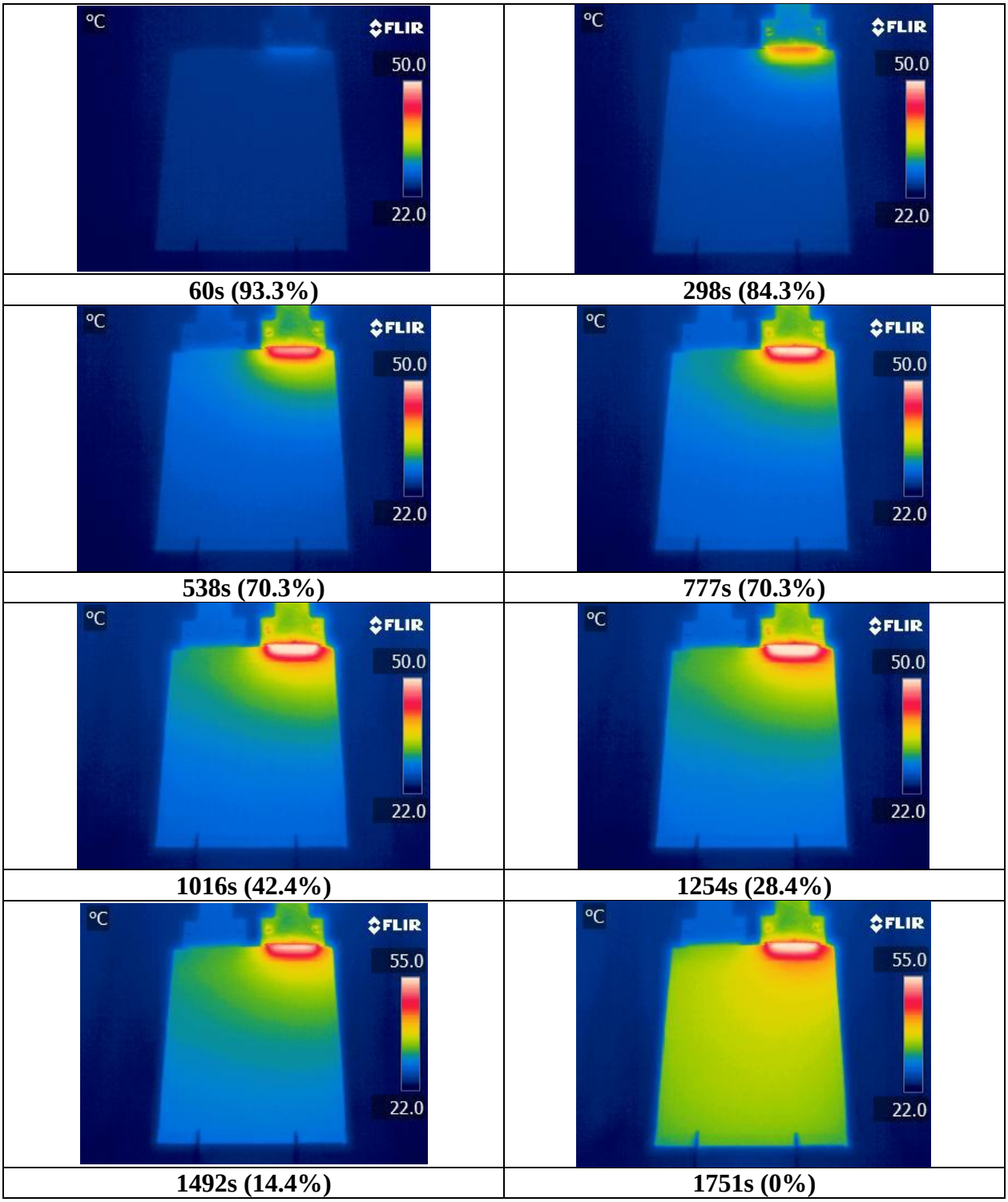

Figure 59 : IR image of 2C discharge with passive cooling. Time after start of discharge and estimated SOC are given below each image

3.4.5 IR Image at 3C Discharge

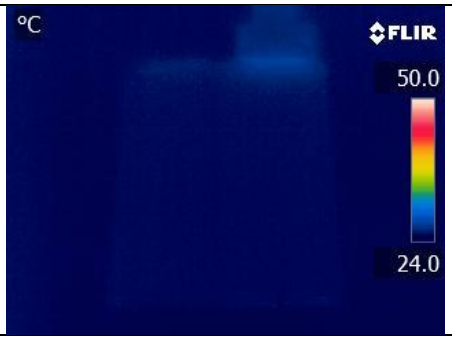	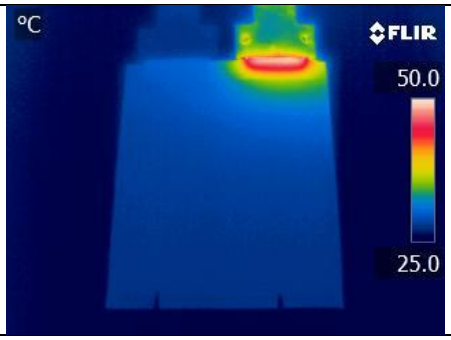
49s (94.9%)	**227s (79.6%)**
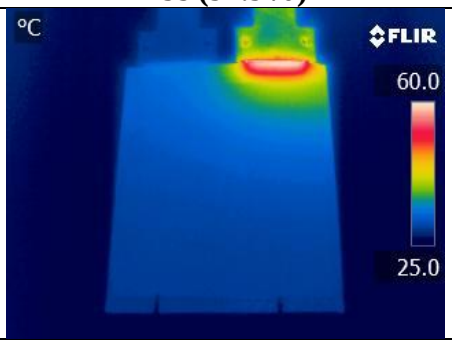	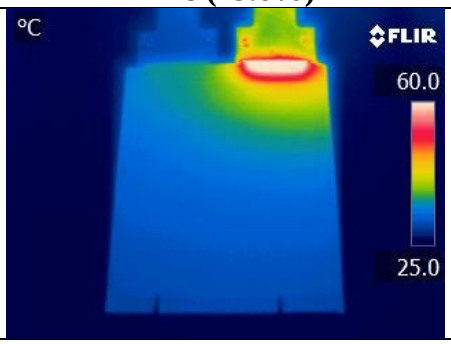
407s (64.4%)	**587s (49.1%)**
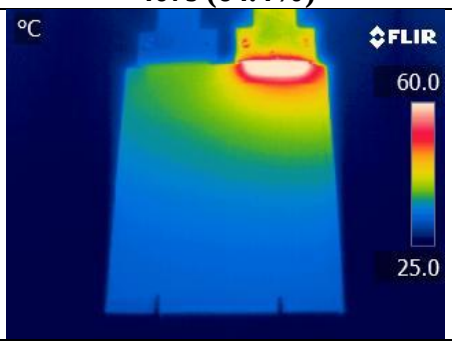	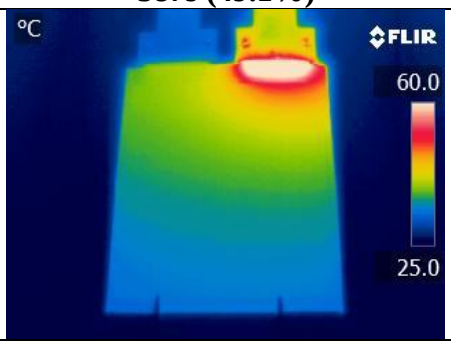
767s (33.8%)	**944s (18.6%)**
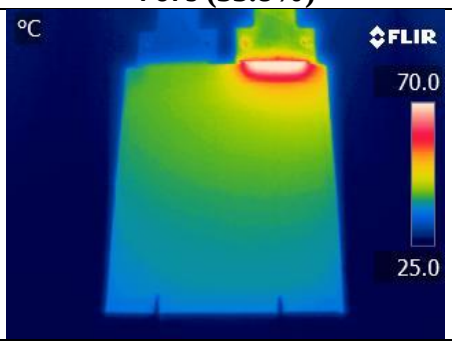	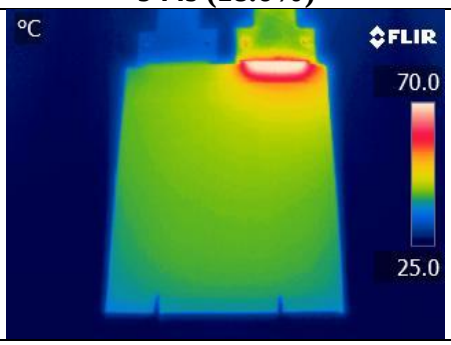
1123s (3.3%)	**1168s (0%)**

Figure 60 : IR image of 3C discharge with passive cooling. Time after start of discharge and estimated SOC are given below each image

3.4.6 IR Image at 4C Discharge

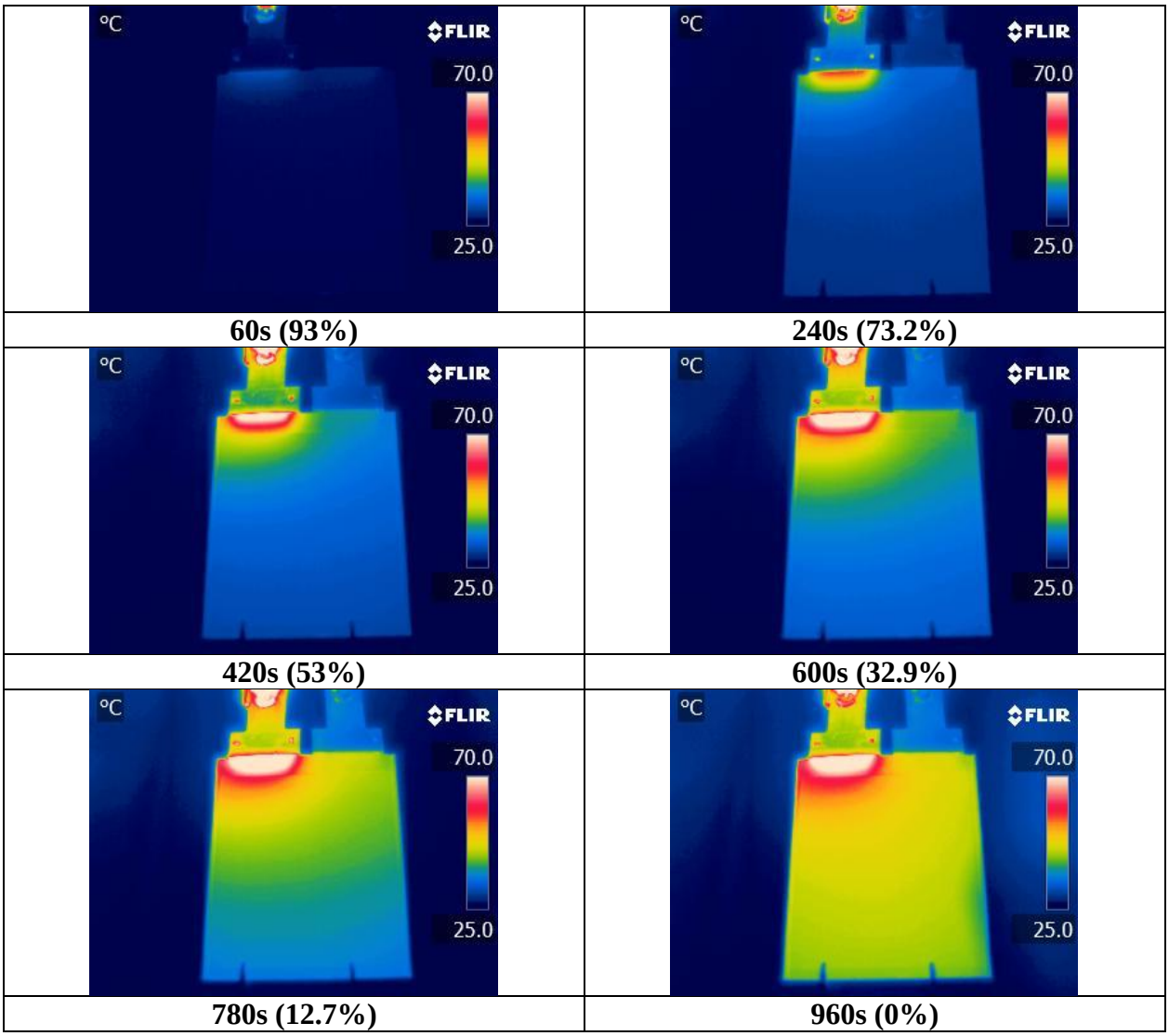

Figure 61 : IR image of 4C discharge with passive cooling. Time after start of discharge and estimated SOC are given below each image

Chapter 4

Part-II: In-Situ Vehicle Data

4.1 Introduction

In 2009, Burlington Hydro launched its GridsmartCity™ initiative as the first step in the evolution toward an intelligent community distribution grid. In support of GridsmartCity™, a Full-electric-converted Ford Escape has been utilized in a productive work environment by Burlington Hydro Co. while its performance, drive cycles, battery parameters and grid impacts being monitored and managed. Complimenting this field test, the University of Waterloo has been developing assessment and management tools to assist with the integration of PHEVs and EVs into the electric grid [118]. Current research is also defined as a part this project. This chapter presents the work done up to now which includes data logger installation, data collection, and analysis of data.

4.2 Vehicle History

The Burlington Hydro electric test vehicle design was modified from the original vehicle. Descriptions of each vehicle and performance specifications are presented in following sections.

4.2.1 The First Burlington Hydro EV (EV-ACX2)

REV delivered an all-electric Ford Escape, named the EV-ACX2, to Burlington Hydro in early 2010, shortly after the beginning of this project. Figure 62 (A), (B), (C), and (D) shows the front view, rear view, passenger cabin, and charge port of the EV-ACX2. Key specifications are provided in Table 21. UW selected, installed, and validated a data logging system for the EV-ACX2 in May 2010. Completing this first step of the project yielded about 6 months of data comprising 126 kilometers of driving. The final report for that year identified that significantly more driving was needed to obtain the necessary data for the remaining modeling tasks. At that time a new vehicle with a new powertrain was also planned to replace the EV-ACX2 for field

trials at Burlington Hydro, and so the data collected from the EV-ACX2 could not be carried forward into future analyses.

(A) Front view of the EV-ACX2

(B) Rear view of the EV-ACX2

(C) Passenger cabin of EV-ACX2

(D) Charge port of EV-ACX2

Figure 62: Front view, rear view, passenger cabin and charge port of the EV-ACX2

Table 21: Key specifications for the EV-ACX2

Specification	Value
Mass (Empty)	1814 kg
Motor Peak Power	90 kW
Motor Peak Efficiency	98% at 4000 RPM
Motor Peak Torque	239 Nm
Battery Module Nominal Voltage	19.2 V
Battery Module Energy Density	89 Wh/kg
Battery Module Nominal Capacity	69 Ah
Total Battery Pack Energy Capacity	25 kWh
Typical Range for Full SOC Swing	100 km
Time 0-100 kilometers per hour (kph)	About 12 seconds

4.2.2 The Second Burlington Hydro EV (EV-ACX 2.5)

An updated version of the REV Ford Escape, the EV-ACX2.5, arrived at Burlington Hydro in June 2011, and was instrumented shortly afterwards by UW. The primary upgrade in the EV-ACX2.5 is a new traction motor/controller combination, a UQM Power Phase 125 kW. REV also did a significant amount of custom control system development for the EV-ACX2.5, and provided a larger set of variables to data log. The EV-ACX 2.5 has the following key performance benefits over the EV-ACX2: 1) Better driving experience, 2) better acceleration, 3) more power, 4) more range, and 5) faster charge time. A vehicle specifications comparison is given in Table 22.

Table 22: Vehicle specification comparison

Specification	EV-ACX 2	EV-ACX2.5
Electric motor type	AC Induction	AC Permanent Magnet
Electric motor power (kW)	90	125
Torque (Nm)	239	300
Range (km)	80	Up to 140
Charge time (hr)	5	3.89
Transmission	Single speed gearbox	Single speed gearbox with electronic park lock

4.3 Charge Management System

The data management system consists of a data logger installed in the EV-ACX2.5, a cellular network connection for data collection, and processing scripts that convert the logged data into monthly usage reports. This system is automated and provides Burlington Hydro employees with the ability to monitor vehicle and grid electricity use. Burlington Hydro can then evaluate the performance of the EV as a fleet vehicle, the grid energy impacts, and opportunities to optimize vehicle operation (e.g. charging times).

4.3.1 Data Logging Installation in Three Different Vehicles

Currently three ISAAC data loggers have been installed in three different Ford Escape vehicles at Burlington Hydro, one in the EV-ACX2.5 (Figure 63) and two in Ford Escape hybrid electric fleet vehicles owned by Burlington Hydro's (Figure 64 and Figure 65). These two HEVs provide baseline HEV performance to compare the electric vehicle performance data collected via the installed data loggers.

Figure 63: First data logger installed in EV-ACX 2.5

Figure 64: Second data logger in HEV #3

Figure 65: Third data logger in HEV #4

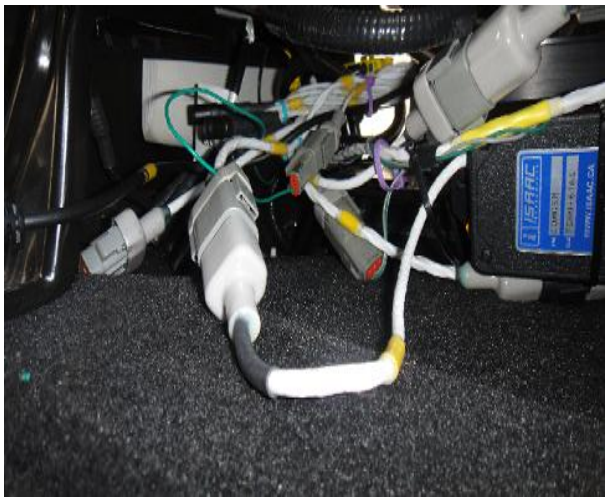

Figure 66: Data recorder unit

Figure 67: Data logger connection and shut down wire

The data recording unit (DRU) and modem are located beneath the front passenger seat. The cellular antenna that enables wireless data transmission is located on top of the vehicle. The data logger is powered by the on-board 12V battery. A local company in Waterloo, Ontario, Cross Chasm Technologies collects all of the logged vehicle data on its server. Figure 66 shows the DRU installed beneath the passenger seat and Figure 67 shows the data logger connection and shut down wire in vehicle. There are three battery packs of Lithium-ion battery installed on the vehicle, including a total of 20 battery modules in series. Figure 68 shows a schematic of the battery packs locations in the vehicle. Each module contains 6 series x 49 parallel IFR 18650 Cylindrical Valence Cells i.e. each battery module includes 6 strings of battery cells in series and each string contains 49 cells in parallel resulting in a total of 294 cells in each battery module. Hence, in total there are 5880 cells (294 cells x 20 modules) in this vehicle. The data logger unit records battery, powertrain, and GPS data. The data channels of interest in this work are listed in Table 23.

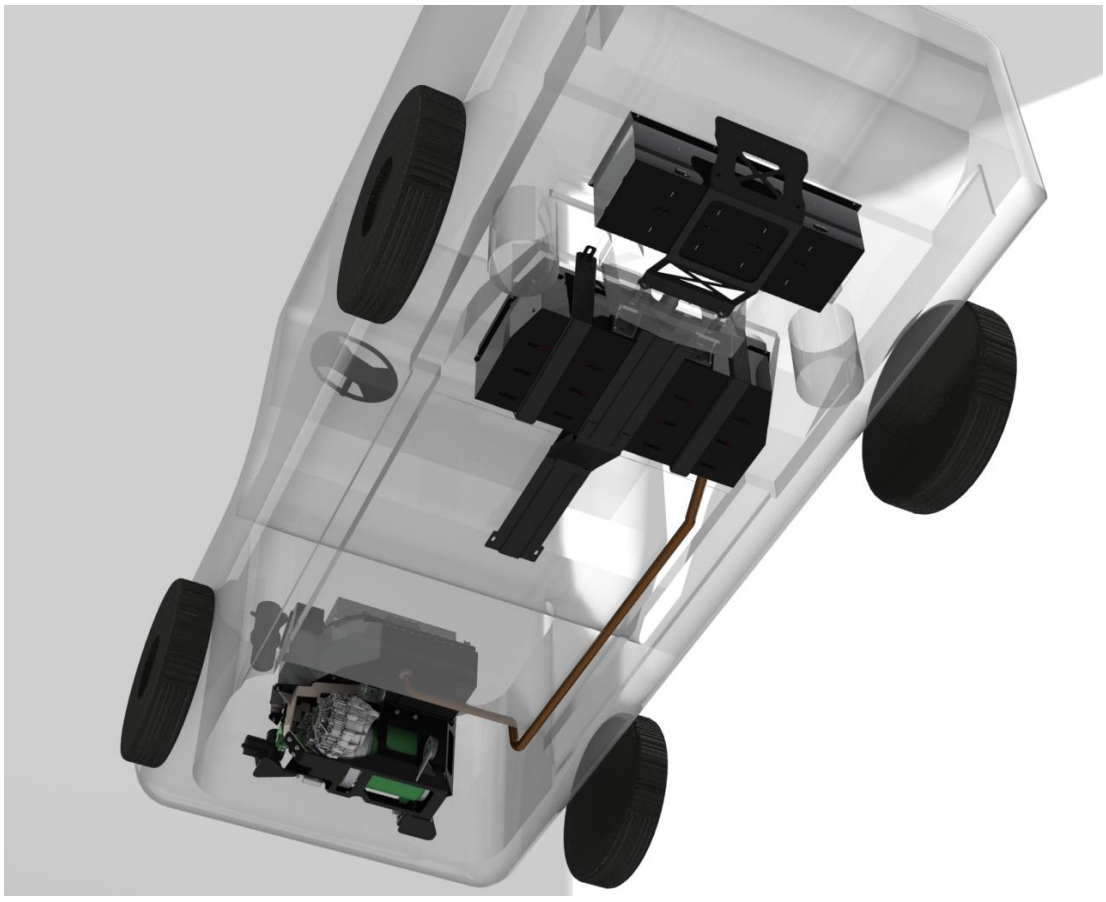

Figure 68 : CAD of vehicle underside showing integration of multiple battery packs [119]

Table 23: Data logging signals

Signal	Reason Required
Battery Voltage	Monitor vehicle energy use and regenerative braking
Battery Current	Monitor vehicle energy use and regenerative braking
Module-1 to Module-20 Temp.	High temperatures are known to enhance degradation
Module-1 to Module-20 SOC	Very high and very low SOCs are known to enhance degradation
Motor Voltage	Monitor powertrain energy use
Motor Current	Monitor powertrain energy use
Motor Speed / Vehicle Speed	Monitor vehicle performance
Motor Torque	Monitor vehicle performance
Vehicle Acceleration	Monitor vehicle performance
Accelerator Pedal Position	Monitor driver demands
Brake Pedal Position	Monitor driver demands

The ability to monitor drive cycles, vehicle charging profiles, and vehicle charging locations enables Burlington Hydro to implement a charging/grid management program. Ideally this will consist of a database that records where the vehicle drives during the day, where it charges, and how much electrical energy from the grid is needed to support the vehicle in its daily activity. As such, battery current and voltage data as well as GPS data of driving behavior must be collected.

4.4 EV-ACX2.5 Sample Report

In this section, an individual EV-ACX2.5 report is presented. This event includes both highway and in-city driving comprises the longest individual drive cycle performed with the vehicle in terms of distance travelled (106 km). The trip characteristics are summarized in Table 24.

Figure 69 shows the relevant drive cycle this trip. The vehicle was driven for 2 hours and 16 minutes with a battery state-of-charge range is 100% to 2%.The peak speed was observed to be 125 km/h while the average speed was 46.9 km/h. During this trip the outside temperature was 5 ^{0}C. The vehicle is capable of achieving a standard Urban Dynamometer Driving Schedule (UDDS) cycle, meeting peak accelerations for the representative city cycle. With an average energy efficiency of 270 Wh/km, and a 25 kWh battery, the vehicle range in Burlington Hydro fleet driving is roughly 106 km, which is in line with REV's claims. This energy efficiency is significantly affected by the allowable battery depth of discharge and temperature. More on-road

data will permit more detailed analyses of the vehicle's performance under a range of driving conditions.

Table 24 : Longest recorded drive cycle details

Specification	Value	
Trip Duration	136	(min)
Trip Distance	106	(km)
Starting SOC	100	(%)
Ending SOC	2	(%)
Total Energy	-23.68	(kWh)
Cycle Average Speed	46.92	(kW/h)
Cycle Peak Speed	125	(kW/h)
Average Positive Acceleration	0.59	(m/s^2)
Peak Positive Acceleration	3.43	(m/s^2)
Trip Cost (at $ 0.11/kWh)	2.60	(CAD)
Cost per Km (at $0.11/kWh)	0.024	(CAD/km)
Outside Temperature	+5	(˚C)

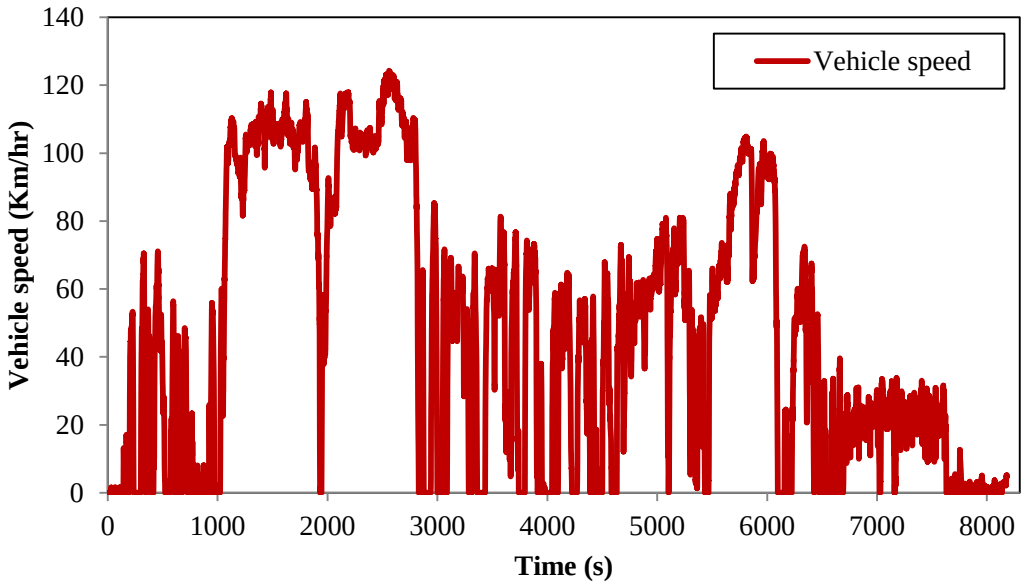

Figure 69 : Vehicle speed versus time for longest recorded trip with EV-ACX2.5

Figure 70 depicts the battery voltage and current profile for the 106 km trip as a function of time. The minimum value of battery voltage is 350 V and maximum value is 414 V which is the initial voltage of the battery. The maximum current drawn from the battery was 196 Amps, while the

maximum current applied to the pack by the regenerative processes was 195 Amps. These values correspond to a maximum power draw of 43.88 kW and a power input of 68.25 kW

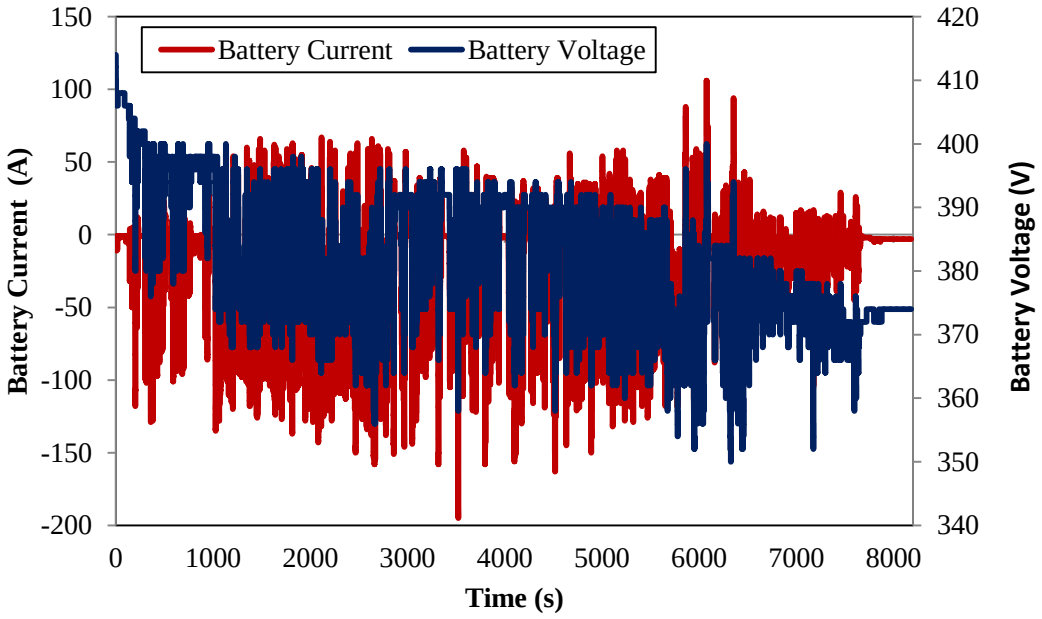

Figure 70 : Battery voltage and current profile for longest recorded trip with EV-ACX2.5

Figure 71 depicts state-of-charge profile for longest recorded trip of 106 km. The EV-ACX 2.5 rarely experiences a low battery SOC like that seen in this trip; the detailed monthly report provided in section 4.5 shows that most of the trips start at 100% SOC and end between 65% SOC to 85% SOC due to driving only in the city. To properly exercise/characterize the battery, larger discharges are required. Based on the observed habits, the project team will advocate for longer drives and less charging between events to exercise the vehicle's battery fully. This will help the team to collect more data to support the continued battery degradation monitoring and modeling.

Figure 71 also depicts the battery maximum and minimum temperature profiles (as measured over all of the battery modules) as a function of time for this trip. It is very well known that the heat generation from a battery is due to resistive (I^2R) losses and the enthalpy changes due to electrochemical reactions during discharge or charge. Heat generation rate from a battery module

depends on several parameters like battery temperature, initial and final state of charge, charge and discharge profile and also on chemistry and construction.

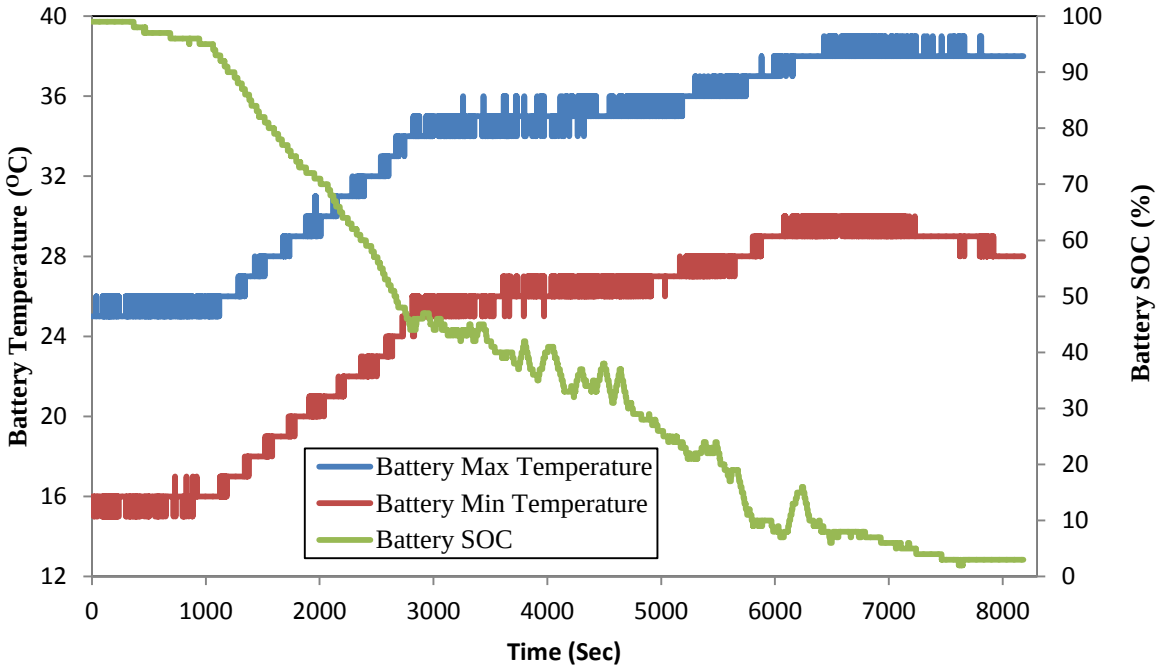

Figure 71 : Battery pack temperature extremes and state-of-charge profile for longest recorded trip with EV-ACX2.5

The EV-ACX2.5 uses 20 passively cooled battery modules located in three packaged locations on the vehicle. It is evident that these different locations are causing significant differences in cell temperature over the drive cycle. These differences may cause differential cell ageing, which can be monitored. It can be seen from Figure 71 that the battery minimum temperature has a minimum value of 15 ^{0}C and a maximum value of 30 ^{0}C, while the battery maximum temperature has a range of 25 ^{0}C to 39 ^{0}C. It can be also observed that there is a drastic change in temperature between 1000 sec to 3000 sec, and this is because of the vehicle was continuous in operation and all three battery packs continuously generate heat. Figure 72 shows temperature profile of all 20 modules. The maximum temperature recorded is 39.27 ^{0}C from Module-6 and minimum temperature recorded is 17.02 ^{0}C from module-18. The average value of all 20 modules is 30.07 ^{0}C.

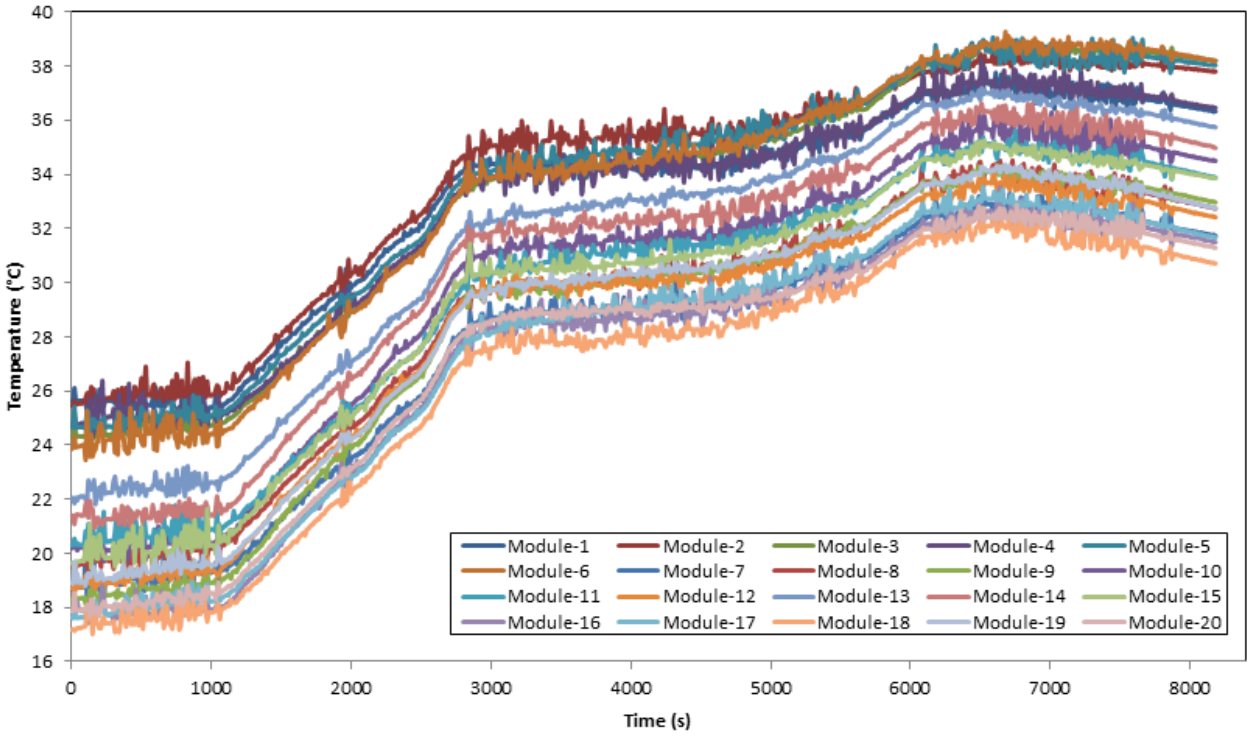

Figure 72 : Module-1 to module-20 temperature profile for longest recorded trip with EV-ACX-2.5

4.4.1 Energy and Cost Analysis of EV-ACX 2.5

Table 25 shows the energy and cost analysis of EV-ACX2.5 for the monthly data collected for five months. It gives a monthly record of the total distance travelled in km by EV-ACX2.5, the energy used during driving in kWh, the cost of driving in dollar, the energy required for charging in kWh, and the charging cost. During its time in Burlington, the EV-ACX2.5 is driven for 792.6 kilometers over five months. The project team needs to have Burlington Hydro dramatically increase EV-ACX2.5 driving to get the battery data for degradation analysis. The total vehicle energy consumption (charging energy) in the last five months is 222.6 kWh and the cost of charging is $24.48.

Table 25 : Energy and cost analysis of EV-ACX 2.5 of last five months

Month	Distance travelled (km)	Driving Energy (kWh)	Driving Cost ($)	Charging Energy (kWh)	Charging Cost (Charging on 220 V)
October	100.8	19.6	$2.156	24.4	$2.684
November	308.2	65.5	$7.205	80.6	$8.866
December	149.3	37.4	$4.114	47.6	$5.236
January	121.0	28.6	$3.146	35.1	$3.861
February	113.3	27.9	$3.069	34.9	$3.839
Total of 5 months	**792.6**	**179**	**$19.69**	**222.6**	**$24.48**

4.5 Detailed Monthly Report for EV-ACX 2.5

In Appendix C detailed monthly vehicle reports for last five months (between October to February) are presented and in this section a detailed monthly report for November month is discussed. The key metrics contained in this report are distance travelled, hours in operation, hours spent charging, total driving and charging energy, time-of-use for vehicle charging, an energy usage path breakdown (from the grid to the powertrain), vehicle energy efficiency plotted against ambient temperature, and a histogram of battery SOC for the start and end of each recorded trip.

The "**Distance**" section shows how many kilometers the vehicle was driven in gasoline mode and electric mode. This is a general report format that can accommodate hybrids, but since the EV-ACX 2.5 is a pure EV, all 308 kilometers are in electric mode.

The "**Time**" section contains a breakdown of the time the vehicle spent ON and OFF. ON is further broken down into driving hours (vehicle is in motion) and idling hours (vehicle is ON but is not in motion). OFF hours are further broken down into charging hours (vehicle is plugged in and battery is charging) and resting hours (vehicle is either plugged in and battery is full, or vehicle is not plugged in).

The "**Driving Energy**" section shows how much energy is being consumed by the vehicle during ON hours. Again, because this is a pure EV there is no gasoline energy consumption. Both

gasoline and electric energy consumption are expressed in Wh/km and Lequivalent/100 km (Le) for easy comparison. Total driving energy for the month, in kWh, is also shown.

The "**Charging Energy**" section provides both the total charging energy used in the month, and a percentage breakdown of how those kWh were obtained. In Ontario's time-of-use (TOU) pricing system electricity charges per kWh vary depending on the time of day and time of year. Prices increase as the time moves from off-peak to mid-peak to on-peak, so it is desirable to plan activities such that the vehicle can be charged off-peak as much as possible. This section also shows the percentage of charging energy obtained from 110V, 220V, and DC quick charge stations. It is important to note that the breakdowns in this section are in kWh (energy), not hours (time).

The "**Energy Path**" section shows where energy is consumed in the vehicle. The charger energy is that energy consumed by the vehicle's on-board charger in converting grid electricity from AC to DC energy that is compatible with the vehicle battery. The powertrain energy is the battery energy consumed by the vehicle to operate. The regenerative energy is the energy recovered by the regenerative braking system, resulting in reduced powertrain energy. All values are given per kilometer travelled for that month.

The "**Temperature**" section plots the vehicle energy consumption in Wh/km against ambient temperature for each recorded trip. This plot is useful for demonstrating the effects of ambient temperature (and the resulting vehicle climate control energy consumption) on energy efficiency.

The "**Battery Charge**" section is a histogram of battery SOC at the start and end of each trip. It provides an at-a-glance view of the typical battery SOC utilization.

4.6 Comparison between EV-ACX 2.5 and HEV

In order to compare the energy consumption and energy cost of EV-ACX 2.5 with that of Burlington Hydro's other fleet vehicles, drive cycles from two of Burlington Hydro's Ford Escape Hybrid (2008 and 2009 model years) fleet vehicles were recorded over four months, between November to February. Table 26 summarizes the monthly distance travel, fuel consumption, and the equivalent energy use in kWh for the HEVs. The equivalence ratio of 9.7 kWh per litter is used for gasoline [120]. It is seen that HEV#4 has the most utilization of the two

HEVs and yields the richest data set. Therefore further analysis was performed based on the HEV#4 recorded data to compare the energy usage and cost with EV-ACX2.5. The results are reported in (Table 27).

Table 26 : Distance travelled and energy consumption by HEV#3 and HEV#4

Month	HEV#3			HEV#4		
	Distance travelled (km)	Fuel (L)	Equivalent Energy (kWh)	Distance (km)	Fuel (L)	Equivalent Energy (kWh)
November	252.8	21.9	212.43	742.9	51.09	495.57
December	-	-	-	793.48	53.15	515.57
January	150	10.2	98.94	1214	80	776
February	104.5682	8.8618	85.95	769.16	50.61	490.917

Table 27 : Energy and cost comparison between EV-ACX 2.5 and HEV#4

Month	HEV#4				EV-ACX 2.5		
	Distance travelled (km)	Fuel used (L)	Equivalent Energy consumption (kWh)	Cost Of driving	Distance travelled (km)	Energy Consumption (kWh)	Cost Of driving
Nov	742.9	51.09	495.57	$54.51	308.2	65.5	$7.205
Dec	793.48	53.15	515.57	$56.71	149.3	37.4	$4.114
Jan	253.53	80	160.923	$17.70	121	28.6	$3.146
Feb	769.16	50.61	490.917	$54	113.3	27.9	$3.069
Total	**3519.54**	**234.85**	**2278**	**$182.92**	**691.8**	**159.4**	**$17.53**
Economy	**0.0512 ($/km)**				**0.025 ($/km)**		

From Table 27, it is observed that the EV-ACX2.5 has travelled a much shorter distance over the last four months as compared to the HEV#4. It is clearly seen that there is a huge difference in energy consumption, distance travelled, and cost of driving. The total fuel consumption over four months of the HEV #4 is 234.85 liters and the equivalent energy consumption is 2278 kWh, while for EV-ACX2.5 the energy consumption is 159.4 kWh. The cost of driving at a rate of 11 cent/KWh for HEV for four months is $182.92 while for EV-ACX2.5 it is $17.53. So the cost per km for HEV#4 is $0.0512 while for EV-ACX2.5 it is only $0.025. Hence, if EV-ACX2.5 is driven for same km as HEV#4 (3519.54 km), the cost of driving is only $87.98, which is much lower than HEV#4 driving cost ($182.92) and there is a saving of $94.94. So it is clear that EV-ACX2.5 is cheaper in operation as compared to HEV.

Chapter 5

Model Development and Validation

The experimental data generated in part-I and II have been validated using a developed battery thermal model. The parameters and design of the model were modified to provide relevant comparison with this work. The methodology used to modify and develop these validations is described in following sections.

5.1 Part-I Model Developement

The first empirical battery thermal model is developed based upon data acquired (time, voltage, current, temperature, and charge/discharge rate) from the thermal boundary condition test apparatus (using dual cold plates for a Li-ion pouch cell). The acquired data is incorporated into a look up table along with simple algorithms written in MATLAB/Simulink to access the look-up table. A Simulink block diagram for battery model is shown in Figure 73 and is adapted from a version created by A Rousseau at Argonne National Laboratory [58].

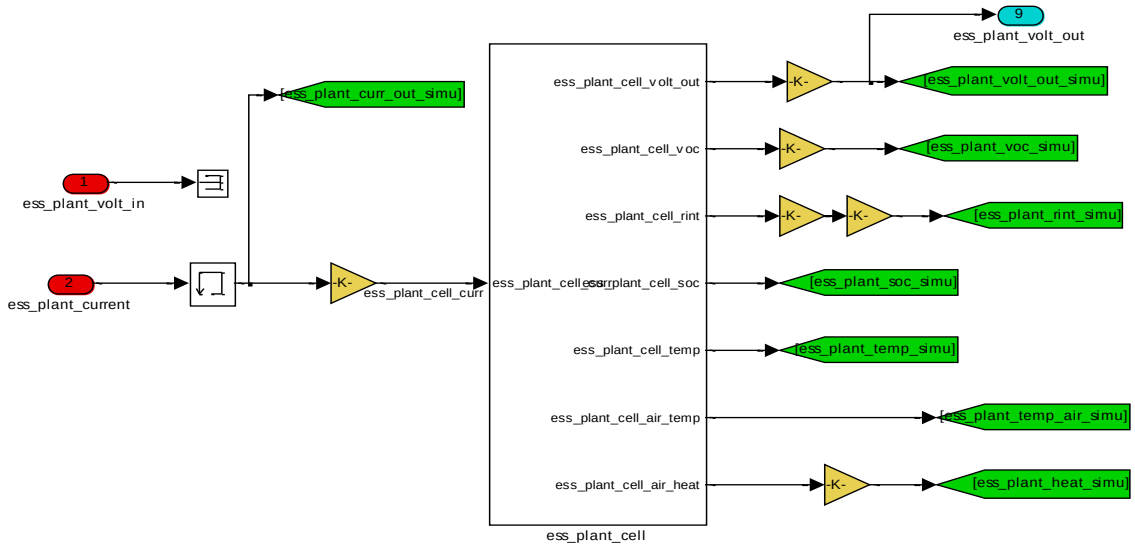

Figure 73 : Simulink block diagram for battery model

The model works by using an input current draw to measure battery voltage which together provides an estimate of the power required from the system. The model is divided into three sections based upon its three primary outputs, SOC, voltage, and temperature. The subsection of the model designed for SOC estimation is shown in Figure 74. As Figure 74 illustrates, cell current and ambient temperature are provided as inputs to the model and SOC estimation is acquired through a simple coulomb-counting procedure. The input current is integrated with respect to time and this charge is added (charging) or subtracted (discharging) from the initial battery capacity to calculate the instantaneous capacity. A look-up table is then use to interpolate the battery's maximum capacity as a function of ambient temperature. The instantaneous capacity is divided by the maximum capacity to achieve the SOC estimate. An initial SOC input provided by the user (ess.plant.init.soc_init in Figure 74) allows a simulation to be conducted beginning with any desired capacity.

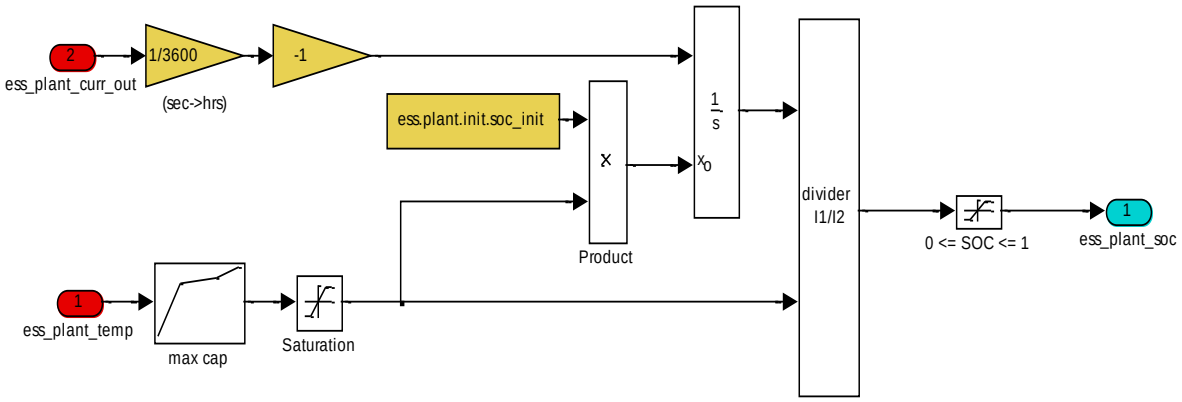

Figure 74 : SOC estimation block for battery model

The second model subsection, voltage estimation, is shown in Figure 75. The inputs to the voltage estimation block are SOC, temperature, and current draw, which are used to determine cell internal resistance, open circuit voltage, and operating voltage.

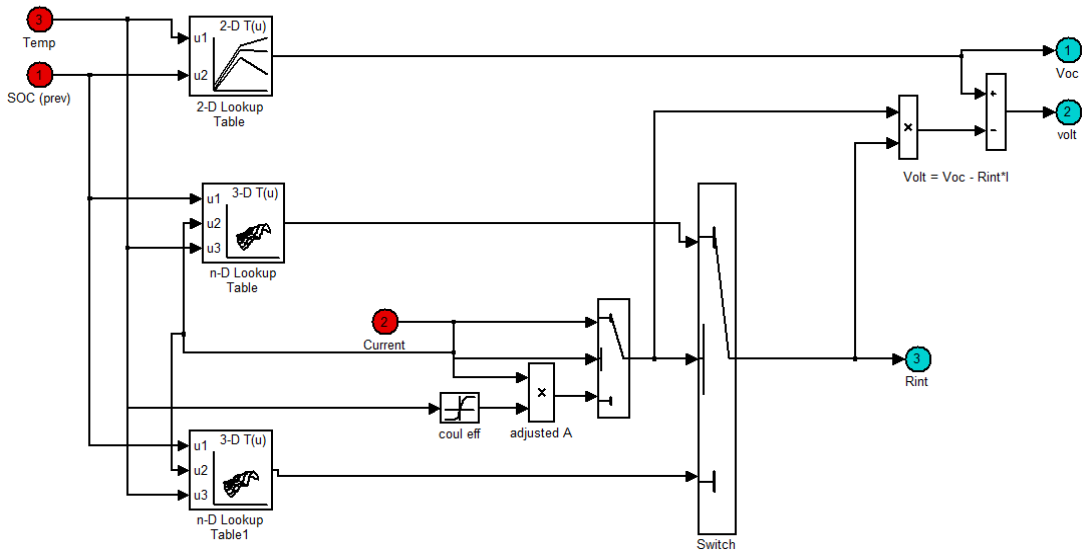

Figure 75 : Voltage estimation block for battery model

The third and final model subsection involves cell temperature estimation and is shown in Figure 76. This temperature estimation block assumes air cooling in to consideration. The heat generated by the cell is calculated using current draw and internal resistance as inputs to simple $Q = I^2R$ calculation. The net heat accumulated in the cell is then calculated and the heat capacity then integrated over time to determine cell temperature. A cell temperature is assumed to be at a uniform temperature.

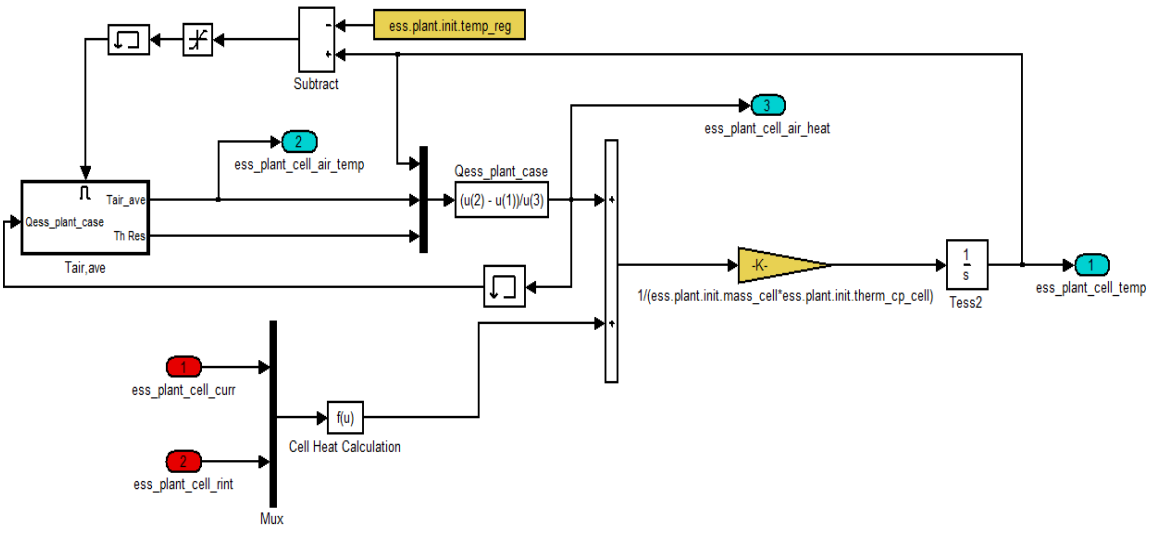

Figure 76 : Cell temperature estimation block of the battery model

5.1.1 Part-I Battery Model Validation

From the thermal boundary condition test apparatus surface temperature, voltage, and SOC data were collected from a Li-ion pouch cell at 1C, 2C, 3C, and 4C discharge cycles and compared to an empirical battery thermal model.

Figure 77 shows a comparison between experimental temperature profile collected from a Li-ion pouch cell at 1C, 2C, 3C, and 4C cycle to the profile predicted by the empirical battery thermal model at an ambient temperature. The model clearly is not able to track the peeks observed in the experimental results and needs to be refined. One important limitation of this model is that it considered only a free convection boundary condition on the battery pouch cell. This work can be extended this model by investigating the impact of a boundary conditions involving a heat exchanger (-45 ^{0}C to +45 ^{0}C).

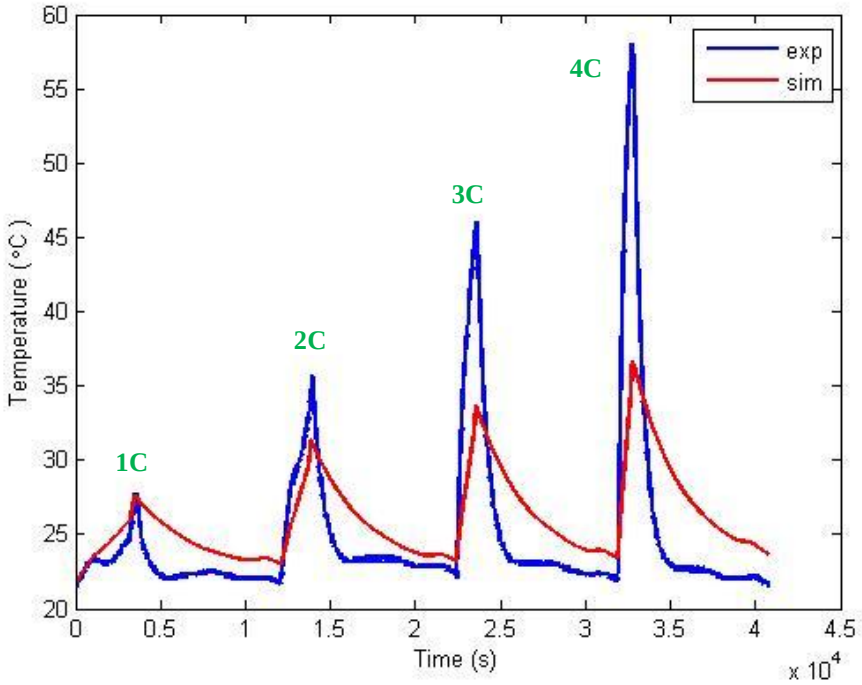

Figure 77 : Comparison of experimental temperature profile from a Li-ion pouch cell at 1C, 2C, 3C, and 4C cycle to the profile predicted by the model

Figure 78 shows a comparison between experimental voltage profile collected from a Li-ion pouch cell at 1C, 2C, 3C, and 4C cycle to the profile predicted by the empirical battery thermal model at an ambient temperature. The voltage data is based on outputs from the model which

utilized resistance values from the Hybrid test stand. This version of the model is obviously lacking as the modeled voltage does not follow the experimental data very well. This is especially true at the edges of the operating range, as the battery approaches the fully charged state at 3.6 V and the fully discharged state at 2.0V. The voltage peaks as the battery charges and discharges are almost non-apparent in the modeled data. Therefore, it is clear that the IR drop or rise across the cell is being significantly underestimated at the terminal low and high values of SOC.

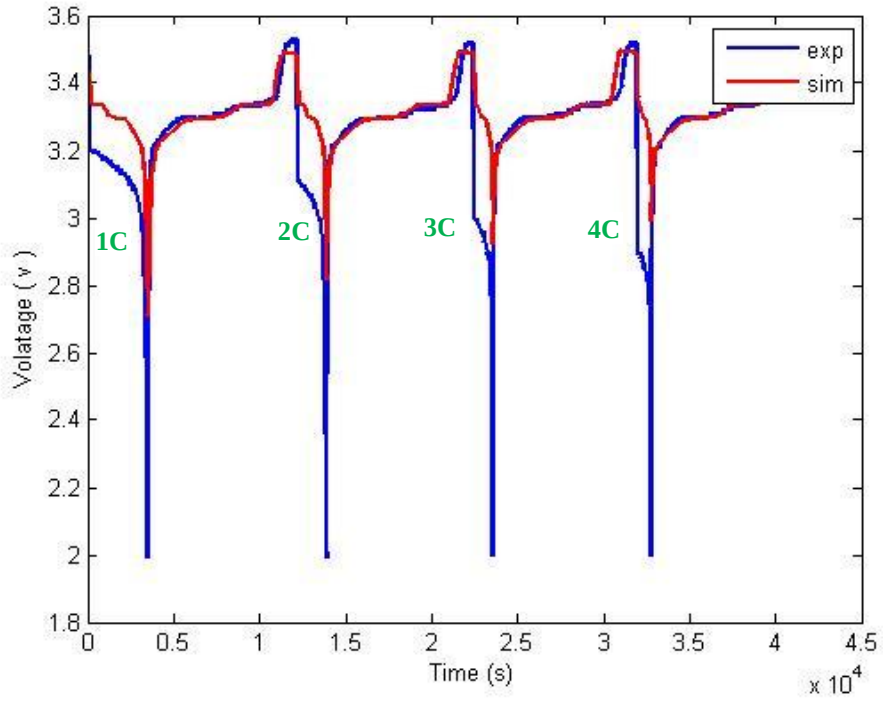

Figure 78 : Comparison of experimental voltage profile from a Li-ion pouch cell at 1C, 2C, 3C, and 4C cycle to the profile predicted by the model

Figure 79 shows a comparison between experimental SOC profile collected from a Li-ion pouch cell at 1C, 2C, 3C, and 4C cycle to the profile predicted by the empirical battery thermal model at an ambient temperature. Model SOC estimation is fairly good; however there are slight discrepancies between the total charge or discharge capacities at various points in the cycle. These differences are minimal and are a result of the simplicity of the model.

The model uses a simple coulomb counting SOC algorithm which takes temperature change into account, but does not consider charge or discharge current. The maximum capacity used for

SOC estimation is the C/5 capacity at a given temperature; it does not take into account that actual capacity will be less as higher charge or discharge currents. This is clear in the data as the estimation of charge capacity is very good for the 1C cycle, but it slightly worse for 3C, and a little bit worse still for 4C. Thus, a more adaptive SOC algorithm that takes current into account would be needed to remove the small discrepancies in SOC estimation as shown below. Also, improving the SOC estimation algorithm could help to remove the remaining voltage estimation issues. With a more accurate representation of the state of charge at the edges of the operating range more accurate voltage predictions could be made in these areas.

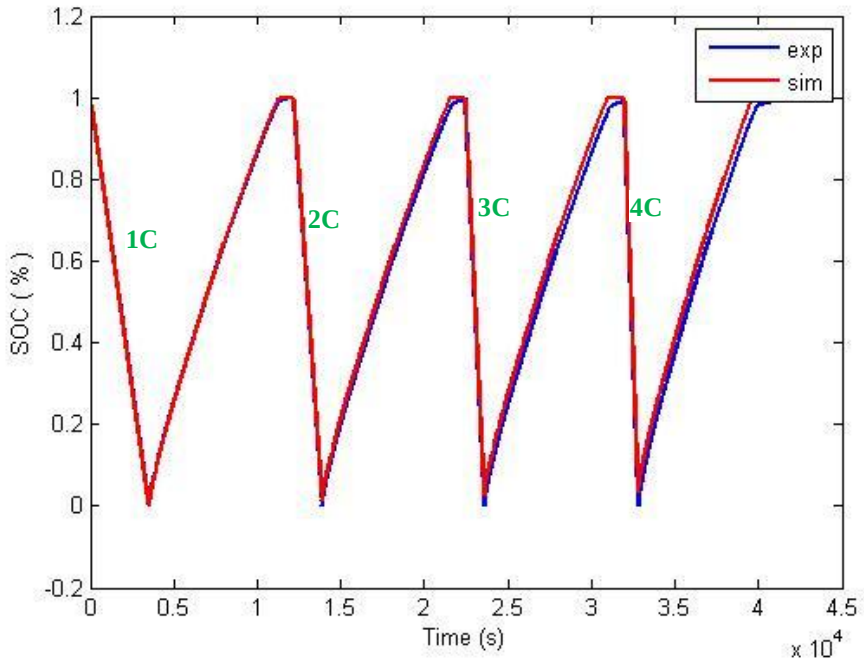

Figure 79 : Comparison of experimental SOC profile from a Li-ion pouch cell at 1C, 2C, 3C, and 4C cycle to the profile predicted by the model

5.2 Part-II Model Development and Validation

From in-situ vehicle data collected, a vehicle drive train model (that can be used to determine vehicle performance) and a second battery thermal model was developed for the converted EVs. The model provides: improved understanding of vehicle operation, insight into how operation can be improved and how operating conditions (e.g. battery temperature) can affect performance of components (e.g. battery degradation).

Determining the relative benefit of an EV, compared to its combustion engine counterpart, is one objective of this work beyond the primary battery management objective of this project. The vehicle drive train model was developed using PSAT/Autonomie software. PSAT is a powerful modeling tool for analyzing hybrid electric vehicle (HEV) systems and was developed by Argonne National Laboratory and sponsored by the U.S. Department of Energy (DOE) [58]. It allows users to realistically evaluate vehicle performance, fuel consumption and exhaust emissions for several driving cycles. One of the most important characteristics of PSAT is that it is a forward-looking model – it simulates a vehicle system from the driver to the wheels, with realistic control commands.

The main steps undertaken to develop the vehicle drive train model including the battery thermal sub-model are as follows:

1) The individual models components were developed using appropriate technical specifications for the Burlington Hydro EV.
2) The components were combined to represent the vehicle architecture.
3) Real-world driving cycle data was recorded using the Burlington Hydro EV.
4) Real-world driving cycles were then executed with the vehicle model.
5) Model components were refined using real-world data.

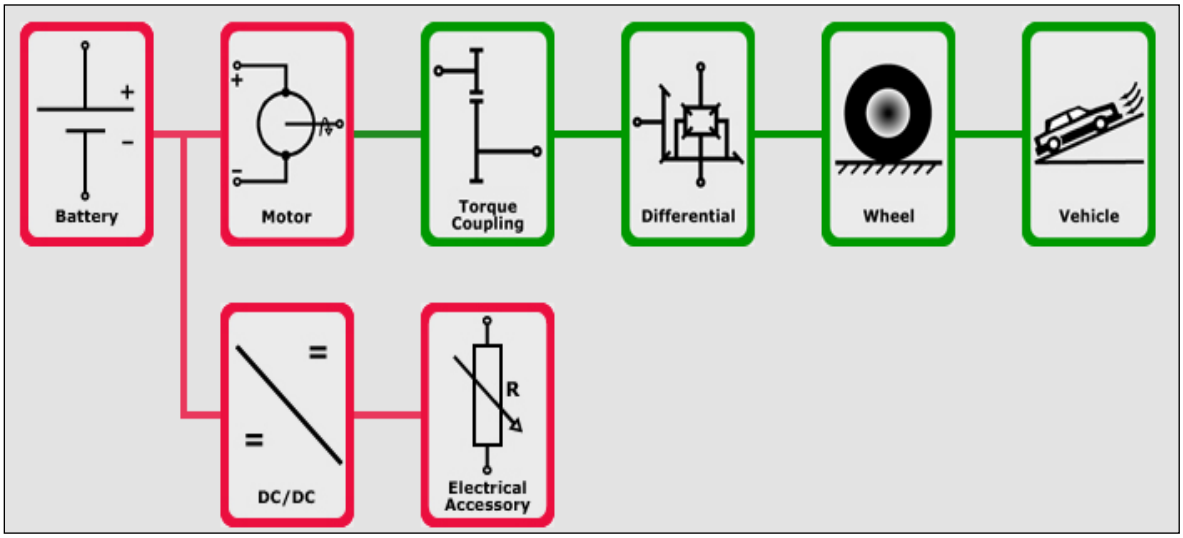

Figure 80 : Burlington hydro electric vehicle drivetrain components in PSAT

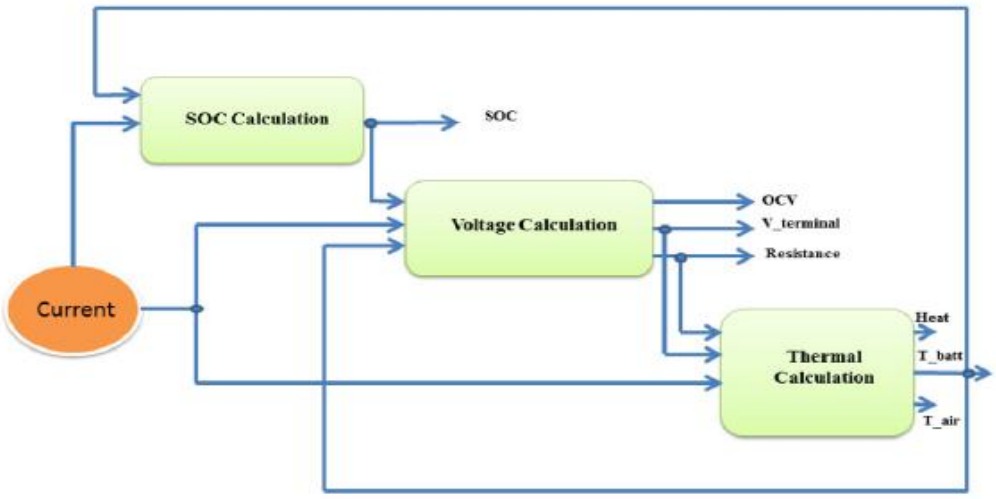

Figure 81 : Battery model in PSAT

The main components of the electric vehicle drivetrain model are the battery and electric motor components and are shown in Figure 80. The battery model in PSAT is shown in Figure 81. To ensure the model is able to predict the real-world vehicle behaviour, performance of these two components must be compared with real-world data. To validate a component model, data measured at the input of the component are fed directly into the component model and the simulated output is compared with the measured output. Validation of the powertrain model involved executing several of the drive cycles with equivalent initial conditions was performed with the EV. The results are then compared with the simulated results.

The signals from the data logger as listed in Table 23 are then used to construct refined component initialization files in PSAT. The key elements of this exercise were:

1) Refine the electric motor operation map, which determines the speed/torque, current/voltage, and efficiency characteristics of the simulated electric motor.
2) Refine the battery charge/discharge maps, which determine the current/voltage characteristics of the battery.
3) Refine the vehicle dynamics model, which determines the simulated forces acting on the vehicle during operation over a range of speeds.
4) Determine the typical electrical accessory power losses within the vehicle, which affect energy efficiency by drawing energy from the battery that is in excess of that required by the powertrain (i.e. electric motor).

In the first step, the data set was analyzed to derive the battery open circuit voltage plot, battery internal resistance plot (for both charging and discharging) and electric motor efficiency. In addition, based on the torque vs. speed plot of the electric motor which was derived from the test data, the braking control strategy was modified in order to match the regenerative braking profile The model was then run with the longest (106 km) drive cycle, and a comparison was made between the net battery energy consumption of the simulated vehicle and the actual Burlington Hydro EV.

Figure 82 shows the SOC curve for the longest recorded trip (106 km). The model results give good agreement when compared with the experimental curve. The general profiles of each curve match, with some discrepancies in the in-city portion of the SOC curve (3000s to 8000s). The model results show smooth changes in SOC whereas the real-wold data incorporates more sudden and large changes in SOC during the in-city portion. This is related to the regenerative control strategies which require greater refinement to capture these sudden SOC changes.

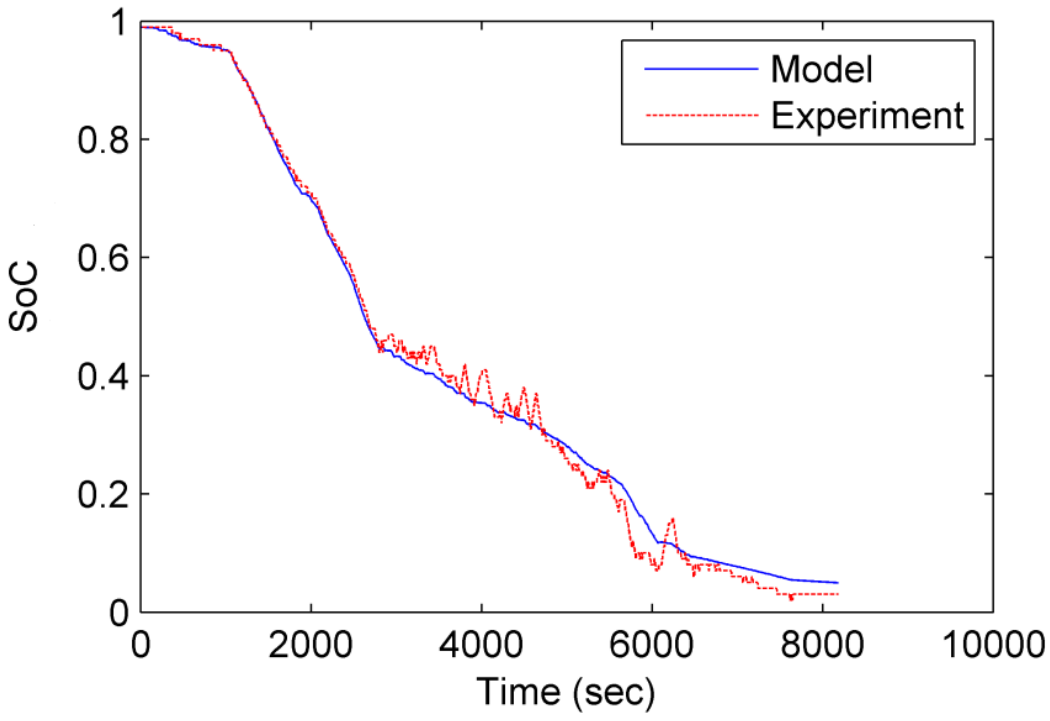

Figure 82 : SOC versus time curve for longest drive cycle

5.3 Comparison of Part-I and Part-II

In additional thermal discharge testing, a prismatic Li-ion pouch cell was tested in lab with the thermal boundary condition test apparatus using the longest recorded drive cycle (106 km) of Burlington Hydro Ford Escape EV-ACX-2.5 as the cycle current profile. The temperature parameters were measured. The test bench was then run with the longest (106 km) drive cycle, and a comparison was made between the experimental values collected from prismatic Li-ion pouch cell with the actual vehicle drive cycle. In order to do this experiment, the first step is to scale down all 20-modules (or 3-battery packs) of EV-ACX 2.5 which contains total 5880 Valence 18650 Li-ion cell to 20 Ah prismatic Li-ion pouch cell.

Figure 83 shows the comparison between the experimental power output profiles from a prismatic Li-ion cell to the profile based on real drive cycle collected from Burlington Hydro EV-ACX2.5. It is clear that both profiles are matching and there are slight discrepancies between each.

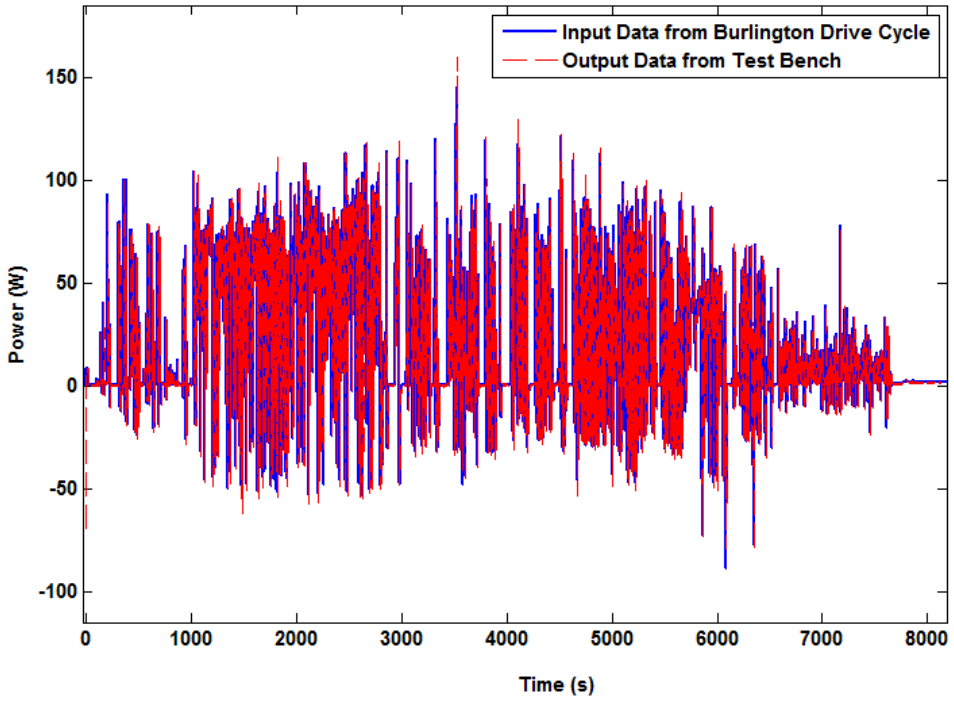

Figure 83 : Comparison of power output between real drive cycle and test bench

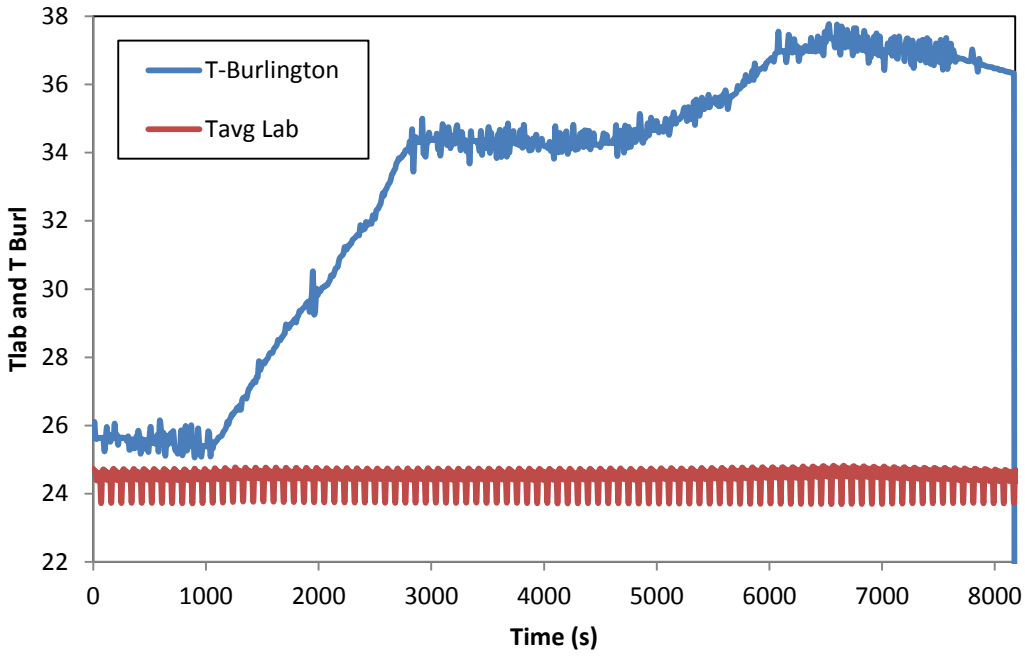

Figure 84 : Experimental and real drive cycle temperature profile

Figure 84 shows the temperature profile obtained from the experimental data and real-world drive cycle. The average battery surface temperature profile from experiment is almost constant near the ambient laboratory temperature while the temperature profile obtained from the real drive cycle is much higher, and does not follow the same trend. This was expected because of three main reasons: 1) the free convection from air in the laboratory has higher heat transfer rate than the battery installation in the Burlington EV module allows, 2) the ambient temperature in the lab was 22 ^{0}C, while the real drive cycle was tested in an ambient temperature of 5 ^{0}C. 3) the Burlington EV has a thermal controller which activates fans automatically and is designed to maintain pack temperature below 38 ^{0}C regardless of ambient temperature.

Chapter 6

Conclusions and Recommendations

6.1 Conclusions

In order to fulfill the objectives and experimental milestones mentioned in section 1.5., an apparatus called “the thermal boundary condition test apparatus using dual cold plates for Li-ion pouch cell with indirect liquid cooling” was designed and built. The thermal behaviour in terms of the surface temperature distribution, heat flux, and heat generation from Li-ion pouch cell for PHEV, HEV and EV applications was studied in a lab. Thermal images of the same battery were also collected at various discharge rates of 2C, 3C, and 4C with IR camera.

The following observations can be made:

6.1.1 From Thermal Characterization Lithium-ion battery:

1) Discharges were performed on the battery both within and outside the apparatus and numerous electro-thermal data sets were created. Varying the operating temperature and discharge rate showed that the amount of heat generated and thus the rate of heat generation of prismatic Li-ion cell increased with the discharge rate, and decrease with operating temperature. Battery discharge time and capacity were shown to increase when the discharge rate was decreased and the operating temperature was increased.
2) Measurements of temperature were performed at ten locations on the battery surface and it was clearly shown that heat generation or heat accumulation was not uniform across the principal surface of the battery. Specifically, the thermocouples mounted nearest to the electrodes sensed temperature increases that were larger than at other locations. Measurements of heat flux near the electrodes confirm the high value of heat flux in that area (as high as 3112.2 W/m^2).

3) From the thermal boundary condition test apparatus, surface temperature, voltage, and SOC data were collected for a prismatic pouch cell at 1C, 2C, 3C, and 4C discharge cycles and compared to an empirical battery thermal model. The result showed that the thermal model was not able to accurately track the peaks observed in the experimental results and therefore requires refinement. Since the model only represents a free convection boundary condition on the battery pouch cell, the model should be extended by introducing the impact of boundary conditions incorporating a heat exchanger in contact with battery surfaces.

6.1.2 From IR image experiment:

1) Discharges were performed at 2C, 3C and 4C rates while the thermo-graphic camera produced images of the battery surface. As a result, the non-uniformity of temperature was visually observed. Temperature non-uniformity is in an indication of heat generation non-uniformity on a surface and as such it can be concluded that the area of highest temperature and non-uniformity is the location where heat generation is largest. For the prismatic pouch cell discharged, the area of maximum heat generation appears to be at the external tab to current collector interface along the top edge of the battery.

6.1.3 From Burlington EV data:

1) In-situ vehicle data collection and thermal characterization of vehicle batteries under realistic drive cycles was performed with data collected from three data loggers installed on three different Burlington Hydro vehicles (one EV, and two HEVs). Monthly reports were generated for the EV to enable Burlington Hydro to track the vehicle's travel distance, energy consumption, efficiency, and charging time. From the data analysis it is clear that compared to the baseline hybrid, the EV-ACX 2.5 is much more affordable to operate, based purely on energy consumption. The systems installed in the vehicles and the data collection infrastructure remains in place to provide insight and benefit to Burlington Hydro planners.
2) A PSAT/Autonomie model was developed based on real-world drive cycles and was validated with the collected data. The data was generated for fellow researchers investigating battery degradation electrochemical modeling. The developed model is able

to realistically simulate the experimental SOC curve. There are some discrepancies in the in-city portion of the SOC curve, which are related to the regenerative control strategies.

3) The collected real-world drive cycles were also performed with the thermal boundary condition test apparatus while electrical and thermal data was collected from a prismatic Li-ion pouch cell. The temperature profile was compared between the experimental data and the real-world drive cycle from the Burlington EV. The average battery surface temperature profile from the lab experiment was almost constant near the ambient laboratory temperature while the temperature profile obtained from the real drive cycle was much higher, and did not follow the same trend. This was due to three reasons:
    i. Free convection from air in the laboratory has a higher heat transfer rate than the battery position in the Burlington EV module allows.
    ii. The ambient temperature in the lab was 22 ^{0}C, while the real drive cycle was tested in an ambient temperature of 5 °C.
    iii. The Burlington EV has a thermal controller that activates fans to maintain pack temperature below 38 ^{0}C regardless of ambient temperature.

6.2 Recommendations

Several recommendations arise from this study:

1) The battery test bench should be thermally isolated. The temperature of the battery during cycling is largely influenced by the ambient temperature of the room. Since both the capacity of the battery and the degradation rate are functions of temperature, the results obtained from the test stand contain a great deal of noise due to the fluctuations in ambient temperature. These fluctuations are caused by the cycle of day and night and by day-to-day changes in temperature. In order to eliminate this noise and obtain more accurate results, the stand should be properly insulated to ensure that temperature fluctuations are only caused by the heat generated during charging/discharging of the battery.
2) More thermal testing of the batteries should be carried out with bath temperatures between -45 ^{0}C to 45 ^{0}C, with different cooling fluid, and with different SOC ranges in order to obtain more thermal data in terms of surface temperature distribution, heat flux, and heat generation from various batteries with different chemistries.
3) The number of heat flux sensors should be increased to cover the entire battery surface. This will enable accurate measurement of the heat flux distribution on the battery.
4) Different cold plate designs with different cooling flow channel patterns, inlet/outlet conditions, SOC ranges, and fluids could be investigated as potential thermal management systems. Further testing using such systems will enable the effectiveness of possible thermal management systems, to be compared.
5) Two or more pouch cells could be connected in series or parallel, and testing should be done under different conditions.
6) Changes in battery design could result in reduced non-uniformity in heat generation and decreased temperature, e.g. move external current tabs to opposite ends of the battery.

6.3 Summary of Contributions

The contributions of the proposed research can be summarized as follows:

1) The thermal behavior of a Lithium-ion battery pouch cell under a wide range of charge/discharge rates, and different initial, ambient, and boundary conditions was characterized. Charge and discharge rates used included those typical of vehicle batteries, initial and ambient temperature from 5 ^{0}C to 35 ^{0}C, and boundary conditions from free convective cooling and contacting cooling plates. Characterization was through 2-D temperature profiles, temperature change rates, and local and total heat flux. This information will be useful to electrochemistry battery modellers, and an example of this use was demonstrated by the development of an empirical battery thermal model for degradation studies and battery management system development.
2) For the in-situ vehicle data collection portion of this research, three data loggers were installed in three different vehicles to evaluate usage and performance of an electric vehicle. Statistical analysis was performed on recorded data from the vehicles (total distance travelled, energy consumption, efficiency, and charging times in five months and compared with other two fleet vehicles). During the five months of analyzed operation, the EV-AXC2.5 travelled 792.6 kms and used 222.6 kWh of grid electricity. The difference in operating cost in terms of energy consumption and energy cost was evaluated for the HEVs and EV. This information was helpful for development of the empirical model in PSAT/Autonomie for vehicle performance and battery modeling.
3) An empirical battery thermal model was developed based on data acquired from the thermal boundary condition test apparatus using dual cold plates for a Lithium-ion pouch cell. The acquired data was utilized into a look up table along with simple algorithms written in MATLAB/Simulink to develop the empirical model.
4) For vehicle battery modeling, PSAT/Autonomie software developed by Argonne National Laboratory was used. In addition, the collected data from the vehicles as well as room thermal boundary condition test apparatus will also be provided for the validation of electrochemistry based battery thermal models.

Chapter 7

Experimental Uncertainty

In this section, the uncertainty analysis of the experimental measurements and derived correlations is presented. The accuracy of measurement equipment is determined and used to establish the uncertainty of calculated relationships and properties.

7.1 Method

The overall uncertainty of the experimental results and theoretical predictions will be calculated using the method described by Moffat in [121]. In this method, the result R of an experiment is determined from a set of measurements as in (34).

$$R = R(X_1, X_2, X_3, \dots, X_N) \tag{34}$$

Each measurement can be represented as $X_i \pm \delta X_i$where $\delta X_i$is the uncertainty. The effect of each measurement error on the calculated result is determined as in (35):

$$\delta R_{X_i} = \frac{\delta R}{\delta X_i}\delta X_i \tag{35}$$

So the overall uncertainty of the result is determined using (36):

$$\delta R = \left\{\sum_{i=1}^{N}\left(\frac{\delta R}{\delta X_i}\delta X_i\right)^2\right\}^{1/2} \tag{36}$$

If R is described by an equation of the form $R = X_1^a X_2^b X_3^c \cdots\cdots X_N^m$ then the overall uncertainty of the result can be determined directly from the set of individual measurement uncertainties as in (37).

$$\frac{\delta R}{R} = \left\{\left(a\frac{\delta X_1}{X_1}\right)^2 + \left(b\frac{\delta X_2}{X_1}\right)^2 + \cdots + \left(m\frac{\delta X_N}{X_1}\right)^2\right\}^{1/2} \tag{37}$$

7.2 Temperature and Heat generation Uncertainty

In this, the total heat generated by the cell is determined along with temperature and heat flux at various locations of the battery surface. The range of uncertainties determined using the following analysis is organized into a summary Table 30.

7.2.1 Average Temperature Measurement Uncertainty

The average battery surface temperature was evaluated using Equation (38).

$$T_{\substack{surface \\ average}} = \frac{\sum(T_{ij}A_{ij})}{A_{total}} \tag{38}$$

Evaluating uncertainty of surface temperature measurements and the of area measurements was required to determine the overall uncertainty of the average surface temperature measurement. The uncertainties are as follows:

a) Surface Temperature, T_{ij}

Surface temperature measurements were made with T-type SLE (special limits of error) thermocouples and recorded with a Keithley 2700 data acquisition system. The uncertainty due to the thermocouple readout is 1°C, according to manufacturer's specifications [122]. The uncertainty is shown as Equation (39).

$$\frac{\delta T}{T} = \pm\frac{1°C}{T[°C]} \tag{39}$$

b) Area, A_{ij}

An electronic digital caliper with a resolution of 0.005 was used to measure the positions of the thermocouples as installed on the battery surface. As $A_{ij} = lw$, Equation (40) was used to determine the uncertainty in each area.

$$\frac{\delta A}{A} = \pm\left\{\left(\frac{\delta l}{l}\right)^2 + \left(\frac{\delta w}{w}\right)^2\right\}^{1/2} \tag{40}$$

For the purpose of evaluating uncertainty in the average surface temperature, let $P_{i,j}$ represent the individual $T_{ij}A_{ij}/A_{total}$ components of the surface temperature average, where i and j subscripts

describe the particular thermocouple. Equation (41) was used to determine the error in each $P_{i,j}$ product.

$$\frac{\delta P_{i,j}}{P_{i,j}} = \pm\left\{\left(\frac{\delta T_{ij}}{T_{ij}}\right)^2 + \left(\frac{\delta A_{ij}}{A_{ij}}\right)^2 + \left(\frac{\delta A_{total}}{A_{total}}\right)^2\right\}^{1/2} \quad (41)$$

A relative uncertainty for the average surface temperature was established via equation (42). The highest surface temperature absolute error occurs when the surface temperature is smallest. The range of relative uncertainty is large and thus was calculated for each operating temperature. These values are summarized in. These values are summarized in Table 28.

$$\frac{\delta T_{\substack{surface \\ average}}}{T_{\substack{surface \\ average}}} = \pm\left\{\left(\frac{\delta P_{1,1}}{P_{1,1}}\right)^2 + \left(\frac{\delta P_{1,2}}{P_{1,2}}\right)^2 + \cdots + \left(\frac{\delta P_{5,1}}{P_{5,1}}\right)^2\right\}^{1/2} \quad (42)$$

Table 28 : Average uncertainty in surface temperature for five operating temperatures

Operating Temperature [°C]	± Relative Uncertainty (%)	± Absolute Uncertainty [°C]
5	20.3	1.5
15	2.6	0.5
22	1.1	0.4
25	1.2	0.4
35	0.7	0.3

7.2.2 Heat Generation Uncertainty

The uncertainty in total heat generated is made up of the uncertainties of the components that calculate the heat. It is calculated using Equation (43). The uncertainties that make up Equation (43) are presented in following subsections.

$$\frac{\delta Q_{gen}}{Q_{gen}} = \pm\left\{\left(\frac{\delta Q_{sensible}}{Q_{sensible}}\right)^2 + \left(\frac{\delta Q_{cooling}}{Q_{cooling}}\right)^2 + \left(\frac{\delta Q_{environment}}{Q_{environment}}\right)^2\right\}^{1/2} \quad (43)$$

The uncertainty in the rate of total heat generation is calculated using Equation (44).

$$\frac{\delta \dot{Q}_{gen}}{\dot{Q}_{gen}} = \pm\left\{\left(\frac{\delta \dot{Q}_{sensible}}{\dot{Q}_{sensible}}\right)^2 + \left(\frac{\delta \dot{Q}_{cooling}}{\dot{Q}_{cooling}}\right)^2 + \left(\frac{\delta \dot{Q}_{environment}}{\dot{Q}_{environment}}\right)^2\right\}^{1/2} \quad (44)$$

7.2.2.1 Sensible Heat Uncertainty

The sensible heat calculation is based on the mass of the battery, battery specific heat capacity and average surface temperature. The battery mass and specific heat capacity were reported by the manufacturer and assumed to have no uncertainty. Thus the uncertainty in sensible heat is as shown in Equation (45).

$$\frac{\delta Q_{sensible}}{Q_{sensible}} = \pm\frac{\delta \Delta T_{s,avg}}{\Delta T_{s,avg}} \quad (45)$$

The uncertainty in the rate of sensible heat accumulation is calculated using Equation (46).

$$\frac{\delta \dot{Q}_{sensible}}{\dot{Q}_{sensible}} = \pm\left\{\left(\frac{\delta \Delta T_{s,avg}}{\Delta T_{s,avg}}\right)^2 + \left(\frac{\delta \Delta \mathrm{t}_{discharge}}{\Delta \mathrm{t}_{discharge}}\right)^2\right\}^{1/2} \quad (46)$$

a) Surface Temperature Difference Uncertainty

The relative uncertainty in surface temperature difference is largest when the temperature difference is smallest. Equation (47) was used to calculate the uncertainty in average surface temperature differences.

$$\frac{\delta \Delta T_{s,avg}}{\Delta T_{s,avg}} = \pm\left\{\left(\frac{\delta T_{s,avg}}{T_{s,avg}}\right)^2 + \left(\frac{\delta T_{s,avg}}{T_{s,avg}}\right)^2\right\}^{1/2} \quad (47)$$

b) Discharge Time

Discharge time was calculated based on the output from the Labview controlled charge/discharge bench. The uncertainty is taken to be equal to the resolution of the time measurement, and is therefore taken to be 1 second. The largest uncertainty occurs during the shortest discharge and is determined using Equation (48). The largest uncertainty will be carried through to simplify further calculations.

$$\frac{\delta \Delta \mathrm{t}_{discharge}}{\Delta \mathrm{t}_{discharge}} = \pm\frac{1\ sec}{\Delta \mathrm{t}_{discharge}} \quad (48)$$

7.2.2.2 Heat Removed Uncertainty (Cooling plate)

The cooling heat energy calculation is based on the mass flow rate of the cooling fluid, the coolant specific heat capacity and temperature difference of the coolant between the inlet and outlet of the cooling plates. The uncertainty in coolant flow rate is assumed to be negligible and the uncertainty in cooling heat energy is determined using (49).

$$\frac{\delta Q_{cooling}}{Q_{cooling}} = \pm\left\{\left(\frac{\delta\dot{m}}{\dot{m}}\right)^2 + \left(\frac{\delta\Delta T}{\Delta T}\right)^2 + \left(\frac{\delta\Delta \mathrm{t}_{discharge}}{\Delta \mathrm{t}_{discharge}}\right)^2\right\}^{1/2} \tag{49}$$

The uncertainty in the rate of sensible heat accumulation is calculated using Equation (50).

$$\frac{\delta\dot{Q}_{cooling}}{\dot{Q}_{cooling}} = \pm\left\{\left(\frac{\delta\dot{m}}{\dot{m}}\right)^2 + \left(\frac{\delta\Delta T_w}{\Delta T_w}\right)^2\right\}^{1/2} \tag{50}$$

a) Flow rate Uncertainty

The volumetric flow rate of the cooling fluid was measured with a Microtherm FS1 30-300 mL/min flow meters. Specifications provided by the manufacturer list instrument uncertainty at 6% of full scale error, which is ± 18 mL/min. This uncertainty is equivalent to Equation (51). The highest relative uncertainty will be carried through to simplify further calculations.

$$\frac{\delta\dot{m}}{\dot{m}} = \pm\frac{18\ mL/min}{\dot{m}\ [mL/min]} \tag{51}$$

b) Fluid Temperature Difference

The uncertainty associated with the difference in temperature between the inlet and outlet of the cooling plates was determined using Equation (52). The uncertainty in the temperature measurement at each inlet or outlet is equivalent to the uncertainty previously given as Equation (39). The highest relative uncertainty will be carried through to simplify further calculations.

$$\frac{\delta\Delta T_w}{\Delta T_w} = \pm\left\{\left(\frac{1\ ℃}{T_{w,i}[℃]}\right)^2 + \left(\frac{1\ ℃}{T_{w,o}[℃]}\right)^2\right\}^{1/2} \tag{52}$$

c) Discharge Time

This uncertainty is equal to that given in Equation (48).

7.2.2.3 Environment Heat Uncertainty

The method of determining the environment heat effect is equivalent to the method used to determine heat removed by the cooling plate. As such, the uncertainty associated with environmental heat gain is equivalent to the uncertainty in heat removed by the cooling plates.

7.2.2.4 Natural Convection Cooling

The cooling heat calculation when natural convection cooling was used is based on correlations for the heat transfer coefficient based on the Rayleigh and Nusselt number. The uncertainty in convection cooling heat was determined using (53).

$$\frac{\delta Q_{conv}}{Q_{conv}} = \pm\left\{\left(\frac{\delta h_c}{h_c}\right)^2 + \left(\frac{\delta A_b}{A_b}\right)^2 + \left(\frac{\delta \Delta T_{s,\infty}}{\Delta T}\right)^2 + \left(\frac{\delta \Delta t_{discharge}}{\Delta t_{discharge}}\right)^2\right\}^{1/2} \quad (53)$$

The uncertainty in the rate of convection cooling heat removal is calculated using Equation (54).

$$\frac{\delta \dot{Q}_{conv}}{\dot{Q}_{conv}} = \pm\left\{\left(\frac{\delta h_c}{h_c}\right)^2 + \left(\frac{\delta A_b}{A_b}\right)^2 + \left(\frac{\delta \Delta T_{s,\infty}}{\Delta T_{s,\infty}}\right)^2\right\}^{1/2} \quad (54)$$

a) Heat Transfer Coefficient Uncertainty

The uncertainty in the heat transfer coefficient was determined using Equation (55). The uncertainty in the thermal conductivity of the air was not included as the effect is considered negligible.

$$\frac{\delta h_c}{h_c} = \pm\left\{\left(\frac{\delta Nu_L}{Nu_L}\right)^2 + \left(\frac{\delta L}{L}\right)^2\right\}^{1/2} \quad (55)$$

b) Rayleigh number

The uncertainty in the Rayleigh number was calculated with Equation (56). The uncertainty in the thermo-physical properties of the air were excluded from the calculation as the values were taken from widely available sources and were dynamically

defined based on the film temperature for each time step of data. As such the contribution to overall uncertainty in Rayleigh number was assumed to be negligible.

$$\frac{\delta Ra_L}{Ra_L} = \pm\left\{\left(\frac{\delta\beta}{\beta}\right)^2 + \left(\frac{\delta A_b}{A_b}\right)^2 + \left(3\frac{\delta L}{L}\right)^2 + \left(\frac{\delta\Delta T_{s,\infty}}{\Delta T_{s,\infty}}\right)^2\right\}^{1/2} \quad (56)$$

Table 29 : Average uncertainties that give rise to uncertainty in Rayleigh number

Variable	Absolute Uncertainty (%)
$\Delta T_{s,\infty}$	1.78
L	0.24
A_b	0.4
β	1.1

c) Nusselt Number

The uncertainty in the Nusselt number correlation is equivalent to the uncertainty in the Rayleigh number as in Equation (57). The uncertainty in Prandtl number has been ignored based on the justification described in the preceding Rayleigh number uncertainty.

$$\frac{\delta Nu_L}{Nu_L} = \pm(1/4)\frac{\delta Ra_L}{Ra_L} \quad (57)$$

7.2.2.5 Heat Flux Uncertainty

The heat flux at locations was determined from the product of voltage readings made with the Keithley hardware and the reported sensitivity of the sensor (HFS). The uncertainty in the HFS voltage readings based on the Keithley specifications in the range of 100 mV is:

$$\frac{\delta V_{HFS}}{V_{HFS}} = \pm\left(3.0 \times 10^{-5} + \frac{3.5 \times 10^{-6}}{V_{HFS}\,[V]}\right) \quad (58)$$

The maximum uncertainty in HFS readings will occur during the maximum voltage measurement. The uncertainty in an HFS reading is thus:

$$\delta q_{HFS} = S * \delta V_{HFS} \quad (59)$$

Table 30 : Summary of uncertainty

Variable	Range	Temperature [°C]	± Relative Uncertainty (%)
$T_{i,j}$[°C]	5.6 °C – 47 °C	–	2.1% - 17.8%
$T_{\substack{surface \\ average}}$[°C]	5.6 °C – 44.5 °C	–	0.48 % - 28.5%
$Q_{sensible}$ [J]	1817 J - 29554 J	5	28.7 %
		15	3.68 %
		22	1.56 %
		25	1.70 %
		35	1.00 %
$\dot{Q}_{sensible}$ [W]	0.52 W – 24.06 W	5	28.7 %
		15	3.68 %
		22	1.56 %
		25	1.70 %
		35	1.00 %
$\dot{m}$ [mL/min]	170 mL/min – 218 mL/min	–	8.3% - 10.6%
ΔT_w[°C]	0.1 °C – 2.6 °C	–	0 % – 21.9%
$Q_{cooling}$ [J]	5992 J – 11162 J	–	24.4 %
$\dot{Q}_{cooling}$ [W]	2.9 W – 50.6 W	–	24.4 %
$Q_{environment}$ [J]	3382.5 J – 66991 J	–	24.4 %
$\dot{Q}_{environment}$[W]	4.12 W – 21.61 W	–	24.4 %
Q_{conv} [J]	3228 J – 4240 J	–	0.56 %
$\dot{Q}_{conv}$ [W]	0.95 W – 4.50 W	–	0.58 %
Q_{gen} [J]	8090 J – 41345 J	5	44.9 %
		15	34.7 %
		22	24.4 %
		25	34.5 %
		35	34.5 %
$\dot{Q}_{gen}$ [W]	2.319 W – 58.56 W	5	44.9 %
		15	34.7 %
		22	24.4 %
		25	34.5 %
		35	34.5 %
q_{HFS}[W/m^2]	0 W/m^2 - 4994 W/m^2	–	0% - 0.04%

References

[1] Natural Resources Canada's Office of Energy Efficiency, "2007 Canadian Vehicle Survey Summary Report," Natural Resources Canada, Ottawa, 2009.

[2] Environment Canada, "National Inventory Report 1990-2012 - Greenhouse Gas Sources and Sinks in Canada," Environment Canada, Gatineau, 1910-7064, 2012.

[3] “Hybrids/Green Car”. Hybrid cars and more/Green Car. Demand Media Inc., Sept-2009. Available: http://www.greencar.com/tech-hybrids.php

[4] H. T. K. Yeow, M. Thelliez, and E. Tan, "Thermal Analysis of a Li-ion Battery System with Indirect Liquid Cooling Using Finite Element Analysis Approach", SAE Int. J. Alt. Power. 1(1):65-78, 2012, doi:10.4271/2012-01-0331.."

[5] S. Peck. M. Pierce, "Developement of a Temperature -Dependent Li-ion Battery Thermal Model, ThermoAnalytics Inc., SAE International, 10.4271/2012-01-0117."

[6] "Rank, A., et al., What are Plug-In Hybrids? Team Fate (University of California, Davis) Retrieved August 7, 2007; earlier version."

[7] A. Simpson, "Cost-Benefit Analysis of Plug-in Hybrid Electric Vehicle Technology" National Renewable Energy Laboratory conference report CP-540-40485 accessed January 7, 2009.

[8] U. Eberle, R.V.Helmolt "Sustainable transportation based on electric vehicle concepts: a brief overview". Royal Society of Chemistry. Retrieved 2010-06-08."

[9] “Electric Cars for 2010 I Clean Fleet Report.” Optimark Inc., Apr.2010. Available: http://www.cleanfleetreport.com/electric-vehicles/electric-car-for-2010/

[10] “History of Electric Vehicles". Inventors. New York Times Company, Jan.2010. Available: http://inventors.about.com/library/weekly/aacarselectrica.htm

[11] “The technology in Hybrid Vehicles.”Hybrid Vehicle-Hybrid Cars and Trucks,Fuel Cell,Clean Fuel’s.Oct.2005. Available: http://www.hybrid-vehicle.org/hybrid-vehicle-technology.html

[12] Didik Frank. "How to built an electric car" Jan.2002, http://www.didik.com/ev_build.htm

[13] Hans Greimel. Automotive News. [Online]. http://www.autonews.com/Accessed date : April 12, 2012

[14] S. Matthewson, S. Panchal, R. Fraser, M. Fowler, R. Culham, "Thermal Management of a Li-ion Cell with Indirect Liquid Cooling Method Using Dual Cold Plates Approach,SAE 2013 Thermal Management Systems Symposium, October 22-24, 2013,Troy, MI,USA."

[15] P. Ramadass, B. Haran, R. White, and B. N. Popov. (2008) " Capacity fade of Sony 18650 cells cycled at elevated temperatures: Part I. Cycling performance" J. Power Sources, Vol. 112, pp 606-613. Accessed 27 Oct 2011.Available: http://www.sciencedirect.com./lib.uwaterloo.ca/science/article/pii/S0378775302004743

[16] R. Spotnitz and J. Franklin. (2008) "Abuse Behaviour of High Power Lithium-Ion Cells" J. Power Sources, Vol. 113, pp 81-87 Accessed 27 Oct 2011. . Available: http://www.sciencedirect.com./lib/uwaterloo.ca/science/article/pii/S0378775302004883

[17] M. Genovese. "Empirical Performance Model for Lithium Ion Battery", CHE 499 : Independent Research Project, Chemical Engineering department, University Of Waterloo, April, 2012.

[18] J. Lo. Effect of Temperature on Lithium-Ion Phosphate Battery Performance and Plug-in Hybrid Electric Vehicle range" MA.Sc thesis,University of Waterloo,2013.

[19] B. B. Li-ion battery for smart phones. http://www.batterybuyer.com/

[20] "The Freedonia Group, World Batteries - Industry Study with Forecasts to 2015 & 2019, 2010."

[21] F. Sullivan, "Frost & Sullivan Projects Explosive Growth for Lithium-ion Batteries in Electric Vehicle and Hybrid Electric Vehicle Segments, 2010."

[22] B. M. Kopf, F. R. Kalhammer, D.H. Swan, V.P. Roan, and M.P. Walsh, "Status and prospects for zero emissions vehicle technology," 2007.

[23] Battery University (23 July 2011). Types of Lithium-ion. Available: http://batteryuniversity.com/learn/article/types_of_lithium_ion

[24] B. Kampman. H. V. Essen. G. Duleep, and Max Grünig. "Impacts of Electric Vehicles - Deliverable 2 Assessment of electric vehicle and battery technology," 11.4058.04, 2011.

[25] D. Hull,"Electric cars race towards a better battery" July,2011, http://chicagotribune.com.

[26] P. Axmann, M. Wohlfahrt-Mehrens, "Electrochemical energy storage systems for car applications," Pres. HySA Systems Business Seminar, November 2009.

[27] P. N. Deutsche Bank; R. Lache, D. Galves, G. Toulemonde, J. Gehrke, K. Sanger, V. ha, S. Rao, and J. Crane, "Electric Cars: Plugged In. Batteries must be included," June2008.

[28] R. Thomas, L. David, "Handbook of Batteries, 3rd editon.: McGraw-Hill, 2001.

[29] P. Arora, Z. Zhang, "Battery Separators," Chem. Rev, vol. 104, pp. 4419-4468, 2004.

[30] M. Brain. "How Lithium-ion Batteries Work" http:// http://electronics.howstuffworks.com/

[31] J. Cho et al. "Comparison of Al_2O_3- and $AlPO_4$-coated $LiCoO_2$ cathode materials for a Li-ion cell," Journal of Power Sources, vol. 146, pp. 58-64, 2005, Selected papers pressented at the 12th International Meeting on Lithium Batteries.

[32] Jeffrey W. Fergus. "Recent developments in cathode materials for lithium ion batteries," Journal of Power Sources, vol. 195, pp. 939-954, 2010.

[33] B. Xia. H. Cao, Y. Zhang, and N. Xu,. "$LiAlO_2$-coated $LiCoO_2$ as cathode material for lithium ion batteries," Solid State Ionics, vol. 176, pp. 911-914, 2005.

[34] A. F. Hollenkamp. A. P. Lewandowski, S.W. Donne, and A.S. Best,. "Cycling and rate performance of Li-$LiFePO_4$ cells in mixed FSI-TFSI room temperature ionic liquids," Journal of Power Sources, vol. 195, pp. 2029-2035, 2010.

[35] G. X. Wang. S. A. Needham, H. K. Liu, V. A. Drozd, and R. S. Liu,. "Synthesis and electrochemical performance of doped $LiCoO_2$ materials," Journal of Power Sources, vol. 174, pp. 828-831, 2007, 13th International Meeting on Lithium Batteries.

[36] J. Park, S.Lee, et al. "Effect of conducting additives on the properties of composite cathodes for lithium-ion batteries," Journal of Solid State Electrochemistry, vol. 14, no. 4, pp. 593-597, 2010, 10.1007/s10008-009-0814-5.

[37] H. Xiangming et al. "Preparation of co-doped spherical spinel $LiMn_2O_4$ cathode materials for Li-ion batteries," Journal of Power Sources, vol. 150, pp. 216-222, 2005.

[38] J.P.Tu, Y.Z.Yang, and W.K.Zhang,. "Spray-drying technology for the synthesis of nanosized $LiMn_2O_4$ cathode material," Materials Letters, vol. 61, pp. 864-867, 2007.

[39] Hyun-Wook Lee et al. "Ultrathin Spinel $LiMn_2O_4$ Nanowires as High Power Cathode Materials for Li-Ion Batteries," Nano Letters, vol. 10, pp. 3852-3856, 2010.

[40] L. C. Yang Shao-Horn, C. Delmas, E. Chris Nelson, and Michael A. O'Keefe,. "Atomic resolution of lithium ions in $LiCoO_2$," Nat Mater, vol. 2, pp. 464-467, 2003.

[41] C.M. Julien. "Local structure of lithiated manganese oxides," Solid State Ionics, vol. 177, pp. 11-19, 2006.

[42] J. T. Bloking. S.Y. Chung, and Y.M. Chiang,. "Electronically conductive phospho-olivines as lithium storage electrodes," Nature Materials, vol. 1, pp. 123-128, 2002.

[43] Fernanda F. C. Bazito and Roberto M. Torresi. "Cathodes for lithium ion batteries: the benefits of using nanostructured materials," Journal of the Brazilian Chemical Society, vol. 17, pp. 627-642, 2006.

[44] Han Chen et al. "Preparation and electrochemical performance of $LiFePO_4$/C composite with network connections of nano-carbon wires," Materials Letters, vol. 65, pp. 559-561, 2011.

[45] Lin Zou et al. "Investigations on the modified natural graphite as anode materials in lithium ion battery," Journal of Physics and Chemistry of Solids, vol. 69, pp. 1265-1271, 2007.

[46] Ralph J Brodd and Akiya Kozawa. Lithium-Ion Batteries: Science and Technologies. New York, USA: Springer, 2009.

[47] B. Gao et al. "Enhanced saturation lithium composition in ball-milled single-walled carbon nanotubes," Chemical Physics Letters, vol. 327, pp. 69-75, 2000.

[48] Ali Reza Kamali and Derek J. Fray, "Review on Carbon and Silicon Based Materials as Anode Materials for Lithium Ion Batteries," Journal of New Materials for Electrochemical Systems, vol. 13, pp. 147-160, 2010.

[49] S. S. Zhang. "A review on the separators of liquid electrolyte Li-ion batteries," Journal of Power Sources, vol. 164, no. 1, pp. 351-364, 2007.

[50] J. Dahn and G. M. Ehrlich, "Lithium-Ion Batteries," in Linden's Handbook of Batteries", New York, McGraw Hill, 2011, pp. 26.1-26.79.

[51] Y. Sasaki. S.T. Myung, S. Sakurada, Y.K. Sun and H. Yashiro,"Electrochemical behavior of current collectors for lithium batteries in non-aqueous alkyl carbonate solution and surface analysis by ToF-SIMS," Electrochimica Acta, vol. 55, no. 1, pp. 288-297, 2009.

[52] H. Liao. Y. Wang, J. Wang, X. Qian, Y. Zhu and S. Cheng, "Effects of Current Collectors on Electrochemical Performance of FeS_2 for Li-ion Battery," Journal of Electrochemical Science, vol. 8, pp. 4002-4009, 2013.

[53] Q. Sa and Y. Wang, "Ni foam as the current collector for high capacity C–Si composite electrode," Journal of Power Sources, vol. 208, pp. 46-51, 2012.

[54] Doron Aurbach et al. "Design of electrolyte solutions for Li and Li-ion batteries: a review," Electrochimica Acta, vol. 50, pp. 247-254, 2004, Polymer Batteries and Fuel Cells:Selection of Papers from First International Conference.

[55] George E. Blomgren, "Liquid electrolytes for lithium and lithium-ion batteries," Journal of Power Sources, vol. 119-121, pp. 326-329, 2003, Selected papers presented at the 11th International Meeting on Lithium Batteries.

[56] S. S. Zhang. "A review on electrolyte additives for lithium-ion batteries," Journal of Power Sources, vol. 162, pp. 1379-1394, 2006, Special issue including selected papers from the International Power Sources Symposium 2005 together with regular papers.

[57] K. Bullis, "Why Chrysler Chose A123 Batteries," MIT Technology Review, 10 April 2006 [Online]. Available: http://www.technologyreview.com/video/412970/why-chrysler-chose-a123-batteries [Accessed 24 September 2013].

[58] Fleets and Fuels.com, "A123 Lithium Packs for New Geely Plug-in" Available:http://www.fleetsandfuels.com/fuels/evs/2012/03/a123-lithium-packs-for-new-geely-plug-in/. [Accessed 24 September 2013].

[59] W. Tahil, "How much lithium does a LiIon EV battery really need?" Meridian International Research, March 2010.

[60] V. V. Viswanathan, W. Xu, S. Towne, R. E. Williford, J. G. Zhang, J. Liu, and Z. Yang, "Effect of entropy change of lithium intercalation in cathodes and anodes on Li-ion battery thermal management," J. Power Sources, vol. 195, no. 11, pp. 3720-3729, 2010.

[61] O. Komesker, O. Obeidi, H. G. Schweiger, A. Raschke, M. Schiemann, C. Zehner, M. Gehnen, M. Keller, and P. Birke, "Comparison of Several Methods for Determining the Internal Resistance of Lithium Ion Cells," Sensors, vol. vol. 10, no. 6, pp. 5604-5625, 2010.

[62] T. B. Reddy., "Linden's Handbook of Batteries. McGraw-Hill Inc., 2011. ix, x, 3, 4, 5, 6, 7, 8, 50."

[63] J. M. Tarascon, and M. Armand., "Issues and challenges facing rechargeable lithium batteries". Nature, 414:359-367, 2001.

[64] G. H. Kim, M. Keyser, and A. A. Pesaran, "Integration Issues of Cells into Battery Packs for Plug-in and Hybrid Electric Vehicles," in EVS-24 International Battery, Hybrid and Fuel Cell Electric Vehicle Symposium, Stavanger, Norway, 2009.

[65] C. Pals and J. Newman, "Thermal Modeling of the Lithium/Polymer Battery I. Discharge Behaviour of a Single Cell, Journal of Electrochemical Society, 1995, Volume 142, pp. 3274-3279."

[66] V. Yufit. B. Wu, M. Marinescu, G. J. Offer, R. F. Martinez-Botas and N. P. Brandon, "Coupled thermal–electrochemical modelling of uneven heat generation in lithium-ion battery packs," Journal of Power Sources, vol. 243, pp. 544-554, 2013.

[67] A. A. Pesaran, "Battery thermal models for hybrid vehicle simulations," Journal of Power Sources, vol. 110, no. 2, pp. 377-382, 2002.

[68] A. Pesaran. G. Kim, and R Spotnitz., "A three-dimensional thermal abuse model for lithium-ion cells". Journal of Power Sources, 170(2):476-489, 2007.

[69] X. Wang, H. Sun, B. Tossan, R. Dixon, "Three-dimentional thermal modeling of a lithium-ion battery pack", Journal of power Sources 206 (2012) A611

[70] K. Yeow, H. Teng, "Reducing temperature gradients in high-power, large-capacity lithium-ion cells through ultra-high thermal conductivity heat spreaders embedded in cooling plates for battery systems with indirect liquid cooling", SAE Technical Paper 2013-01-0234, 2013, doi:10.4271/2013-01-0234.

[71] G. Karimi and A. Dehghan, "Thermal management analysis of a lithium-ion battery pack using flow network approach," International Journal of Mechanical Engineering and Mechatronics, vol. 1, 2012.

[72] C. B. Shin. U.S. Kim, C.S.Kim, "Effect of electrode configuration on the thermal behavior of a lithium-polymer battery, Journal of Power sources 180 (2008)."

[73] G. H. Kim. A. A. Pesaran, K. Smith, S. Santhanagopalan, K. J. Lee "Overview of computer-aided engineering of batteries and introduction to multi-scale, multi-dimensional modeling of Li-ion batteries", DOE Hydrogen program and vehicle technologies program, NREL, 2012.

[74] Y. Ye, N. Cai, J. Lee and X. He, "Electro-thermal modeling and experimental validation for lithium ion battery," Journal of Power Sources, vol. 199, pp. 227-238, 2012.

[75] B. Li. C. Mi, D. Buck and N. Ota, "Advanced Electro-Thermal Modeling of Lithium-Ion Battery System for Hybrid Electric Vehicle Applications," IEEE, 2007.

[76] J. Jing, S. Chen, and K. Yang, "Temperature characterization ananlysis of $LiFePO_4$/C power battery during charging and discharging," Journal of Thermal Analysis and Calorimetry, vol. 99, pp. 515-521, 2010.

[77] V. V. Viswanathan, J. G. Zhang, and R. E. Williford, "Effects of entropy changes in anodes and cathodes on the thermal behavior of lithium ion batteries," Journal of Power Sources, vol. 189, pp. 101-107, 2009.

[78] S. Garimella, T. M. Bandhauer, and T. F. Fuller., "A critical review of thermal issues in lithium-ion batteries". Journal of the Electrochemical Society, 158:R1-R25, 2011.

[79] H. Maleki, J. S. Hong, S. Al Hallaj, L. Redey, and J. R. Selman., "Electrochemical-calorimetric studies of lithium-ion cells". Journal of the Electrochemical Society,145:1489-1591, 1998.

[80] Al Hallaj, and J. R. Selman., "Characterization of commercial li-ion batteries using electrochemical-calorimetric measurements". Journal of Power Sources, 87:186-194, 2000.

[81] J. S. Kim, "Thermal characteristics of $LiMn_20_4$ Spinel",Electrochemical and solid-state letters, vol. 4, no. 9, pp. A141-A144, 2001.

[82] Y. Kobayashi, K. Kumao, T. Takei, K. Iwahori, and I. Uchida., " Pre-cise electrochemical calotimetry of $liCoO_2$/graphite lithium-ion cell". Journal of the Electrochemcial Society, 149(8):A978-A982, 2002.

[83] H. Kameyama, K. Onda, T. Hanamoto, and K. Ito., "Experimental study on the heat generation behavior of small lithium-ion secondary batteries". Journal of the Electrochemical Society, 150, 2003.

[84] H. Y. H. Bang, Y. K. Sun, and J. Prakash., "In situ studies of $li_xMn_2O_4$ and li_xAl_0:17mn1:83o3:97o3:97s0:03 cathode by imc". Journal of The Electrochemical Society,15:A421-A428, 2005.

[85] K. E. Thomas and J. Newman, "Thermal modeling of porous insertion electrodes," Journal of the Electrochemical Society, vol. 150, no. 2, pp. A176-A192, 2003.

[86] X. Guo, Z. Lv, and X P Qiu "New li-ion battery evaluation research based on thermal property and heat generation behavior of battery", Chinese Journal of Chemical Physics, vol. 25, no. 6, pp. 725-732, 2012.

[87] A. P. Matthew A Keyser, and Mark Mihilic, "Thermal characterization of advanced lithium-ion polymer cells", National Renewable Energy Laboratory http://www.nrel.gov/transportation/BTM, Third Advanced Automotive Battery Conference, June 2003.

[88] M. C. Niculuta and C. Veje, "Analysis of the thermal behavior of a $LiFePO_4$", Journal of Physics: Conference Series, vol. 395, 2012.

[89] Y. Chen. A. J. Evans. Journal of Electrochemical Society, 1994, Volume 141, pp 2947-2952.

[90] G. Wierschem, B. McKinney, and E. Nrotek. "Thermal management of lead-acid batteries for electric vehicles," presented at the batteries for electric vehicle- Research Development and Testing Conference, Detroit, MI, February 28, 1993.

[91] W. B. Gu and C. Y. Wang, "Thermal-Electrochemical Modeling of Battery Systems," Journal of The Electrochemical Society, vol. 147, no. 8, pp. 2910-2922, 2000.

[92] A. Vlahinos, S. D. Burch, and A. A. Pesaran, "Thermal performance of EV and HEV battery modules and packs," National Renewable Energy Laboratory, Golden, Colorado, 1997.

[93] R. Xiong, H. He, and J. Fan. "Evaluation of lithium-ion battery equivalent circuit models for state of charge estimation by an experimental epproach," Energies, vol. 4, pp. 582-598, March 2011.

[94] S. Li. Xiaosong Hu, and Huei Peng, "A comparative study of equivalent circuit models for Li-ion batteries," Journal of Power Sources, vol. 198, pp. 359-367, October 2012.

[95] T. Kim and W. Qiao. "A hybrid battery model capable of capturing dynamic circuit characteristics and nonlinear capacity effects," IEEE Transactions on Energy Conversion, vol. 26, no. 4, pp. 1172-1180, December 2011.

[96] M. Ceraolo, T. Huria, J. Gazzarri, and R. Jackey, "High fidelity electrical model with thermal dependence for characterization and simulation of high power lithium battery cells," Electric Vehicle Conference (IEVC), 2012 IEEE International, Greenville, 2012, pp. 1-8.

[97] R. E. Gerver and J. P. Meyers, "Three-dimensional modeling of electrochemical performance and heat generation of lithium-ion batteries in tabbed planar configurations", Journal of the Electrochemical Society, vol. 158, no. 7, pp. A835 - A843, 2011.

[98] Battery University. (February 2011). How to store batteries. Available: http://batteryuniversity.com/learn/article/how_to_store_batteries

[99] R. Spotnitz, "Simulation of capacity fade in lithium-ion batteries," *J. Power Sources,* vol. 113, no. 1, pp. 72-80 2003.

[100] Electropaedia. (retrieved 29 January 2011). Cell Chemistries. Available: http://www.mpoweruk.com/chemistries.htm

[101] Q. Zhang, and R. E. White. "Capacity fade analysis of a lithium ion cell," J. Power Sources, vol. 179, no. 2, pp. 793-798, 2008.

[102] T. Gustafsson, K. Edström, and J.O. Thomas, "The cathode–electrolyte interface in the Li-ion battery," Electrochim. Acta, vol. 50, no. 2-3 pp. 397–403 2004.

[103] M. Dubarry, and B. Y. Liaw, "Identify capacity fading mechanisms in a commercial $LiFePO_4$ cell," J. Power Sources, vol. 194 no.1, pp. 541-549, 2009.

[104] J. Vetter, M.R. Wagner, C. Veit, K.C. Möller, J.O. Besenhard, M. Winter, M. Wohlfahrt-Mehrens, C. Vogler, and A. Hammouche,"Ageing mechanisms in lithium-ion batteries," J.Power Sources, vol. 147, no. 1-2, pp. 269-281, 2005.

[105] "J. Apt, S. B. Peterson, and J. F. Whitacre, "Lithium-ion battery cell degradation resulting from realistic vehicle and vehicle-to-grid utilization," J. Power Sources, vol. 195, no. 8, pp. 2385-2392, 2010.

[106] C. Rosenkranz. "Plug In Hybrid Batteries," Pres EVS20, p. 14, November 2003.

[107] Electropaedia. (retrieved 2 February 2011). Lithium Battery Failures. Available: http://www.mpoweruk.com/lithium_failures.htm

[108] J. H. Feikert, T.D. Tran, and R.W. Pekala, "Rate effect on lithium-ion graphite electrode performance," J. Appl. Electrochem, vol. 26, no. 11, pp. 1161-1167, 1996.

[109] J. Liu, K. Anime, and I. Belharouak, "High-temperature storage and cycling of $CLiFePO_4$/ graphite Li-ion cells," Electrochem. Com, vol. 7, no. 7, pp. 669-673, 2005.

[110] M. Broussely. "Aging mechanisms and calendar-life predictions in lithium-ion batteries," Adv. in Li-ion batteries, pp. 293-432, 2002.

[111] G. Abbas, Nazri, and Pistoia. Lithium Batteries, Science and Technology : Kluwer Academic Publishers, 2004.

[112] M. Doyle, R. E. White, and P. Arora. "Capacity fade mechanisms and side reactions in Lithium-Ion batteries," J. Electrochem. Soc, vol. 145, no. 10, pp. 3647-3666, 1998.

[113] H. Maleki, and J. N. Howard. "Effects of overdischarge on performance and thermal stability of a Li-ion cell," J. Power Sources vol. 160, no. 2, pp. 1395-1402, 2006.

[114] M. Nagata, C. Kishiyama, J. Dodd, P. Lam, and H. Tsukamoto. "Improvement of deep discharge capability for Lithium-ion batteries," Proc. Electrochem. Soc, vol. 28, pp. 252-259, 2004.

[115] M. B. Stevens. "Hybrid fuel cell vehicle powertrain development considering power source degradation," PhD, University of Waterloo, 2008.

[116] F. Incropera and Dewitt , et al., Fundamentals of Mass and Heat Transfer. Chicago, 2007.

[117] O.FLIR,"Available:http://www.flirthermography.com/media/S60_datasheet.pdf. [Accessed 12 2011].

[118] E. Samadani. S. Panchal, M. Mastali, R. Fraser, "Battery Life Cycle Management for Plug-in hybrid electric vehicle (PHEVs) and electric vehicles (EVs)", A Report on Transport Canada_March 2013

[119] M. Giannikouris, "Battery lifecycle management for PHEVs:Transport Canada Final Report", 2010,

[120] "Energy Content of Fuels-Power Tables".Accessed date : April 2011. http://www.phy.syr.edu/courses/modules/ENERGY/ENERGY_POLICY/tables.html.

[121] R. J. Moffat, "Uncertainty analysis," Electronics Cooling, 5 1999.

[122] "Keithley, Model 2700 Multimeter/Switch System User's Manual," November 2002. [Online]. Available: http://www.ee.bgu.ac.il/~acl/Equip/2700_900_01fnl.pdf. [Accessed 10 October 2013].

Appendix A:

LabView Screenshot

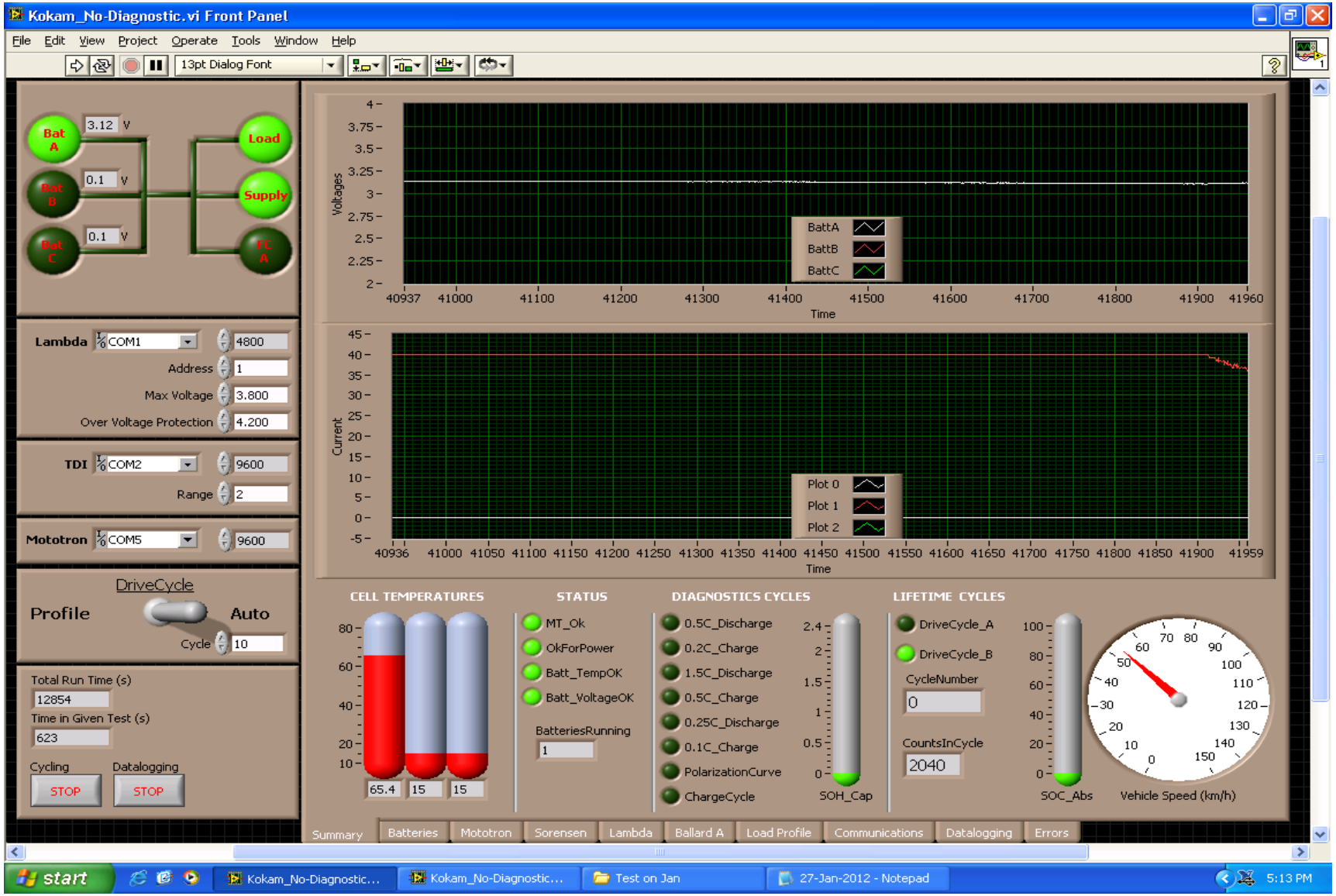

Figure A1: Screenshot of LabView program in control of hybrid test bench

Appendix B:

Part-I Results

Figure B1: Total heat generation rate at 1C, 2C, 3C, 4C & 5, 15, 25, 35 ºC bath temperatures

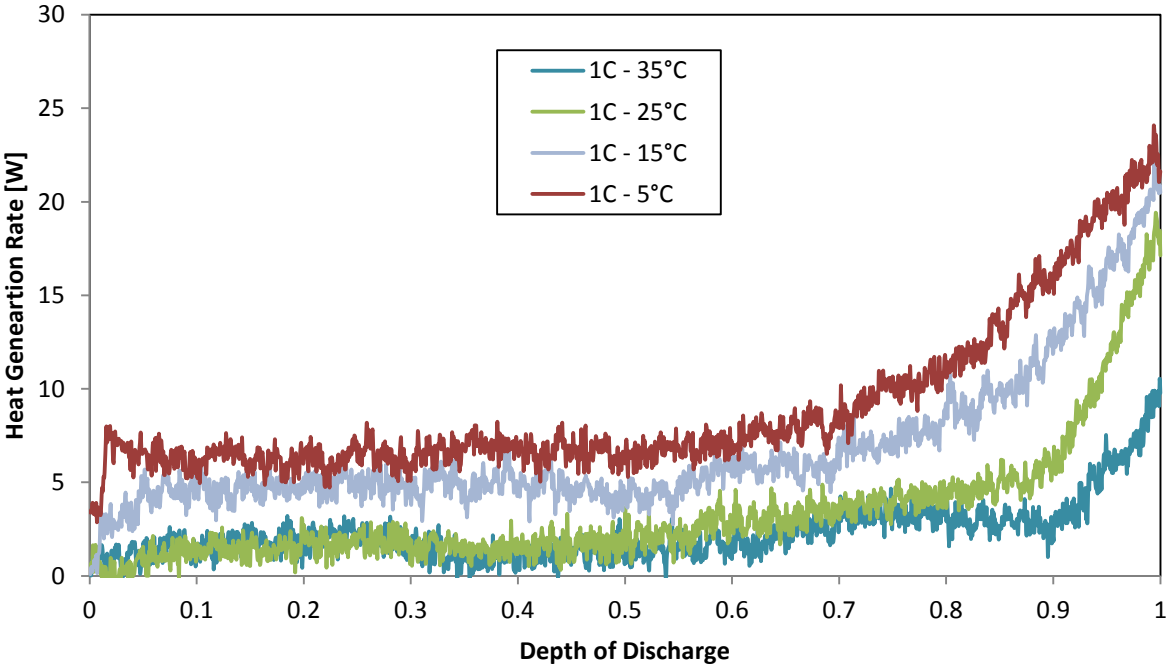

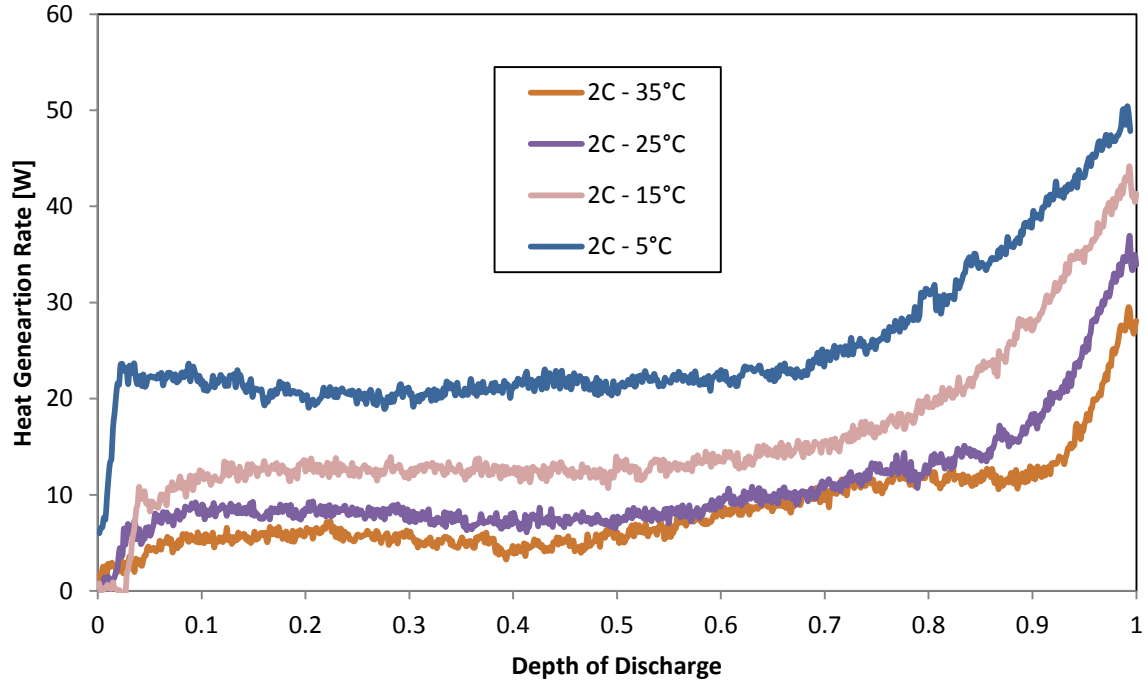

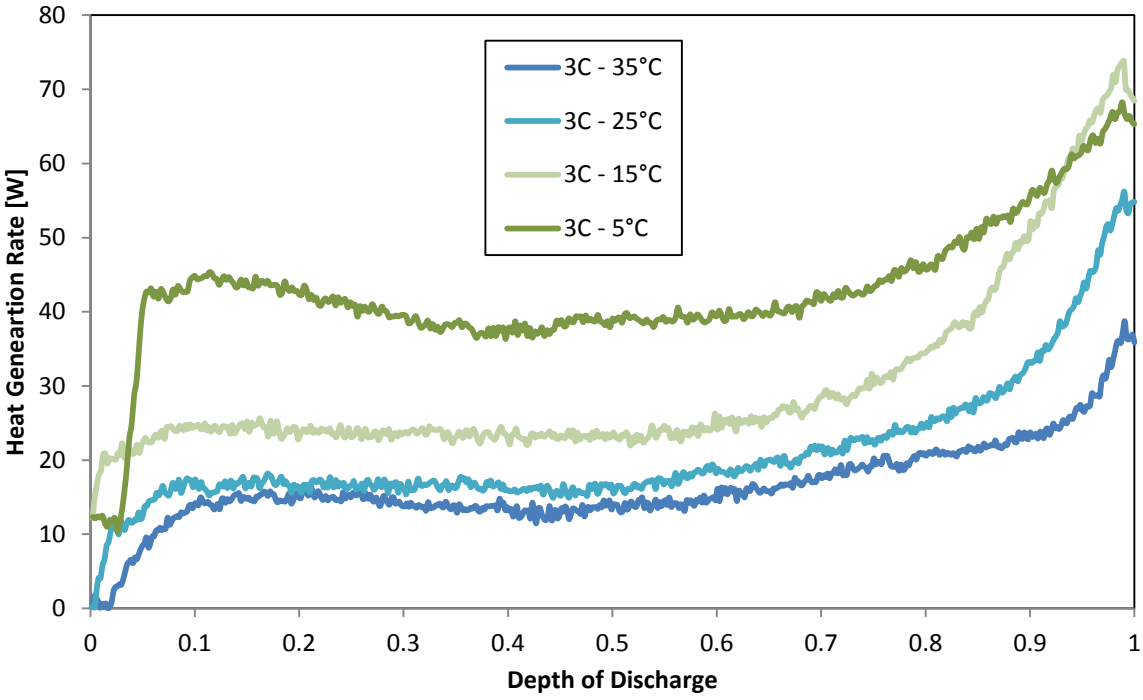
Heat Geneartion Rate [W]
Depth of Discharge
3C - 35°C
3C - 25°C
3C - 15°C
3C - 5°C
0
10
20
30
40
50
60
70
80
0
0.1
0.2
0.3
0.4
0.5
0.6
0.7
0.8
0.9
1

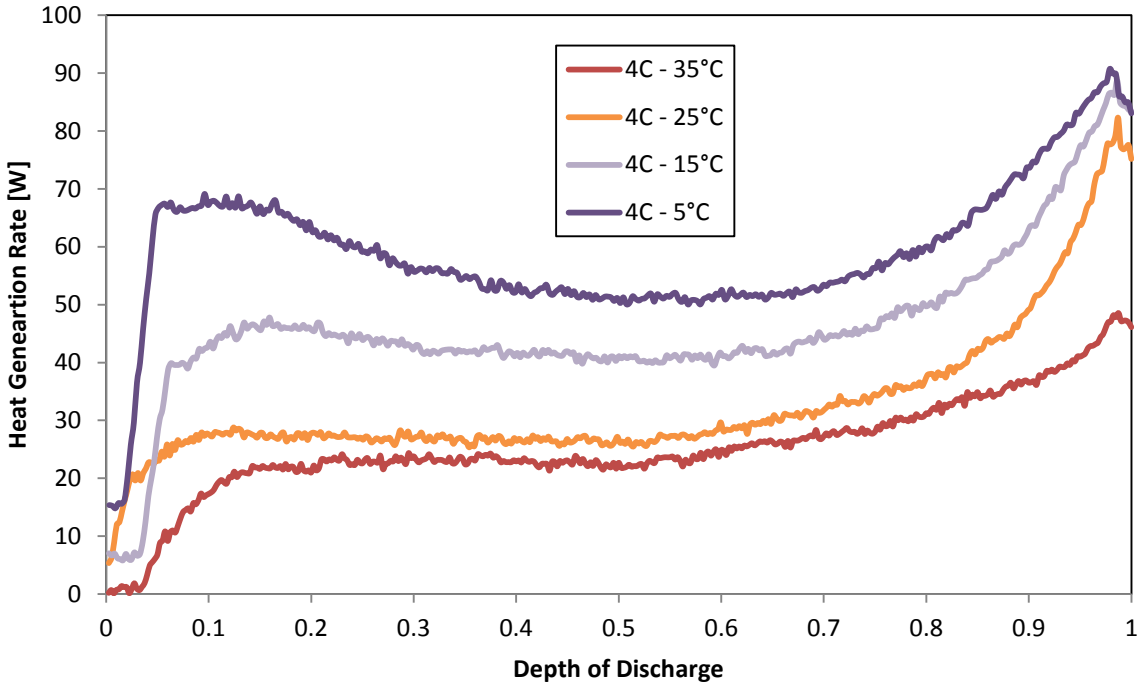
Heat Geneartion Rate [W]
Depth of Discharge
4C - 35°C
4C - 25°C
4C - 15°C
4C - 5°C
0
10
20
30
40
50
60
70
80
90
100
0
0.1
0.2
0.3
0.4
0.5
0.6
0.7
0.8
0.9
1

Figure B2: Battery voltage versus DOD at 1C, 2C, 3C, 4C & 5, 15, 25, 35 ° C bath temperatures

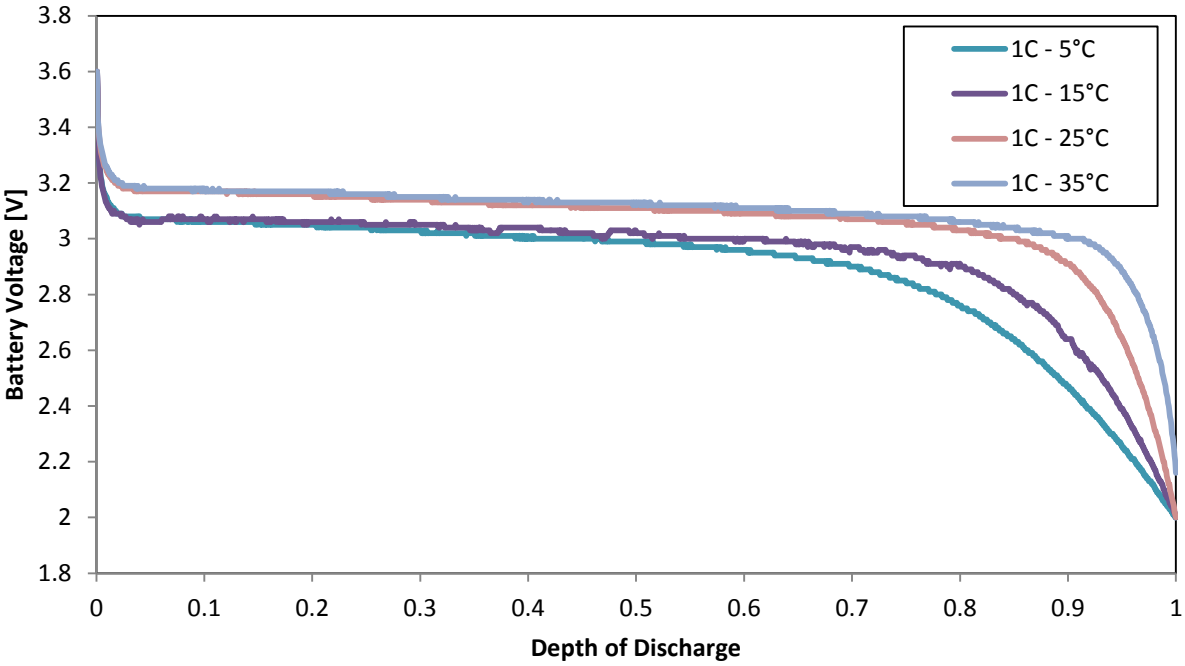

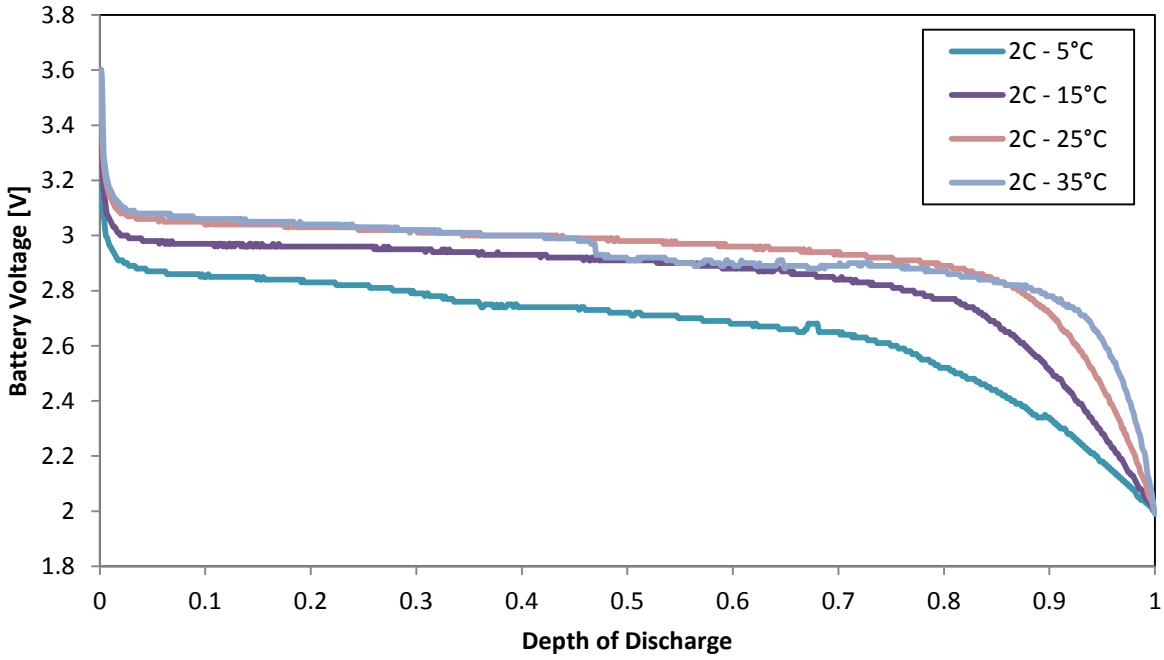

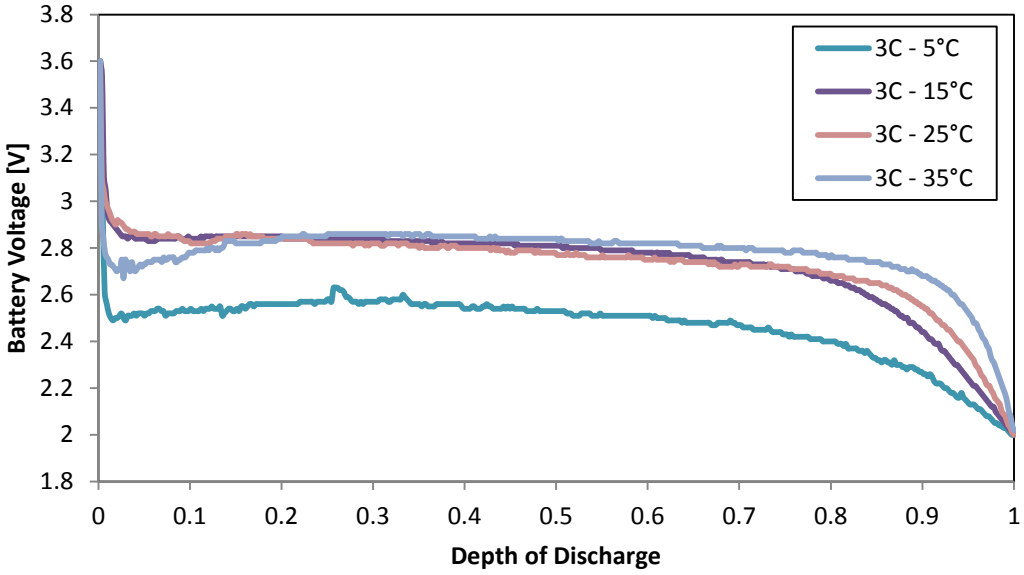
3C - 5°C
3C - 15°C
3C - 25°C
3C - 35°C
Battery Voltage [V]
Depth of Discharge
3.8
3.6
3.4
3.2
3
2.8
2.6
2.4
2.2
2
1.8
0
0.1
0.2
0.3
0.4
0.5
0.6
0.7
0.8
0.9
1

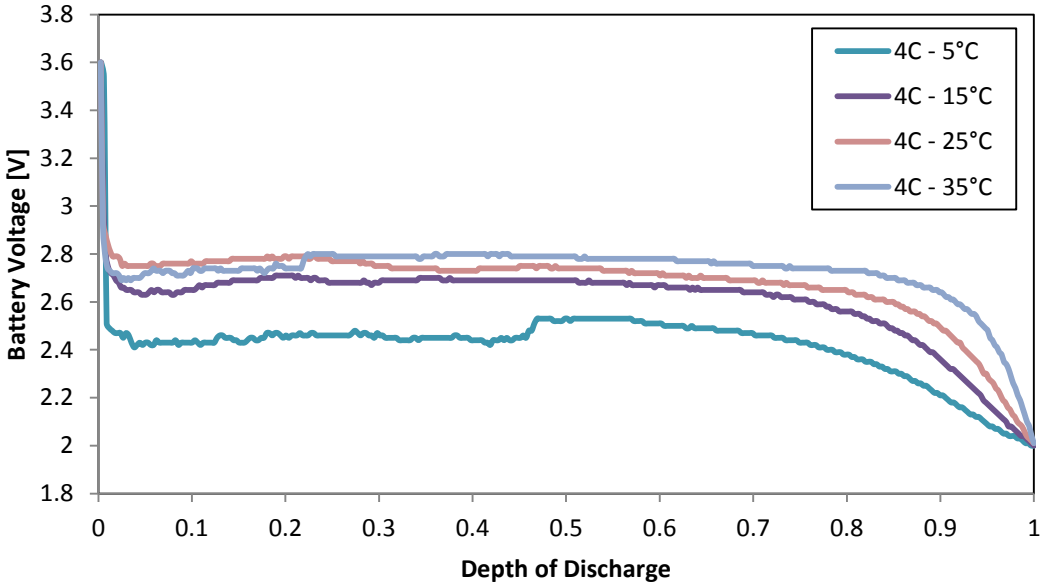
4C - 5°C
4C - 15°C
4C - 25°C
4C - 35°C
Battery Voltage [V]
Depth of Discharge
3.8
3.6
3.4
3.2
3
2.8
2.6
2.4
2.2
2
1.8
0
0.1
0.2
0.3
0.4
0.5
0.6
0.7
0.8
0.9
1

Figure B3: Cell surface temperature profile at 1C & 5, 15, 25, 35 ºC bath temperatures

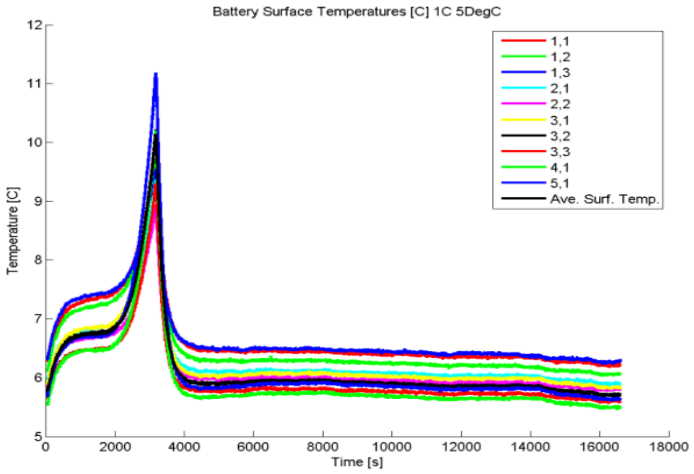

5 ºC

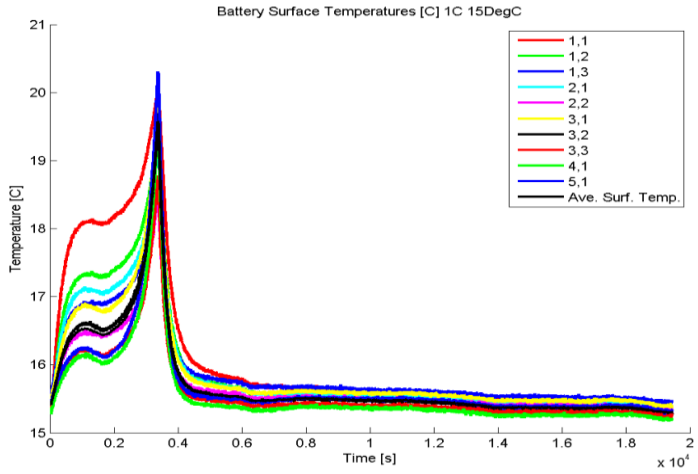

15 ºC

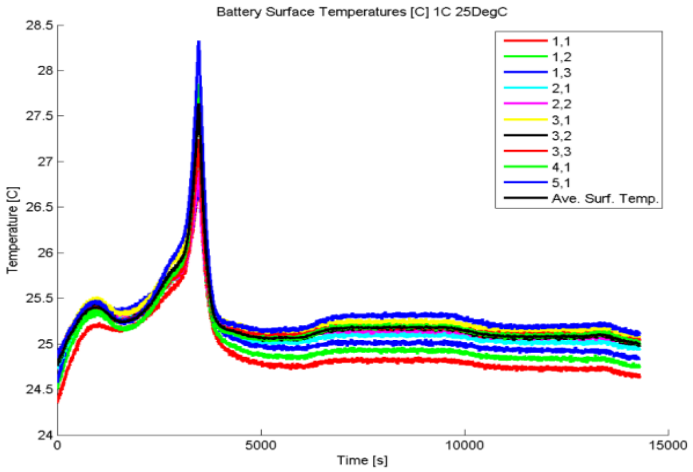

25 ºC

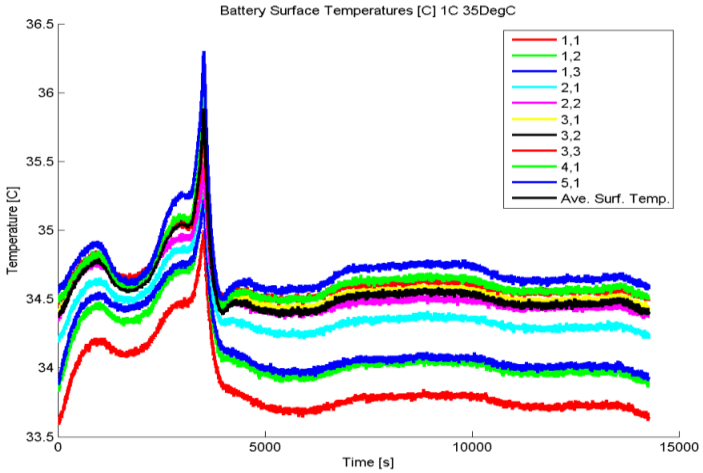

35 ºC

Figure B4: Cell surface temperature profile at 2C & 5, 15, 25, 35 ºC bath temperatures

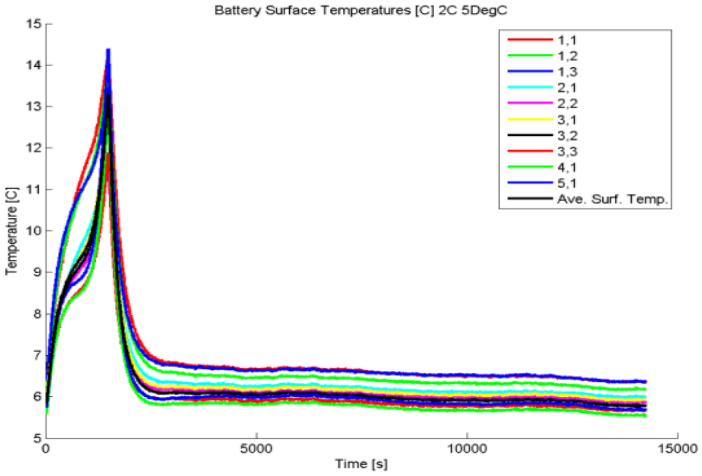

5 ºC

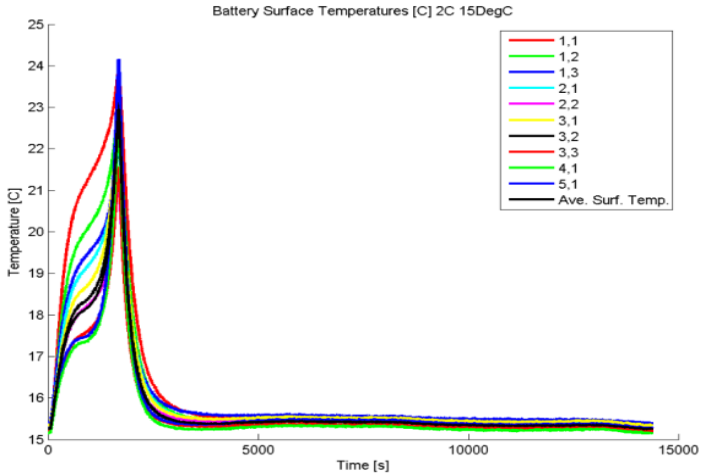

15 ºC

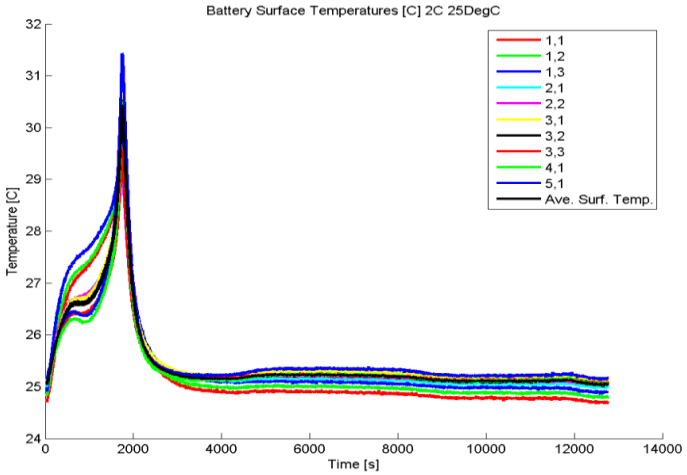

25 ºC

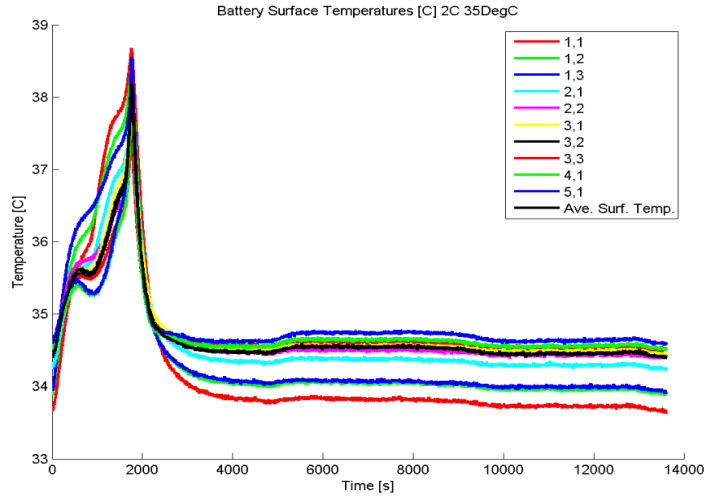

35 ºC

Figure B5: Cell surface temperature profile at 3C & 5, 15, 25, 35 ºC bath temperatures

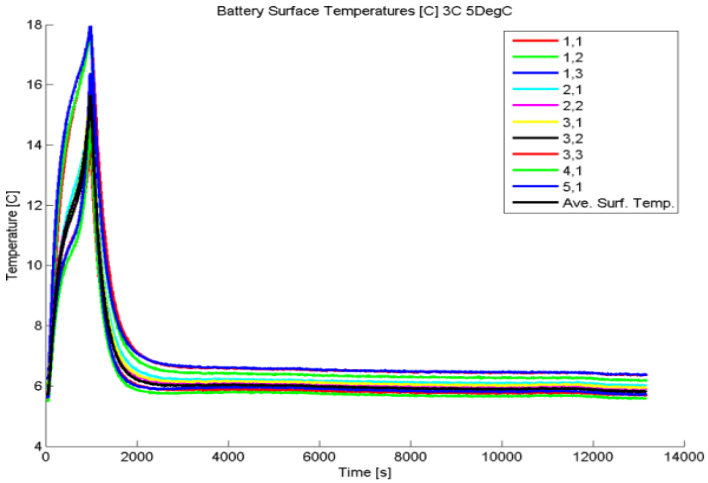

5 ºC

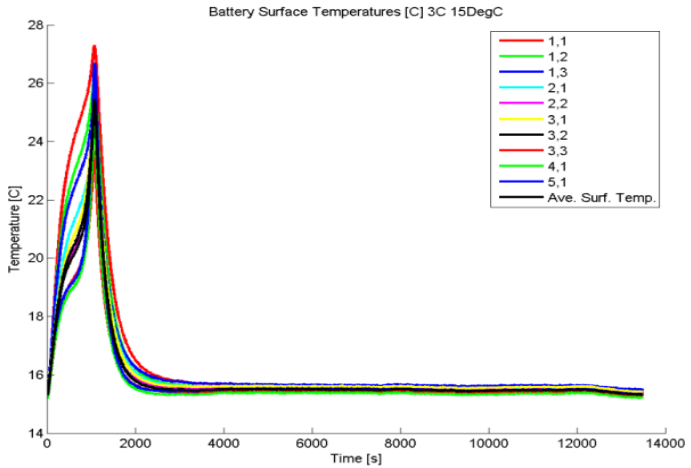

15 ºC

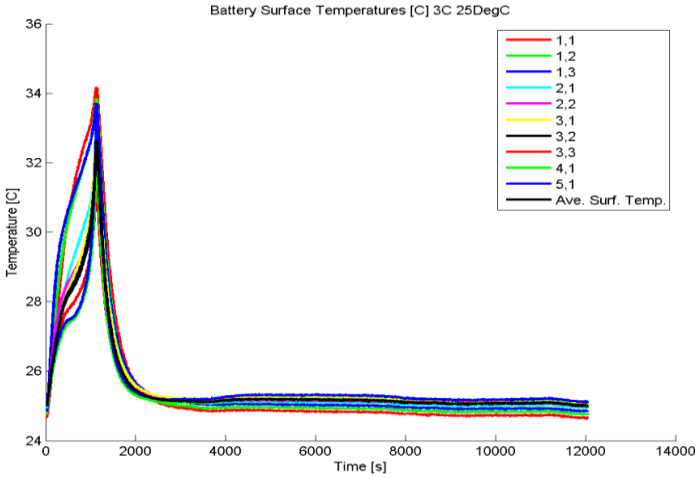

25 ºC

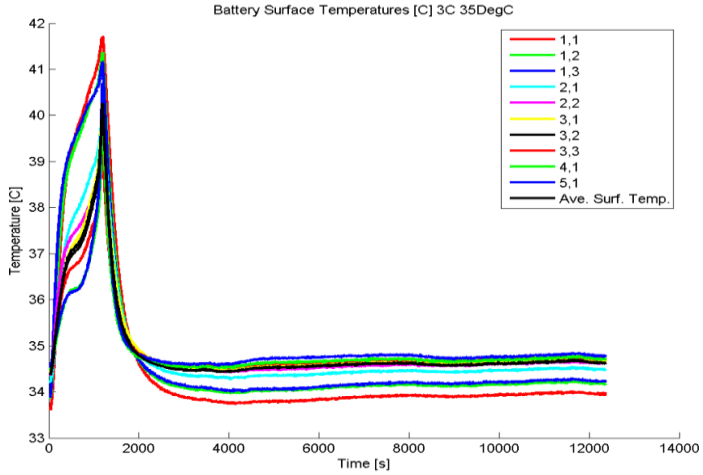

35 ºC

Figure B6: Cell surface temp profile at 4C & 5, 15, 25, 35 ºC bath temperatures

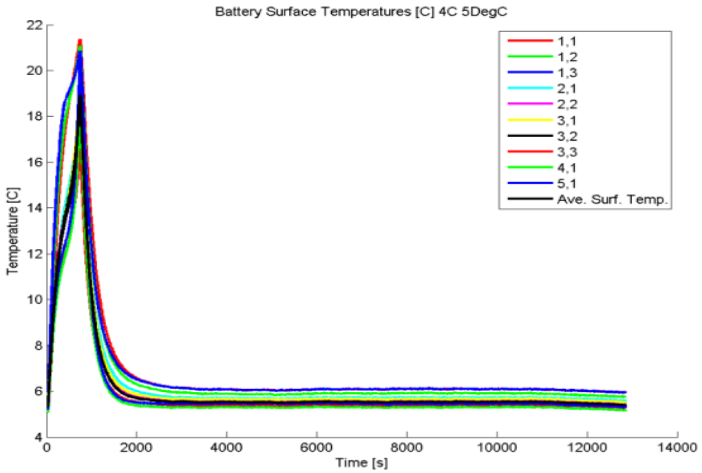

5 ºC

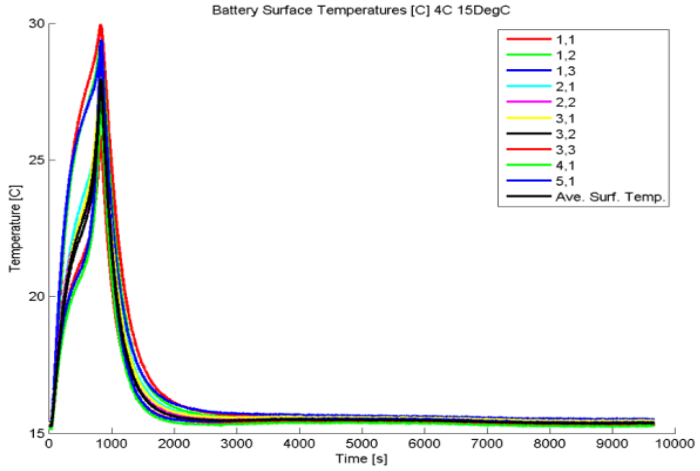

15 ºC

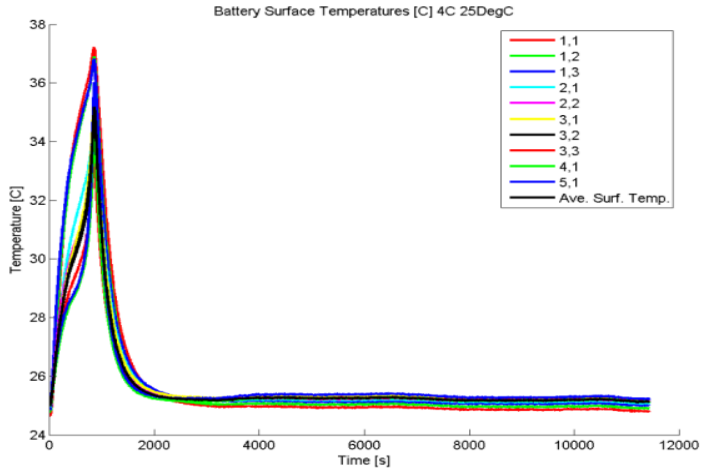

25 ºC

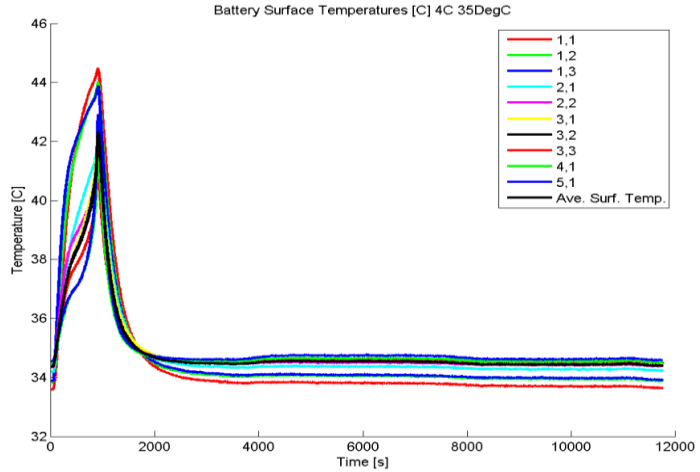

35 ºC

Appendix C:

Part-II Results

Figure C1: EV-ACX2.5 October report

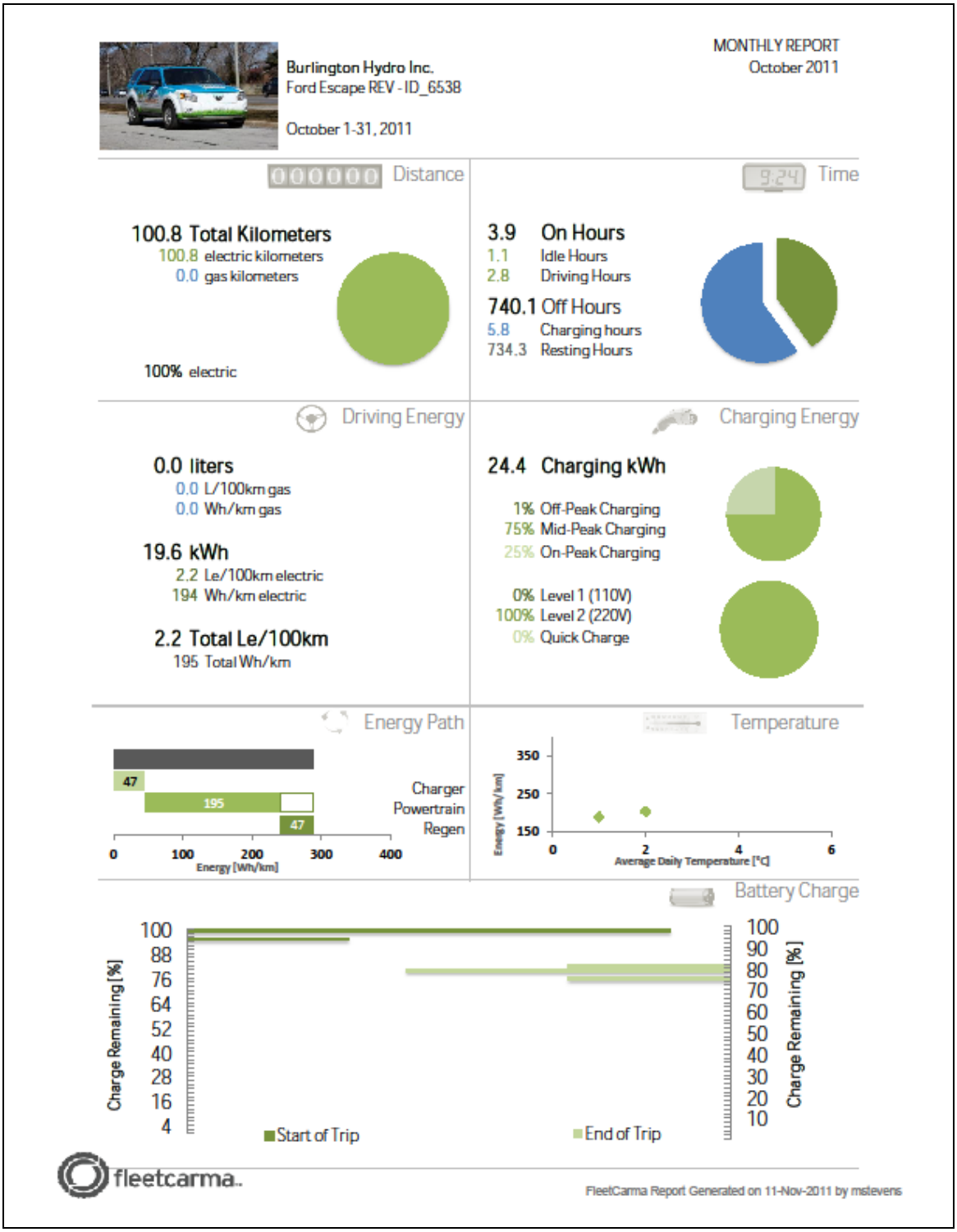

Figure C2: EV-ACX 2.5 November report

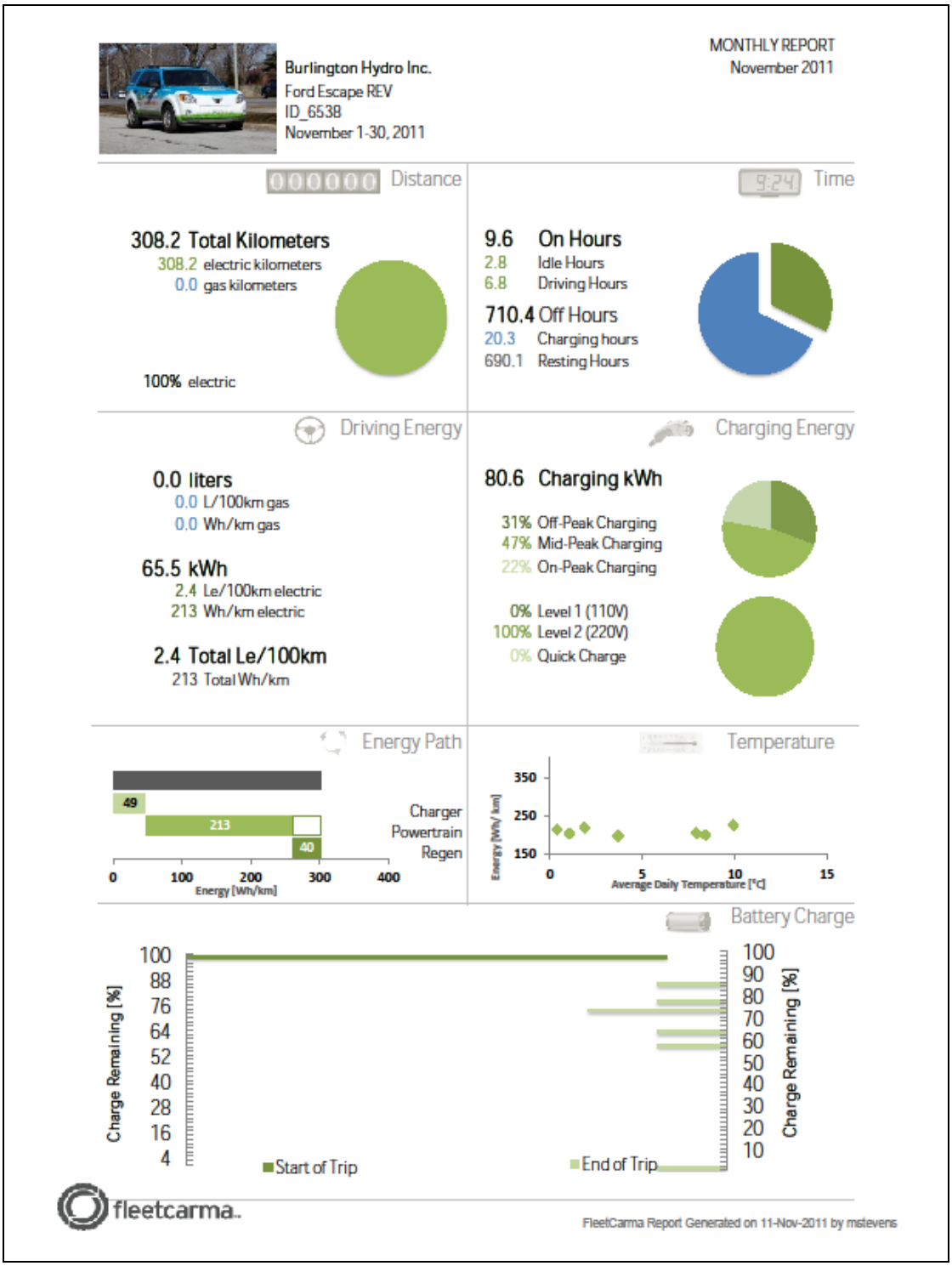

Figure C3: EV-ACX2.5 December report

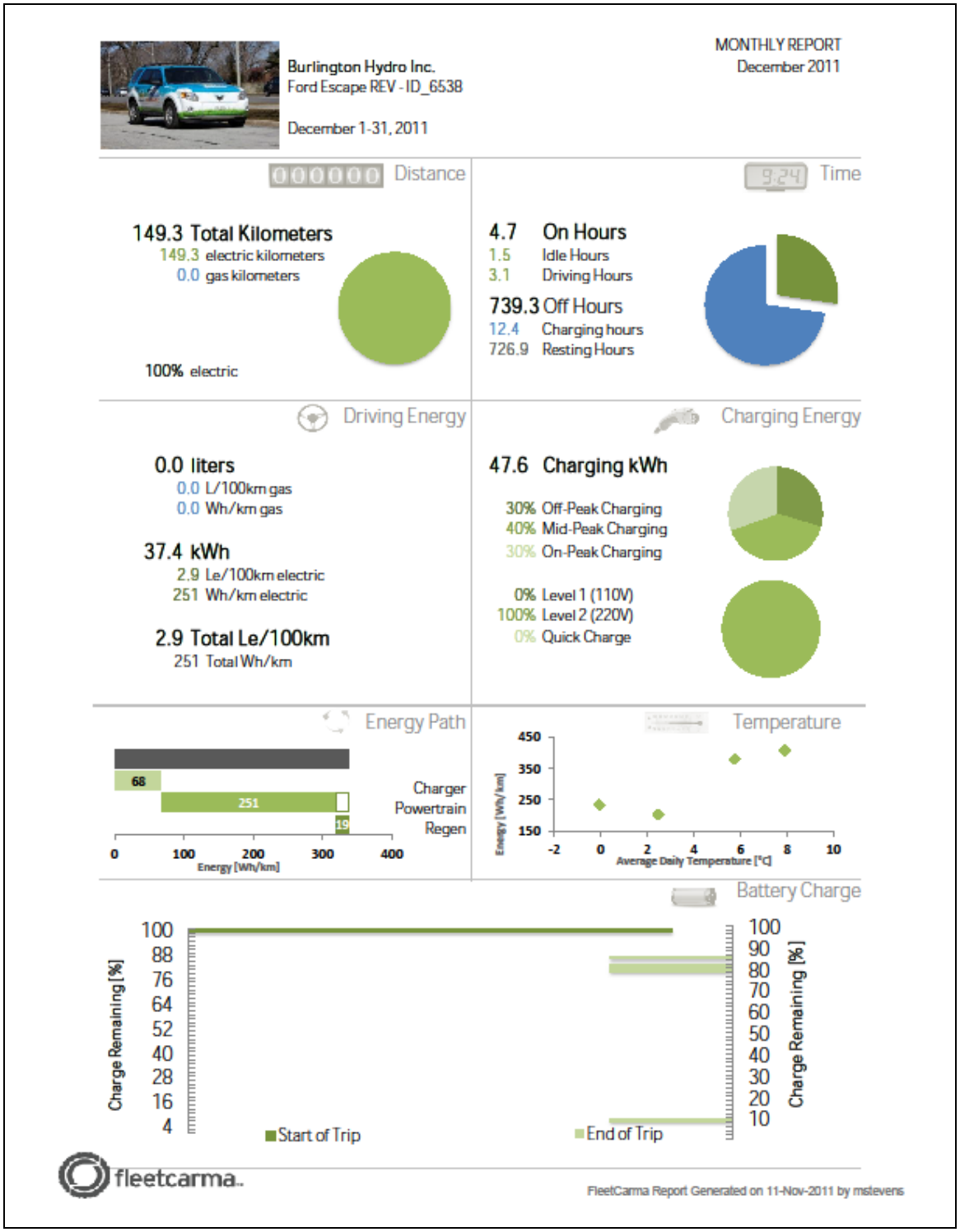

Figure C4: EV-ACX2.5 January report

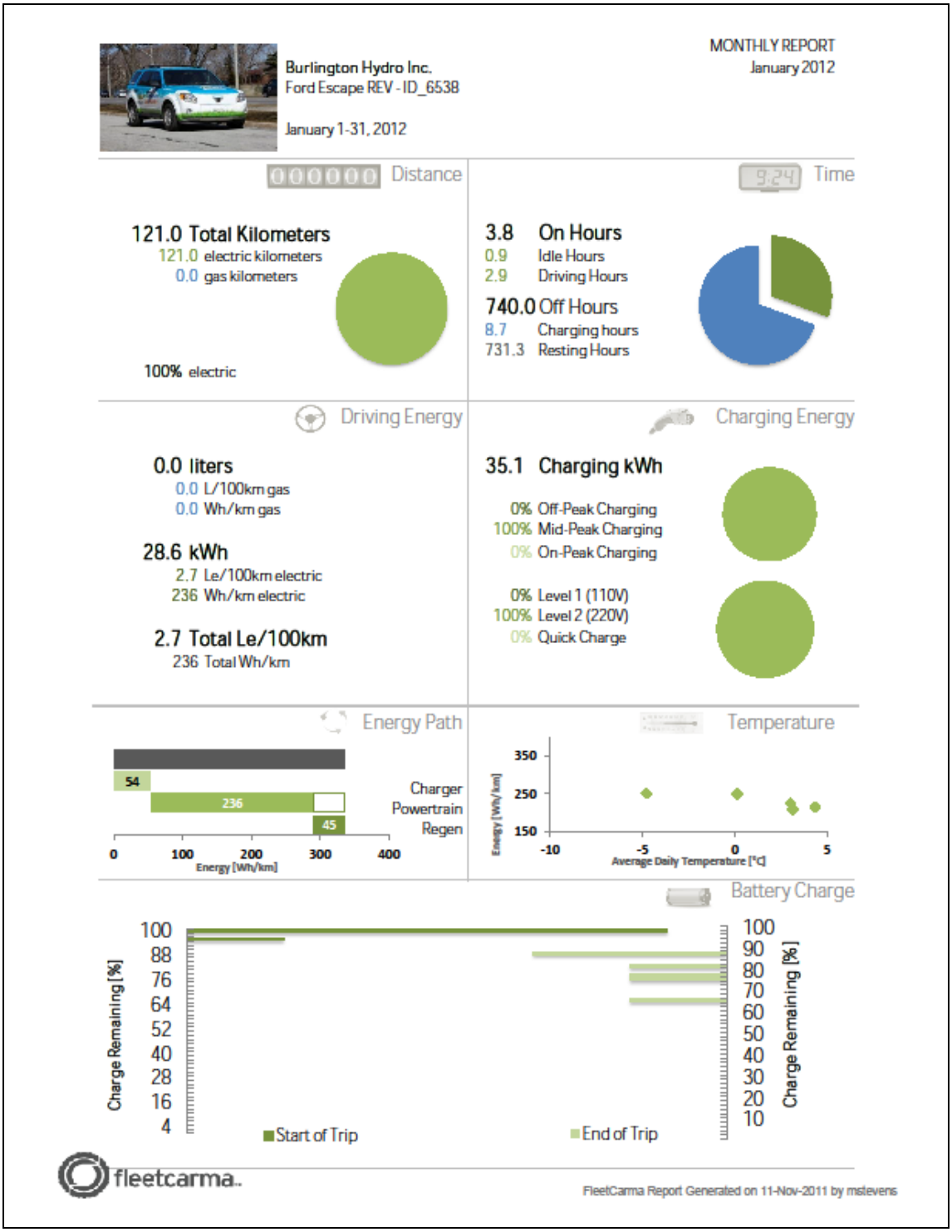

Figure C5: EV-ACX2.5 February report